University of California

Los Angeles

Composition of the Highest Energy Cosmic Rays

A dissertation submitted in partial satisfaction

of the requirements for the degree

Doctor of Philosophy in Physics

by

Matthew David Healy

2007

The dissertation of `Matthew David Healy` is approved.

Graciela Gelmini

Rainer Wallny

Yingnian Wu

Katsushi Arisaka, Committee Chair

University of California, Los Angeles

2007

I dedicate this work to my grandfather David Dieterle, a North Dakota wheat farmer and a man of limited education but an unlimited fascination for the marvels and mysteries of the heavens.

I dedicate this work to my father Richard Healy, a most practical electrical engineer whose great passion has always been the least practical of all the many branches of physics and cosmology.

I dedicate this work to my mother Gloria Dieterle Healy, whose energy level exceeds that of all cosmic rays ever detected. I resolve that one day I will understand where she gets it from.

I dedicate this work to my loving wife Qian Lu, a brilliant psychologist who has partially succeeded in teaching me the unthinkable and the unfathomable, namely that there is more to life than physics.

Most of all, I dedicate this work to the wonderful, simple people of Malargüe, Argentina. To the man, who with no prior notice on a Sunday drove the 280 miles, at breakneck speed over a dusty, rutted, gravel road, to help me catch an airplane flight home. To the restaurantiers, hotel operators, and technicians of Malargüe who have benefited me and my colleagues at the Pierre Auger Observatory. I suspect the people of Malargüe have only limited interest in ultra-high energy cosmic rays, but the help they have given the entire experiment and myself in particular has been totally without limits.

Table of Contents

List of Figures

List of Tables

Acknowledgments

This work has been made possible with the financial support of the United States Department of Energy, Task F grant to K. Arisaka, University of California, Los Angeles. The author acknowledges the work of T. Ohnuki, whose work in building a distributed computing cluster using home PCs as nodes, was instrumental for all phases of the analysis. D. Barnhill also provided invaluable advice and initial direction. The author acknowledges many useful discussions with J. Lee, and to a greater extent the guidance and tremendous insight of the thesis chair, K. Arisaka. The author would also like to acknowledge the commitment of the following funding agencies to the building and support of the Pierre Auger Observatory. Gobierno de Mendoza, Comisión Nacional de Energia Atómica y Municipalidad de Malargüe, Argentina; the Australian Research Council; Fundação de Amparo à Pesquisa do Estado de São Paulo, Conselho Nacional de Desenvolvimento Científico e Tecnológico and Fundação de Amparo à Pesquisa do Estado de Rio de Janeiro, Brasil; National Science Foundation of China; Ministry of Education of the Czech Republic (projects LA134 and LN00A006); Centre National de la Recherche Scientifique, Institut National de Physique Nucléaire et Physique des Particules (IN2P3/CNRS), Institut National des Sciences de l'Univers (INSU/CNRS) et Conseil Régional Ile de France, France; German Ministry for Education and Research and Forschungszentrum Karlsruhe, Germany; Istituto Nazionale di Fisica Nucleare, Italy; Consejo Nacional de Ciencia y Tecnologia, Mexico; the Polish State Committee for Scientific Research (grant numbers 1P03D 01430, 2P03B 11024 and 2PO3D 01124), Poland; Slovenian Research Agency; Ministerio de Educación y Ciencia (FPA2003-08733-C02, 2004-01198), Xunta de Galicia (2003 PXIC20612PN, 2005 PXIC20604PN) and Feder Funds, Spain; Particle Physics and Astronomy Research Council, UK; the

US Department of Energy, the US National Science Foundation, USA, and UNESCO. Partial support of ALFA-EC funds, in the framework of the HELEN Project, is gratefully acknowledged.

Vita

1979	Born, Waltham, Massachusettes USA
1998	Graduated Nashoba Regional High School, Bolton Massachusettes
2002	Graduated with honors Clarkson University, Potsdam New York
2002	Moved to Los Angeles, California to begin graduate work at the University of California, Los Angeles
2003	Masters Degree in Physics from the University of California, Los Angeles
2004	Joined the Pierre Auger Collaboration to begin original research
2005	Advanced to Candidacy for the degree of Doctor of Philosophy in Physics
2005	Presented original research at the 29^{th} ICRC (Pune)
2005	Married the woman of my dreams, Qian Lu
2007	Chosen by the Pierre Auger Collaboration to speak about composition studies with the surface detector at the 30^{th} ICRC (Mérida)
2007	Completed the requirements for the degree of Doctor of Philosophy in Physics at the University of California, Los Angeles

Publications and Presentations

M. D. Healy *et al.* [Pierre Auger Collaboration], Long Term Stability of Water Stations in the Pierre Auger Surface Detecrtor, Proc. 29^{th} Intern. Cosmic Ray Conf., Pune (2005)

M. D. Healy *et al.* [Pierre Auger Collaboration], Composition-sensitive parameters measured with the surface detector of the Pierre Auger Observatory, Proc. 30^{th} Intern. Cosmic Ray Conf., Mérida (2007)

M. D. Healy *et al.* [Pierre Auger Collaboration], Search for Ultra-High Energy Photons with the Pierre Auger Observatory, Proc. 30^{th} Intern. Cosmic Ray Conf., Mérida (2007)

M. D. Healy *et al.*, Observation of the Long Term Stability of Water Stations in the Pierre Auger Surface Detector, In preparation

D. Barnhill *et al.* [Pierre Auger Collaboration], Upper Limit on the Cosmic Ray Photon Flux Above 10^{19} eV Using the Surface Detector of the Pierre Auger Observatory, In preparation

K. Arisaka *et al.*, Composition of UHECR and the Pierre Auger Observatory Spectrum, Journal of Cosmology and Astroparticle Physics, In preparation

I. Allekotte *et al.*, The Surface Detector System of the Pierre Auger Observatory, Nucl. Instrum. Meth., In preparation

A. Tripathi *et al*, A Systematic Calibration of Surface Detectors using Muon Data from the Engineering Array, Internal Gap Note 2002-046

A. Tripathi *et al*, The Offline SD Calibration and Monitoring Database in the DPA Framework, Internal Gap Note 2004-039

J. Lee *et al*, Long Term Performance and Stability of the Surface Detector from September 2003 through June 2004, Internal Gap Note 2004-044

D. Barnhill *et al*, A Preliminary Upper Limit on the Photon Fraction Using Rise Time Information, Internal Gap Note 2005-024

T. Ohnuki *et al*, Search for Small Scale Angular Clustering of Cosmic Rays Above 10 EeV in the Auger Surface Detector Data, Internal Gap Note 2005-026

M. D. Healy *et al*, Observation of the Long Term Stability of Water Tanks in the Pierre Auger Surface Detector, Internal Gap Note 2005-028

A. Calvez *et al*, Preliminary BL Lacertae Correlation Studies with the Auger Data, Internal Gap Note 2005-057

A. Tripathi *et al*, A Preliminary Estimate of The Cosmic Ray Energy Spectrum from Pierre Auger Observatory Data, Internal Gap Note 2005-061

J. Lee *et al*, An Analysis of the Angular Resolution of the Surface Detector, Internal Gap Note 2005-079

M. D. Healy *et al*, Long Term Performance and Stability of the Surface Detector over Two Years of Data Taking, Internal Gap Note 2005-090

D. Barnhill *et al*, A Study of Composition Trends Using Rise Time Data, Internal Gap Note 2006-017

M. D. Healy *et al*, Applying the Constant Intensity Cut to Determine Composition, Energy, and Muon Richness, Internal Gap Note 2006-020

J. Lee *et al*, The Cosmic Ray Spectrum with 2 Years of Data, Internal Gap Note 2006-039

M. D. Healy *et al*, A Study of Composition Trends Using Rise Time and Curvature Data, Internal Gap Note 2006-092

J. Lee *et al*, The Latest Auger Spectrum and Theoretical Implications, Internal Gap Note 2007-012

Abstract of the Dissertation

Composition of the Highest Energy Cosmic Rays

by

Matthew David Healy

Doctor of Philosophy in Physics

University of California, Los Angeles, 2007

Professor Katsushi Arisaka, Chair

I present a detailed investigation of the composition of comsic rays with energies greater than 1×10^{19} eV with the Pierre Auger Observatory. Initial studies were found to indicate that a model of pure proton primaries was inconsistant with the data collected. A detailed method is developed to use observables from the surface detector as proxies for the depth of shower maximum - the depth in g cm^{-2} where the number of electrons and positrons is greatest. The depth of shower maximum (known as X_{max}) is closely associated with the mass of the primary cosmic ray. The estimates from the surface detector are compared, using the hybrid technique, to the subset of showers containing direct measurements of X_{max} by the fluorescence detector. Extending the surface detector measurements to the highest energies shows that primary cosmic rays are trending away from the expectation for a pure proton stream toward an increasingly heavy mixture of elements.

CHAPTER 1

Introduction

1.1 Cosmic Rays in Our Midst

The study of cosmic rays is at the intersection point for many of today's leading topics in physics. Their study combines aspects of cosmology, astronomy, astrophysics, and particle physics to form an unique confluence between the world of the small and the world of the large. Delivered to us for free every second of every day, we only need to know how to look for them...

> In 1992 the fastest object known to mankind hit the Earth's atmosphere 25 kilometers above Utah. When it struck, it was moving at 99.999 999 999 999 999 999 999 percent of the speed of light, which is the maximum possible speed for ordinary matter. The object concerned was a cosmic ray, or, more accurately, a cosmic particle [2].

1.1.1 What are cosmic rays?

Cosmic *rays* is a historical misnomer. The word originates from the discovery of energetic particles emitted, in the earliest cases, by radioactive matter. These were the alpha, beta, and gamma rays which were later identified to actually be a helium nucleus, a positron, and a photon respectively. Before these identifications were made however other sources of radiation were found. These were the x-

rays identified by William Roentgen [3] and the most bizarre of all, the cosmic rays, so named because they seemed to be coming from the cosmos itself. With the identification of the particles involved, the alpha and beta were renamed as particles while the photons (gamma rays and x-rays) maintained their names. It took significantly longer to identify cosmic rays and by the time it was confirmed they were not photons the name was firmly in place[1]. As it turns out, cosmic rays are primarily atomic nuclei with various masses, the distribution of which varies with energy. In this way they are most similar to alpha particles, and perhaps should be called cosmic particles. However besides the source, radioactive matter versus the depths of space, there is another glaring difference between alpha particles and cosmic rays. Alpha particles typically carry a few tens-of-thousands of electron-volts[2] in kinetic energy, cosmic ray kinetic energies range from a few mega up to a few zeta electron-volts[3]. The answer to the question, "What are cosmic rays?"; Cosmic rays are atomic nuclei of various elements that arrive at the Earth from outer space with potentially enormous energies (see fig. 1.2).

1.1.2 Historical developments

Cosmic rays have been a topic of study in physics for almost 100 years now. They were first discovered in 1911 by an Austrian physicist named Viktor Hess. He carried an ionization chamber[4] with him on several balloon flights of varying altitude. His results showed ambient radiation increased with altitude as in fig. 1.1.

[1] Actually the search for cosmic ray photons is an active area of research at higher energies because of the implications they would have for particle physics and cosmology [4]

[2] An electron-volt (or eV) is equal to 1.602×10^{-19} joules of energy, or if you like the highest energy cosmic rays contain about the same energy as half a kitchen match [5]

[3] zeta = 10^{21}

[4] an ionization chamber is similar in function to a gieger counter

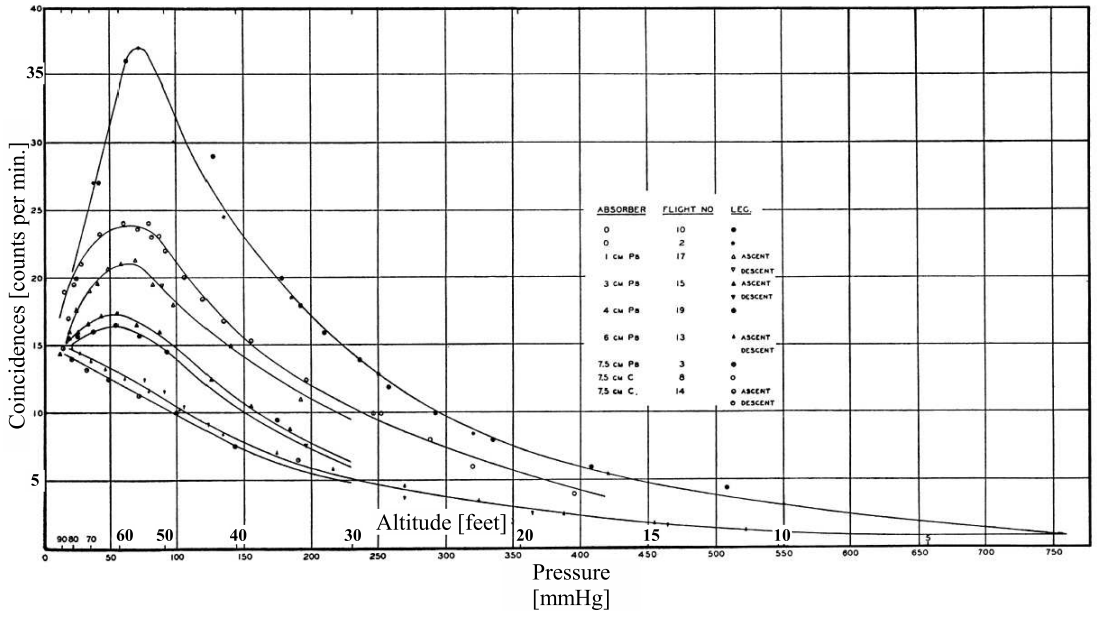

Figure 1.1: A more modern version of Hess' original experiment taken from [6]. The radiation, shown on the y-axis as the number of counts recorded in an absorber, reaches a maximum above 50,000 feet. The various curves represent the multiple absorbers used in either an ascent or decent path of the balloon. The thicker absorbers record a smaller number of counts suggesting that radiation of greater penetrating power (i.e. particles with a larger energy) have a lower flux.

Thus he was the first to confirm a source of radiation from above, and later that the flux was variable [7]. This discovery was actually the answer to a much older puzzle from the late 1700s when Coulomb (the man who discovered static change) demonstrated that a statically charged object will discharge over time. The only way that could happen was if the air was somehow conducting the change away because it contained charge carriers that were free to move. At the time Coulomb knew of no way to produce ions outside the lab and thus it was an open question. Progress was made in 1901 when Wilson showed that no matter how pure the

air was he could not stop a charged object from spontaneously discharging. To show this he took clean air, dirty air, moist air, dry air, etc. but was unable to eliminate the discharge effect and because the static charge dissipated regardless of the polarity of the original charge the air had to be filled with ions of both charges. Furthermore, since ions of opposite charges will recombine to form neutral particles, there had to be a source of new ions otherwise the air would quickly become inert. With this in mind Wilson concluded there had to be a source of new ions and the list of possibilities was short: there were X-rays, cathode rays, and radioactive elements. As far as Wilson knew, X-rays and cathode rays could only be produced in the lab and radioactive elements were rare, so the search was on to find a source of ions common enough to be in operation everywhere on Earth. He conjectured that space might have something to do with it and to test that idea he tried his experiment underground because the addition of rock above his head would provide shielding. Unfortunately with the instruments he had at the time the train tunnel he used was not deep enough to demonstrate the effect so he dropped the idea. That was where Hess came in, with an improved tool (the ionization chamber) and a hot air balloon which could take him to great heights, thus reducing the shielding (in this case the air itself), he observed the predicted increase in radiation. Finally a source of ions had been found that would operate no matter where on Earth an observer was.

Although this succeeded in verifying the source of radiation, the type was still in question. Experiments into this area revealed that not only was the type unknown, it was unlike anything previously observed. Cosmic rays, as they had come to be known, could be observed underwater and even in deep mines. Gamma rays, the more energetic cousins of X-rays, were the only things that came close to that kind of penetrating power but even they fell short. Furthermore, with the invention of the gieger counter it was shown that cosmic rays occasionally arrived

in groups triggering multiple gieger counters at the same time even though they had been separated. Setting the counters up so the largest detecting area was in a particular direction showed cosmic rays had a preference for the east-west direction rather then north-south. There was only one explanation, cosmic rays were charged particles and therefore bent to a preferred direction because of the Earth's magnetic field. This discovery finally eliminated any talk of gamma rays because they are photons and therefore uncharged. Another instrumentation breakthrough in the early 1920s, the cloud chamber, which measured individual particle paths, led to the conclusion that not only were cosmic rays charged but they were largely electrons. A Frenchman named Pierre Auger decided to put the coincidence of gieger counters to the test in 1933 by separating them by ever increasing distances. The rate of coincident triggers decreased as the counters became further and further spaced, however, even at a distance of 300 meters he still found they would occasionally trigger in coincidence. This led him to the idea that cosmic rays were actually a shower of particles all created at the same time by a single progenitor. The shower traveled downward spreading out while it evolved, much like the wake behind a boat. Placing a cloud chamber at various locations between the gieger counters allowed an estimation of how the density of particles varied, and using this information plus the area covered he figured out the approximate number of particles in one of those rare showers able to trigger his counters separated by 300 meters. He multiplied that number by the average energy of the particles which happened to be 10 MeV (10 million electron volts, for comparison a photon of visible light is $\sim$1 electron volt). In this way he made a crude estimate of the energy of the progenitor that was an astounding 10 trillion electron volts: and this calculation didn't even allow for energy loss in the atmosphere. Today the energy of a cosmic ray is measured in the same way with the only improvements coming in the technical arena - the theory has

remained unchanged. This is why the Pierre Auger Observatory bears his name.

1.1.3 Connections to particle physics

Cosmic rays are often referred to as the result of nature's accelerators. This observation is both accurate and misleading but it is worthwhile to explore the extent to which cosmic ray physics has influenced particle physics and what further cross-disciplinary possibilities still remain.

Without a doubt cosmic rays yielded the first evidence for some of the earliest sub-atomic particles discovered. A great breakthrough occurred in 1937 [8] with evidence for intermediate mass particles[5] because this upset the current view of the sub-atomic world. Rabi, a renowned physicist from Columbia, famously remarked, "Who ordered that?" when faced with the new particle. His surprise stemmed from the fact that the muon had no obvious role in the world. It had all the properties of an electron, except for a mass about 205 times heavier. The discovery of something unnecessary provided a spark for further investigation and sure enough before long pions and positrons were discovered in cosmic ray showers. With the advent of man-made accelerators new particles became easier to find and the list grew at an increasingly rapid pace until scarcely a year went by when a new particle **wasn't** discovered. Accelerators had an advantage because they provided a more controlled experimental environment and for that reason the interest of particle physicists in cosmic rays waned for a period. It has since been renewed though because upon collision with the atmosphere the highest energy cosmic rays reach a center of mass energy approximately two orders of magnitude higher than the world's largest accelerator, the Tevatron at Fermilab, and therefore could probe the standard model in ways a conventional accelerator

[5]particles with a rest mass between that of electrons and the much heavier protons/neutrons

can't. Even the creation of such an energetic particle in the first place poses interesting particle physics possibilities with dark matter, big bang relics, and GUT[6] scale decays at the top of the list. These intriguing possibilities ensure that particle physicists continue to keep an eye on the developments in the field of cosmic rays.

1.2 Air-Shower Phenomenology

The Pierre Auger Observatory is designed to detect the most energetic cosmic rays ever observed with an expectation that several events will exceed 1×10^{20} eV per year. These events are at the very end of the known spectrum (see fig. 1.2) and because of the rarity, require a detector of enormous size to catch just a few. This rules out the possibility of building the device anywhere except on the ground. Relegated to the surface of the Earth, direct detection of the cosmic rays' is out of the questions; they always interact with the atmosphere first and produce a cascade of particles that subsequently interact themselves continuing the cascade. The process is called an air shower and the ultra-high energy cosmic rays the Pierre Auger Observatory is optimized to detect result in truly monumental showers[7] containing tens of billions of particles.

1.2.1 Shower profiles: longitudinal and lateral

Although a giant air shower begins with a single particle interaction the cascade quickly becomes stochastic due to the large numbers of particles produced. It

[6]GUT stands for Grand Unified Theory - a replacement or revision of the standard model of particle physics that includes a unification scheme for the electromagnetic, strong, and weak forces

[7]some showers detected at the observatory have covered an area greater than 65 km^2

is therefore convenient to take a broad view of shower development rather then speaking about the paths of individual particles. As the shower progresses downward through the atmosphere the electromagnetic component can be described by a smooth function called the gaisser-hillas function 1.1.

$$\mathrm{N(X)} = \mathrm{N_{max}} \cdot \left(\frac{\mathrm{X} - \mathrm{X_0}}{\mathrm{X_{max}} - \mathrm{X_0}} \right)^{\frac{\mathrm{X_{max}} - \mathrm{X_0}}{\lambda}} \cdot e^{\frac{\mathrm{X_{max}} - \mathrm{X_0}}{\lambda}} \tag{1.1}$$

It is similar to a guassian and reflects the fact that the number of particles increases rapidly in the first several generations while the energy carried by the particles is well above the inelastic interaction cross-section. However the more particles are created the wider the original energy is distributed thus lowering the average energy per particle and slowing the production of new ones down. Eventually a threshold is crossed at which point absorption becomes the dominate process and the number of particles in the shower begins to decrease in an approximately exponential manner.

The passage of so many electrons through the air causes nitrogen molecules to be excited and fluoresce. By observing the number of photons produced by air fluorescence the process of shower development can be directly measured. Furthermore since the electromagnetic component accounts for $\approx 90\%$ of the total energy in a shower the energy produced by fluorescence is directly proportional to the energy of the primary cosmic ray.

$$\#\text{ of Air Fluorescence Photons} \quad = \quad \alpha \cdot \frac{dE}{dX} \tag{1.2}$$

$$\sum N_\gamma \propto \text{Total Energy} \tag{1.3}$$

The strength of using the fluorescence method is the ability to directly observe a nearly calonometeric energy deposit. Other benefits include direct observation of the depth of shower maximum (the parameter $\mathrm{X_{max}}$ from equation 1.1, which

turns out to be one of the best parameters for composition measurements), and a highly constrained geometry from the long vertical tracks. The greatest difficulties are accounting for the atmospheric conditions, the necessity to know both the fluorescence yield (equation 1.2) and the absolute number of photons that reach the detector accurately. Further complicating matters are an acceptance that depends on the shower brightness[8] and the operation is restricted to dark nights.

During the longitudinal development described above the shower also spreads outward from its axis laterally. The particles off-axis are fed from interactions in the core[9] and thus follow the same pattern as the longitudinal development, but lag that of the core, occurring at deeper atmospheric depths by an amount determined by the extra radial distance.

The lateral distribution is measured normal to the shower axis by an array of ground particle detectors that can either be simple scintillating counters or detectors that are more sensitive to the energy deposit than the number of particles. In either case the exact functional form of the lateral distribution is dependent on the properties of the detector as much as it is the properties of the shower. It is sufficient to say that a power-law similar to 1.4 presented in "*Introduction to High-Energy Cosmic Ray Physics*" by Pierre Sokolsky who uses the NKG type function [9, 10, 11] is a good approximation.

$$\rho(r) = \frac{\mathrm{N}}{{r_1}^2} \cdot f\left(s, \frac{r}{r_1}\right)$$
$$\text{with the function f taking the form:} \tag{1.4}$$
$$f\left(s, \frac{r}{r_1}\right) = \left(\frac{r}{r_1}\right)^{s-2} \cdot \left(1 + \frac{r}{r_1}\right)^{s-4.5} \cdot \left[\frac{\Gamma(4.5-s)}{2\pi \cdot \Gamma(s) \cdot \Gamma(4.5-2 \cdot s)}\right]$$

[8] any number of factors contribute to how bright a shower appears

[9] the core is not a well defined region, for showers above 10^{18} eV the core can be thought of as a 100 meter radius cylinder coaxial with the shower axis

The advantages of a ground detector are the relatively simpler calibration and monitoring, a weaker dependence on atmospheric conditions, an aperture that is well defined, and the ability to function regardless of the outside light level. Surface detectors also have a much lower unit cost, but that is offset because more of them are required to be an effective instrument. The disadvantages are usually a poorer resolution of the arrival direction, and a reliance on computer simulations for energy and composition measurements.

1.2.2 Shower particle physics

The interaction of individual particles are not usually visible over the froth of the entire cascade but there is one conservation law that is particularly important: *the conservation of baryon number*.

Showers initiated by a baryon[10] primary (i.e. particles containing three quarks; a subset of all hadrons) give rise to a great number of hadronic secondaries because strong force interactions dominate the cross-sectional phase space. This is true even if some of the first interactions are not strong force processes. The conservation of baryon number ensures that the intial quark content survives and promptly will participate in a series of strong force interactions.

The great number of hadronic secondaries produced are overwhelmingly pions, two thirds of which are charged. Some of the charged pions may interact again but the strong force dominates here as well, resulting in ever greater numbers of pions. Inevitably a portion of the charged pions decay to a muon and a neutrino

[10]mesons are too short lived to be considered a viable candidate for primary cosmic rays

by the reactions shown in 1.5.

$$\begin{aligned} \pi^- &\rightarrow \mu^- + \overline{\nu}_\mu \\ \pi^+ &\rightarrow \mu^+ + \nu_\mu \end{aligned} \tag{1.5}$$

Thus showers initiated by a baryon have a characteristic muon component not seen in showers initiated by a non-baryon primary. The most common example of a non-bayon comsic ray is a primary photon which interacts largely via the electromagnetic force, leading to showers that are characteristically muon poor. Aside from the muon component the rest of the shower consists of photons, electrons, and positrons, collectively called the electromagnetic component, whose numbers are described by the aforementioned gaisser-hillas function 1.1. The production of electromagnetic particles is the result of direct electromagnetic interactions between charged particles in the shower and those in the atmosphere as well as the nearly instantaneous decay of the uncharged pions via 1.6.

$$\pi^0 \rightarrow 2 \cdot \gamma \tag{1.6}$$

1.2.3 The Pierre Auger Observatory

The observation of a particle cascade can be broadly classified as belonging to one of two categories already discussed:

1. the fluorescence detection method and;
2. the ground particle detector method.

They are complimentary techniques, one depending on the longitudinal profile and the other on the lateral distribution. Either is capable of functioning independent of the other and the strengths and weaknesses tend to run orthogonal making the combination of the two apparatus advantageous. The Pierre Auger

Observatory is the first experiment to use both techniques, combining four fluorescence sites with the largest ground array ever built. The plan and its current status are shown in fig. 1.4. Past experiments have only utilized one of the two methods and therefore have been largely concerned only with the longitudinal or lateral profile of a shower. Notably the Akeno Giant Air Shower Array (AGASA) [12] and the High Resolution Fly's Eye (HiRes) [13] have disagreed about the flux of the highest energy cosmic rays, probably stemming from the differences in detection techniques.

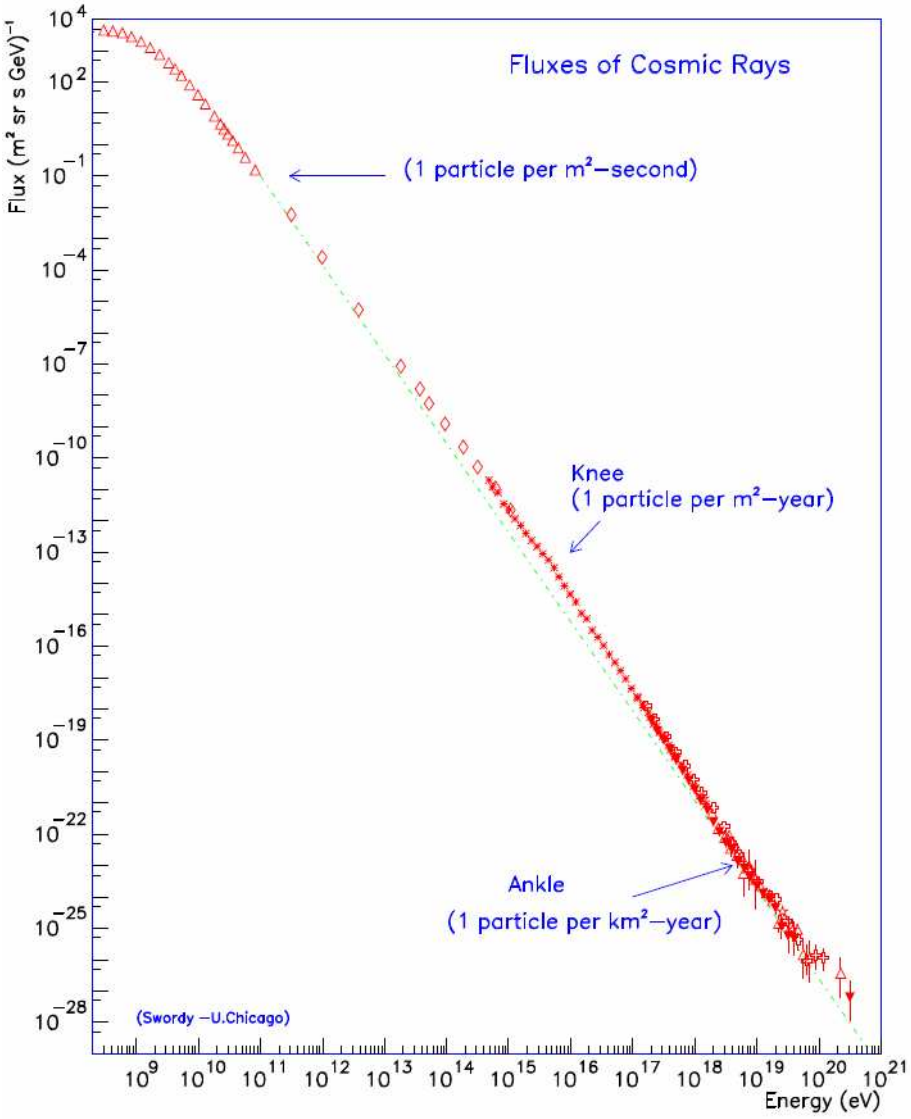

Figure 1.2: The world cosmic ray spectrum covering 15 orders of magnitude in energy. The detection techniques vary widely within this range. A particularly salient feature is an increase in energy corresponds to a decrease in rate of approximately $E^{-2.6}$ so that at energies above 1×10^{18} eV the flux is less than one event per square kilometer per century.

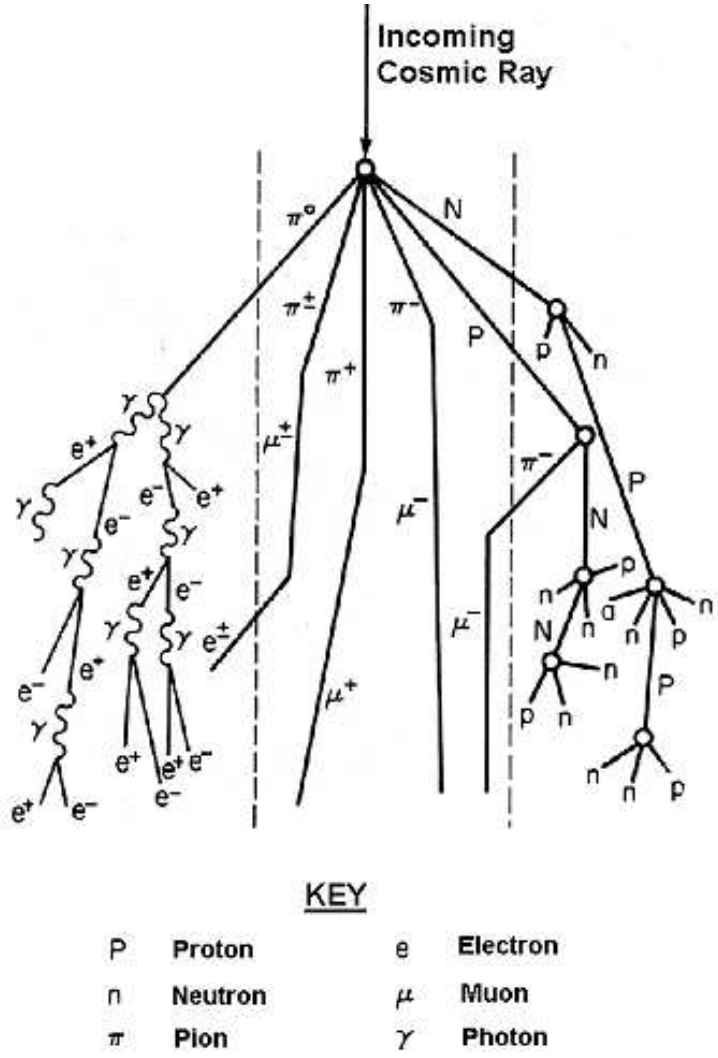

Figure 1.3: Example of the first several generations of a cosmic ray shower. Neutral pions decay in $\approx 10^{-16}$ sec often becoming gamma rays while the charged pions have a much longer lifetime $\approx 10^{-8}$ sec which allows them to further interact or decay to a muon and netrino.

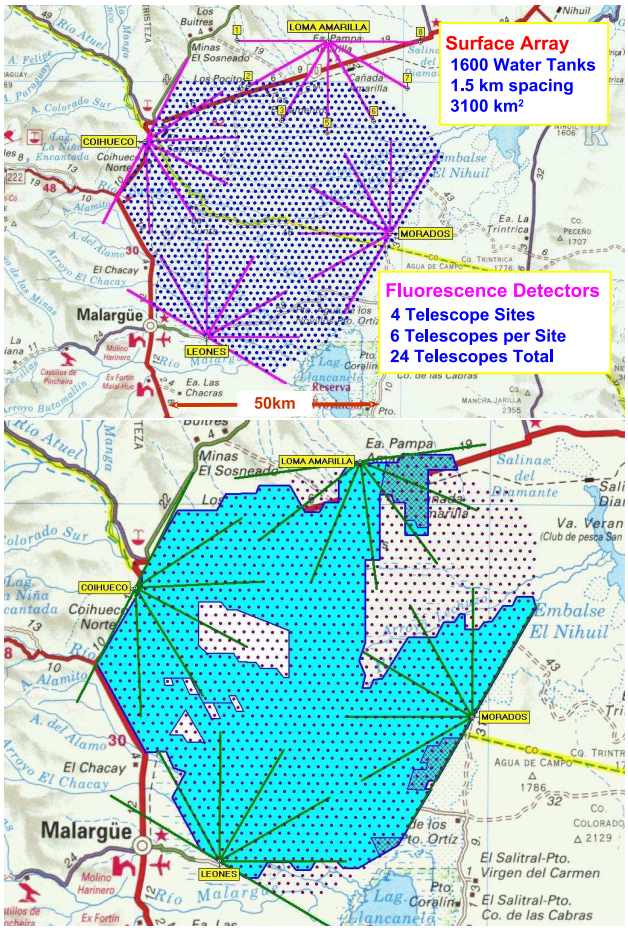

Figure 1.4: **Top:** The design of the Pierre Auger Observatory. It is located in Argentina and contains 1600 water-Cherenkov detectors as well as four fluorescence buildings each housing 6 telescopes. **Bottom:** The current status of array construction as of 22 April 2007. The four fluorescence sites are complete and 1326 out of 1600 station have been deployed.

CHAPTER 2

Theory

When studying ultra-high energy cosmic rays it is worth pointing out that very little is actually known which makes covering what is known that much more important. It is also wise to acknowledge the assumptions that are commonly made so we can differentiate what is certain from what is merely probable. Here is what we know for certain.

- There are ultra-high energy cosmic rays (E$> 1 \times 10^{18}$ eV)
- Ultra-high energy cosmic rays originate outside the Earth
- The flux of ultra-high energy cosmic rays is very-very low
- Ultra-high energy cosmic rays produce a shower of secondary particles that can be observed in the atmosphere and on the ground
- The number of secondaries has a smooth development and is related to the original energy of the cosmic ray
- The secondaries consist primarily of photons, electrons, and muons (in that order)

Using these certainties and a few logical arguments a menagerie of possible scenarios can be developed, beginning with the benign and ending with the exotic.

2.1 Bottom-up scenarios

The lowest energy cosmic rays are a product of the Sun. High temperatures and fluctuations in the magnetic field cause eruptions in the solar atmosphere spewing particles off the outer layers of the Sun resulting in an outward flow of charged particles called the solar wind. These cosmic rays permeate interstellar space out to a distance of $\sim$50 AU[1] and are so low energy they often become trapped in the magnetic field of the Earth causing a phenomenon known as an aurora when they rain down on the poles. Solar cosmic rays are abundant and well studied. They consist largely of protons with a mix of other stable particles.

At higher energies, cosmic ray origins are outside the bounds of the solar system with current evidence favoring energetic stellar phenomena such as supernovae and the plasma shocks they create. The tendency is for more energetic cosmic rays to be associated with increasingly more violent astrophysical events. At this juncture it should be noted that it is compositional evidence (see fig. 2.1) that suggests supernovae are involved proving that composition determination is an important measurement. A more direct method to associate cosmic rays with supernovae would be to match the arrival directions with the locations of supernovae. However this method is doomed to fail because comsic rays are charged particles and magnetic bending distorts the paths so much that the arrival direction often has nothing to do with the location of the source. In situations such as this there may be no alternative except to use compositional information as a basis for conjecture.

[1] an AU is an astronomical unit, the distance from the Sun to the Earth, about 93 million miles

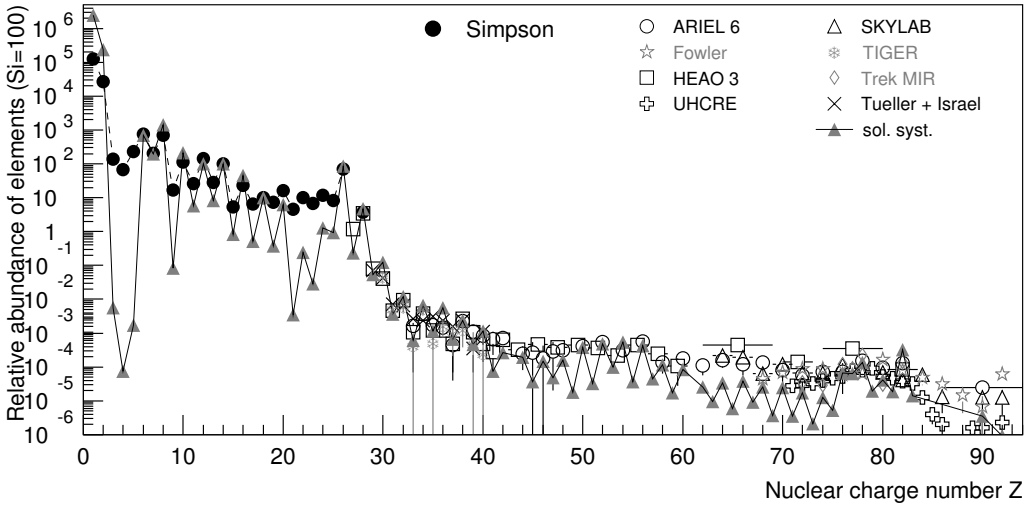

Figure 2.1: The compositon of cosmic rays above 1 GeV [14].

2.1.1 Magnetic fields and the galactic versus the extra-galactic

When talking about ultra-high energy cosmic rays it is convenient to break them into two categories, those that originate within our galaxy and those that originate elsewhere. It is well established that the Milkyway generates a galaxy wide magnetic field and this field tends to trap charged cosmic rays within. Containment is not perfect by any means but given a field strength of $\sim 1 \times 10^{-6}$ gauss even protons of 1×10^{18} eV travel in a nearly random fashion. If we assume cosmic rays originate in galaxies, and that those galaxies tend to have magnetic fields at least as strong as ours, it is unlikely that many of the cosmic rays below 1×10^{18} eV come from a galaxy other than our own.

As the energy increases containment by magnetic fields weakens and eventually disappears completely. If our galaxy contained a source of 1×10^{19} eV cosmic rays it should be easy to identify because the deflection in the magnetic field would be greatly reduced so the arrival direction **would** match the direc-

tion of the source. This hypothesis has been tested several times with some encouraging results [15, 16] but none has been confirmed [17].

In addition to the argument about magnetic fields, a feature in the shape of the energy spectrum often called the ankle[2] suggests a change in the properties of cosmic rays above the energy $\sim 3 \times 10^{18}$ eV. A good explanation is that this feature is the result of a transition from galactic cosmic rays to extra-galactic cosmic rays. It also naturally explains why there is a lack of direct correlation between source locations and arrival directions. For extra-galactic cosmic rays it is the extra-galactic magnetic field that matters. And although the strength is expected to be much weaker ($\sim 1 \times 10^{-9}$ gauss), this is more than offset by the fact that the distance scales are much larger. Simulations show (see fig. 2.2) that extra-galactic cosmic rays should not correlate with the sources unless the energy is $\sim 4 \times 10^{19}$ eV. The possibility that cosmic rays will point back to a source is a major motivation for the collection of as many events above this threshold as possible.

2.1.2 Acceleration mechanisms

A very thorough explanation of the most probable acceleration scenarios for cosmic rays from 100 MeV up to 1 PeV is given in [18]. Working backward using the observed composition as a function of energy and including the process of spallation[3] an argument is presented that matches what would be expected from stellar evolution. I will confine myself therefore to more exotic acceleration mechanisms needed to produce the highest energy cosmic rays.

[2]the cosmic ray energy spectrum contains two features called the knee and the ankle which resemble a change in shape similar to the way those joints change the shape of a human leg

[3]spallation turns heavier elements into lighter ones through collisions with interstellar matter

2.1.2.1 Fermi shock acceleration

Fermi acceleration is actually two possible theories where I will concentrate on the one known as *first-order Fermi acceleration* because it has the advantage that incremental changes in the particle energy during acceleration are $\frac{\Delta E}{E} \approx \frac{2 \cdot V}{c}$. A detailed description of both processes is available in [18]. Fermi acceleration works by placing a gas of low energy cosmic rays in a plasma that contains mechanical waves known as shocks. The cosmic rays repeatedly interact with the shocks gaining energy each time. In the case of first-order Fermi acceleration the shocks are supersonic and the energy gain of a particle that collides with the shock can be calculated by considering an inertial frame comoving with the shock. In this frame the particle has a relativistic energy-momentum tensor given by the following equation.

$$E_{comoving} = \gamma_{shock} \cdot \left(E_{particle} + V_{shock} \cdot |\vec{p}_{particle}|, \vec{p}_{particle} + \frac{\vec{V}_{shock} \cdot E_{particle}}{c^2} \right)$$

$$\gamma_{shock} \text{ is the usual Lorentz factor } \gamma = \left(1 - \frac{v^2}{c^2}\right)^{-\frac{1}{2}}$$

$$V_{shock} \text{ is the velocity of the plasma shock}$$

In this frame of reference the shock is stationary and the particle reflects elastically; energy conservation gives $E_{before} = E_{after}$. In the process the direction of the particle's momentum is reversed. In the observer's frame the energy of the cosmic ray is $E_{observer} = \gamma_{shock} \cdot (E_{particle} + V_{shock} \cdot \vec{p}_{particle})$ both before and after the collision. The change in momentum direction though gives an energy boost in the observers frame of:

$$\Delta E \approx \gamma_{shock}^2 \cdot E \cdot \frac{V_{shock}}{c}$$

In essence the particles bounce off the shock repeatedly gaining energy with each collision. The source of the energy is that of the shock itself because with each

collision it carries less energy. The shocks themselves are large, covering perhaps several parsecs so for all intents and purposes they are an infinite well of energy.

The greatest strength of first order Fermi acceleration is the natural progression to a power-law spectrum and the fact that it relies only on the generation of plasma shocks that are supersonic, something that surely happens in events such as a supernova explosion.

2.1.2.2 Direct field acceleration

A second interesting possibility is the neutron star. It is known that neutron stars pulse out radiation and the surface magnetic field is very strong ($\sim 10^{10-12}$ gauss). Combine this with the rotation period and any particle traveling near the speed of light at the surface will feel an electric field of $\approx 3 \times 10^{14}$ V m^{-1}. In a field that strong particles gain energy extremely rapidly. The ultimate limitation is set by the size of the pulsar with a typical value of E_{max} set by picking some standard values for a neutron star: B = 10^{10} gauss, L = 100 meters.

$$E_{max} \approx ZeBcL$$

$$E_{max} \approx 3 \times 10^{19} \text{ eV}$$

A good summary of candidate sources is fig. 2.3 which combines the strength of magnetic fields with the size of the object. Generally speaking, the bigger the object is and the higher the field strengths inside, the greater the energy that can be achieved.

2.2 Top-down scenarios

Another possible scenario is the creation of ultra-high energy cosmic rays from the decay of something much heavier. These are called top-down models because

the cosmic ray is not boosted to a high energy from an initial low energy state as in the case of bottom-up scenarios. In a top-down model the rest mass of the original particle is partially converted to kinetic energy of the decay products, one of which is a proton. There are several possible top-down theories but they all share one trait in common. The decays produce ultra-high energy gamma rays as well as ultra-high energy protons. This possibility has already been investigated by the Pierre Auger Observatory by looking for showers initiated by photons. None have been found [4]. The absence of photons places strong constraints on top-down models as potential cosmic ray sources.

2.3 The Greisen, Zatsepin, and Kuzmin effect

Regardless of how a cosmic ray originates there is one final effect that is very important. The Griesen, Zatsepin, and Kuzmin (or GZK) effect [19, 20] is an interaction between cosmic ray protons and the ambient cosmic microwave background photons[4] present throughout all of space. Above a cosmic ray energy of about 4×10^{19} eV the center of mass energy is such that one of the quarks inside a proton can be kicked into an excited state turning the proton into a Δ^+. The Δ^+ then decays as in equation 2.1.

$$\begin{aligned} \Delta^+ &\rightarrow p \ + \ \pi^0 \\ \Delta^+ &\rightarrow n \ + \ \pi^+ \end{aligned} \tag{2.1}$$

In the first decay the proton is recovered but its energy has been reduced when compared to the proton before excitation.

This is the essence of the GZK effect. Above a critical energy cosmic ray protons have a limited lifetime set by the frequency of interaction with CMB

[4] the cosmic microwave background are the 2.7° K photons left over from the big bang. They were discovered by Penzias and Wilson in 1965

(cosmic microwave background) photons. The mean free path decreases rapidly above the GZK energy as seen in fig. 2.4 limiting the distance to sources, especially for cosmic rays with energies above 10^{20} eV. One intersting note about fig. 2.4 is the travel length for iron exceeds that of a proton within a certain energy range. This is because the travel length for nuclei are set largely by the cross section for photo-disintegration rather than the traditional GZK interaction. Photo-disintegration is the breakup of a nucleus into multiple pieces, each an element lighter than the original but sharing the kinetic energy. This turns one cosmic ray into several but each with an energy less than the original.

The effect of this interaction on the cosmic ray spectrum is often described as a cut-off above the GZK energy. This is a bit misleading because super-GZK events (those with an energy greater than the GZK energy) are allowed. Still unless the sources are within a sphere whose radius is set by the GZK mean free path a distinct suppression in the number of cosmic rays above the cutoff will be observed. At the highest energies the sphere is so small that unless cosmic rays are the result of a top-down decay it is almost certain they originated beyond that bound. Fig. 2.5 is the measured Pierre Auger spectrum with two theoretical predictions for the flux. Notice the suppression in the flux above the GZK energy.

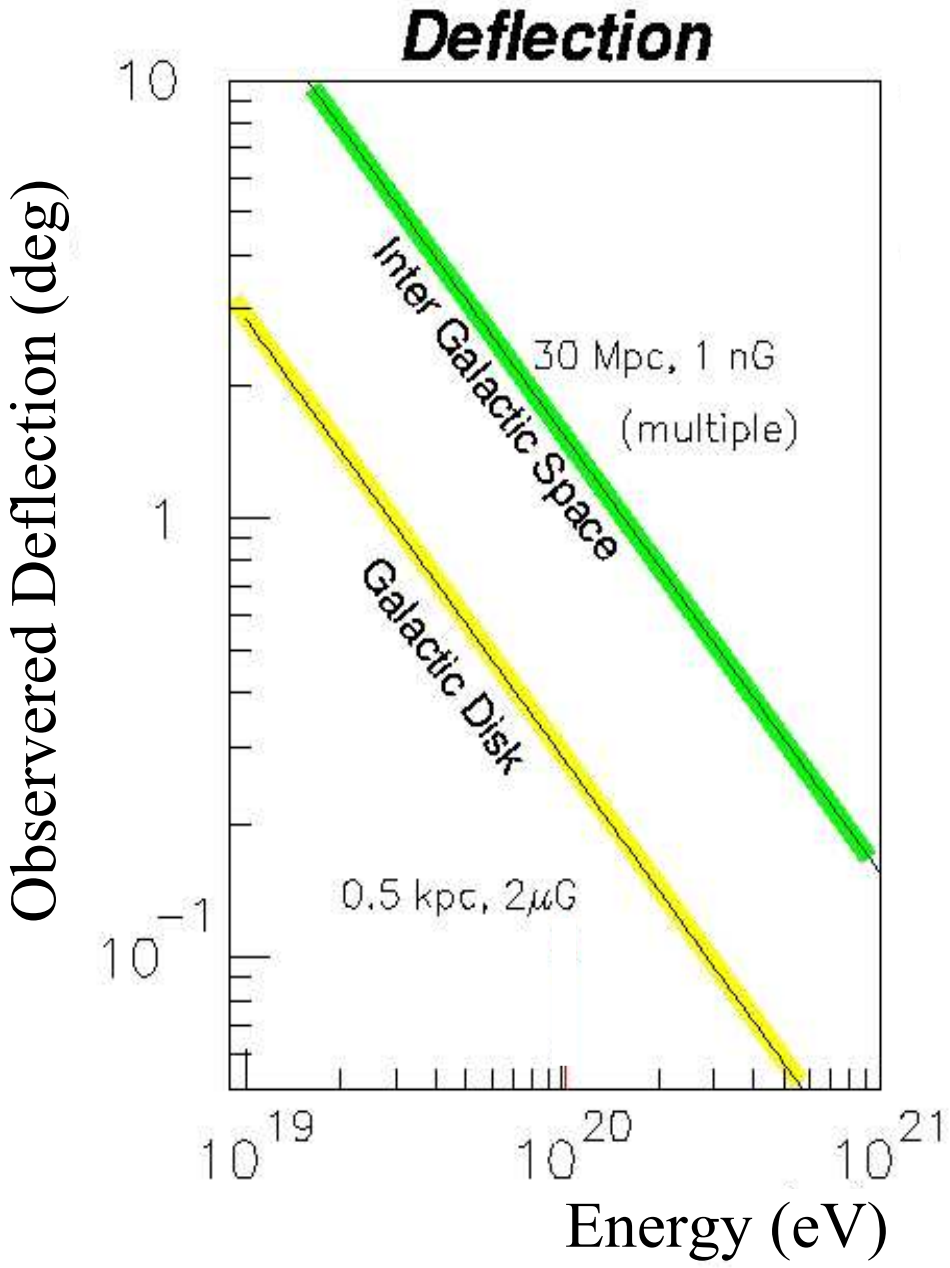

Figure 2.2: The deflection angle for protons of a given energy in a magnetic field. The colored lines correspond to typical values of the galactic and extra-galactic fields. The deflection assumes a primary with Z=1 (a proton); heavier primaries will bend more.

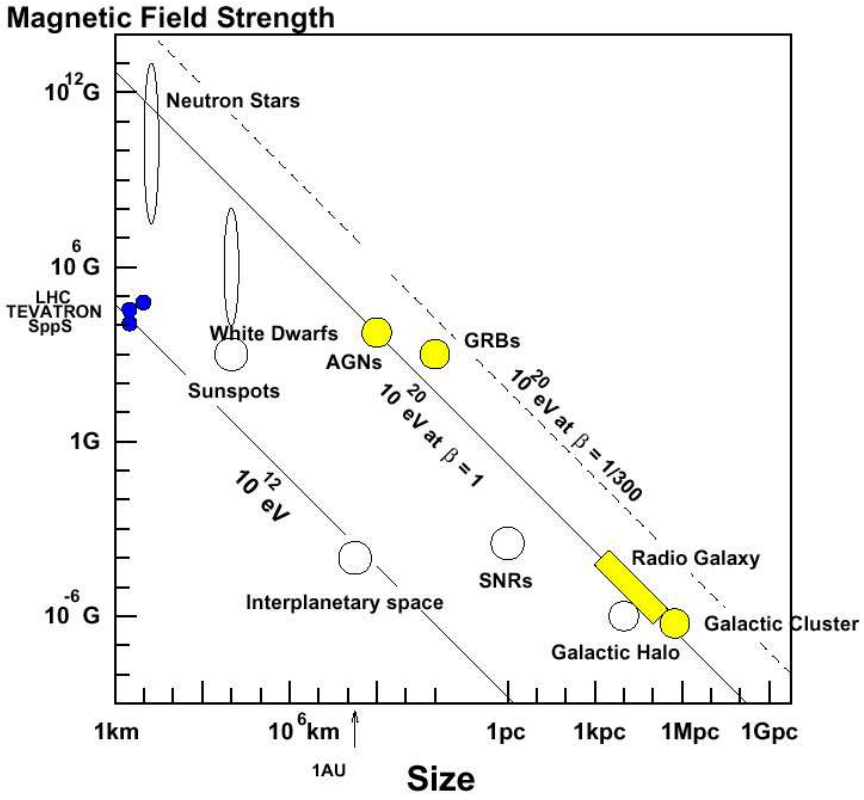

Figure 2.3: A collection of astronmical objects plotted by size and approximate magnetic field strength. Those colored yellow are considered "most" favorable as sources of ultra-high energy cosmic rays. The β parameter is an efficency factor for acceleration.

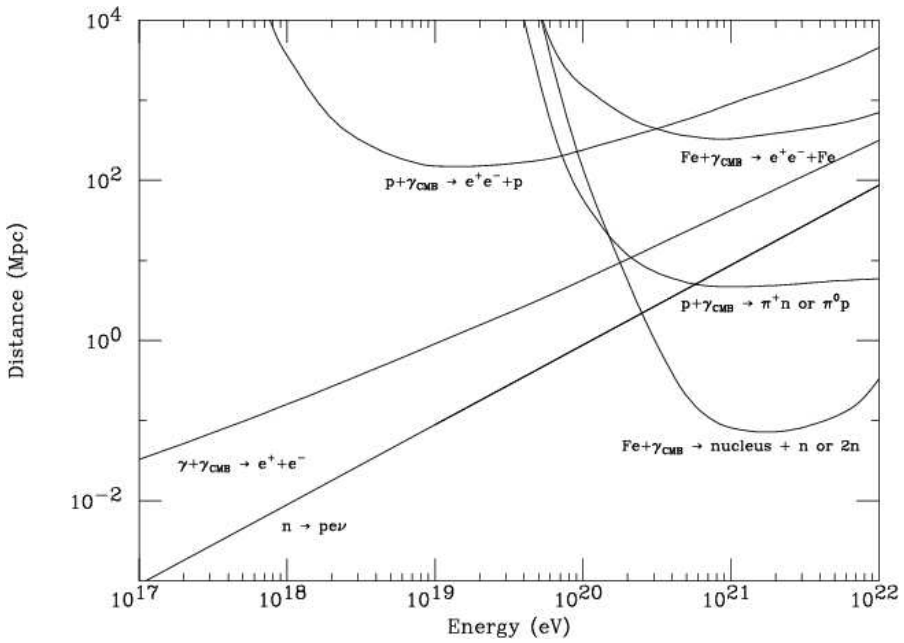

Figure 2.4: The mean free path for cosmic rays of various energies. The effective travel length decreases rapidly above the GZK energy.

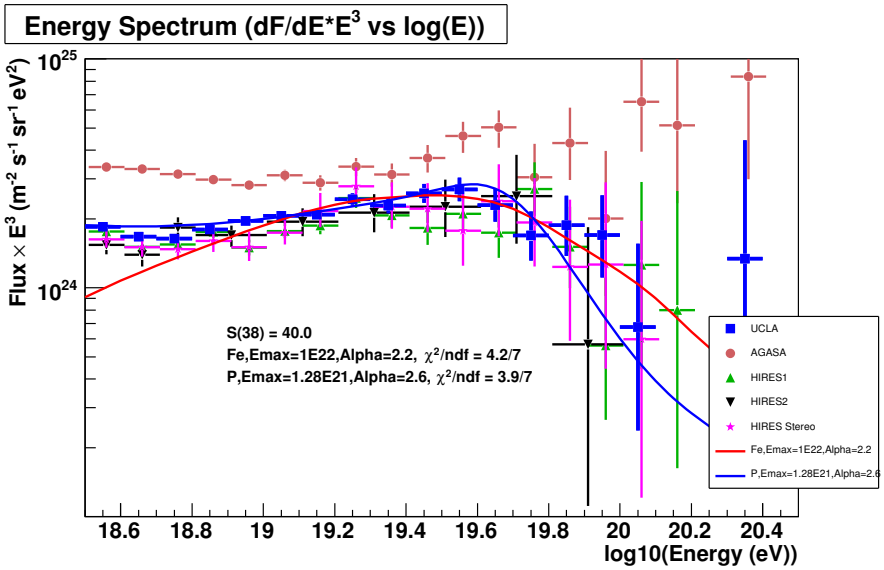

Figure 2.5: The two predictions (proton and iron) are based on cosmic ray sources uniformly distributed throughout the universe that produce only protons, or only iron. For this distribution of sources many lie outside the GZK sphere and the flux is therefore suppressed above the GZK energy. The models include the products of photo-disintegration in the case of iron. The data are the measured flux of the Pierre Auger surface detector and other experiments.

CHAPTER 3

Technical Description of the Detector Elements

3.1 The Pierre Auger Surface Detector

3.1.1 Layout of the array

The Surface Detector (often referred to as the SD) is an array of water cherenkov detectors regularly spaced in a repeating pattern. The fundamental geometrical form in the array is an equilateral triangle with one and a half kilometer sides. Individual triangles share a single side in common and six of them together form a hexagon. It is not an accident that the first level physics trigger (referred to as a T3) is a triangle of triggered detectors and the event quality trigger (referred to as a T5) is a hexagon of currently active, but not necessarily triggered, detectors [21].

The array spans an area of roughly three thousand square kilometers and the total shape resembles a hexagon. The placement of individual detectors is done by a surveyor using traditional tools as well as a GPS locator. The usual tolerance for placement is plus or minus ten meters [22]. The layout of the array is designed to maximize the sensitivity near threshold but still space detectors enough so that the aperture is large enough to detect a statistically significant number of the comparatively rare, but thereby more interesting, GZK or super-GZK events [19, 20].

3.1.2 Components of a detector

Each detector in the array holds twelve tons of ultra-pure water in a cylindrical polyurethane container. The inner walls of the container are lined with a Tyvek® bag because of it's non-reactivity and its optical properties in the near ultra-violet. Three nine inch photo-multipliers arrayed in a triangle look down through windows at the top of the Tyvek® bag. Each photo-tube face is coupled to the plastic window with an optical glue. The photo-tubes are behind a light trap and then covered by a metal hatch that is secured to the external surface of the detector. Coaxial cable and an RS-232 cable connect the photo-tubes to an electronics and power supply box that handles all the on-detector monitoring and data analysis. Electricity is supplied by a solar panel and two lead acid batteries for operation during the night or on cloudy days. Location and time synchronization is provided by a GPS antenna and communication to the central campus is achieved by an ad-hoc network operating via microwave radio.

3.1.2.1 Water

The surface detectors use twelve tons of deionized water as a medium for the production and transmission of cherenkov light. Since vertical muons are used as the calibration benchmark it is important that sufficient light is transmitted to the photo-multiplier tubes to produce as strong a signal as possible while still maintaining the dynamic range for large air showers. To this end it is important to use ultra-pure water because it maximizes the attenuation length and prevents future contamination due to bacteria growth because the medium is largely sterile.

The benchmark is a resistivity greater than 15 MOhm cm at a production rate sufficient to maintain the rate of deployment of the array. This is achieved using an on-site purification plant that employs a three phase process [22].

Pre-processing A physical filter, chemical decontamination, and finally ultra-violet sterilization

Reverse osmosis A high-pressure pump forces 2300 L h^{-1} through 4 membranes

Continuous electrodeionization A set of membranes designed to capture both positive and negative ions followed by continuous circulation through a 254 nm, 151 watt ultra-violet sterilization chamber

The input water is a mixture of water from the city of Malargüe and an on-site 80 meter deep well. The total system output is 36,000 L day^{-1} that can be transferred to a truck for deployment to new stations in the field.

3.1.2.2 Photomultiplier tubes

The photomultiplier tubes are custom manufactured by the Photonis© corporation. The photocathode area is 9 inches in diameter, with a ten stage dynode chain, and a nominal gain of $1{\times}10^6$ at 2000 volts. The photo-tubes are connected to an integrated base that contains a high voltage supply, resistor chain, and analog readout. The high voltage supply steps up the input voltage to a value determined by the detector's self-calibration system and is on the order of 1200 volts. The resistor chain then divides the high voltage among the various dynode stages. The photo-tube contains two readout channels identified as the dynode and the anode. The dynode channel is attached to the last dynode and the anode is taken from a fine wire mesh between the last and second-to-last dynode. Since the signals are taken from slightly different locations within the dynode chain they differ in size by a small amount. The base contains an amplifier for the dynode channel multiplying the signal by forty times that when combined

with the original difference yields a net amplification of the anode signal of about 32 times. The specifications by the Pierre Auger Collaboration are:

- Photo-tube diameter of 8" - 10"
- Cathode sensitivity Sk $> 50\mu$A/lm; Skb $> 7\mu$A/lm-B; quantum efficiency at 350nm $> 16\%$
- Gain of $2 \cdot 10^5$ with a supply of 1600 volts or less; gain of $1 \cdot 10^6$ with 2000 volts or less
- Dark current at a gain of $1 \cdot 10^6 < 20$nA; the dark current rate must be stable and vary by less than a factor of 10 between a gain of $2 \cdot 10^5$ and $1 \cdot 10^6$
- Dark pulse rate $<$ 10kHz at a gain of $1 \cdot 10^6$
- Linearity of better than 5% up to a peak current of 50mA at a gain of $2 \cdot 10^5$
- Single photo-electron resolution, the peak to valley ratio, at a gain of $1 \cdot 10^6$ must be > 1.2 times
- Time resolution for a single photo-electron at a gain of $1 \cdot 10^6$ must have FWHM of $<$ 10.0ns and a risetime of $<$ 6ns

3.1.2.3 Electronics box

The electronics box seen in fig. 3.1 is responsible for all on-station data analysis and monitoring as well as communication via an attached radio unit to the central data acquisition system (CDAS) [23]. It is situated under a protective hatch that sits atop of each station allowing easy access in the event that manual maintenance is required. Within the electronics box are three front-end boards

that each contain two analog to digital converters running at 25 MHz. Each of the three front-end boards match one of the three photomultiplier tubes and is responsible for the digitization of signals received. Each photo-multiplier tube has two analog outputs, the anode and the dynode often referred to as the low gain and the high gain channel respectively, and therefore each front-end board contains two analog to digital converters (a schematic is seen in fig. 3.2). The station level trigger, called a T2, is formed by a three-fold coincidence of signal from each of the photo-multiplier tubes. Upon a trigger the electronics box stores the digitized signal beginning 250 nanoseconds before the trigger and 6 microseconds after in a buffer while the trigger information is communicated to CDAS. In the event several stations trigger to form a larger array level trigger CDAS will request digitized signals from all stations that have them regardless of whether or not the station participated in the array level trigger. The electronics box is also responsible for tagging the triggers with a time stamp obtained from a GPS (global positioning system) antenna, monitoring hardware and data quality at a station level, as well as self-calibrating the station.

3.1.2.4 Supporting structures

Each station (see fig. 3.3) contains a number of supporting components that allow the primary components to function. These include two lead-ion batteries [24], a forty watt solar panel [25], a microwave radio, a GPS receiver [26], and an antenna for the radios [22].

3.1.3 Event detection and recording

Cosmic rays are detected by the secondary particles produced when the original primary interacts in the upper atmosphere. The ultra-high energy cosmic rays of

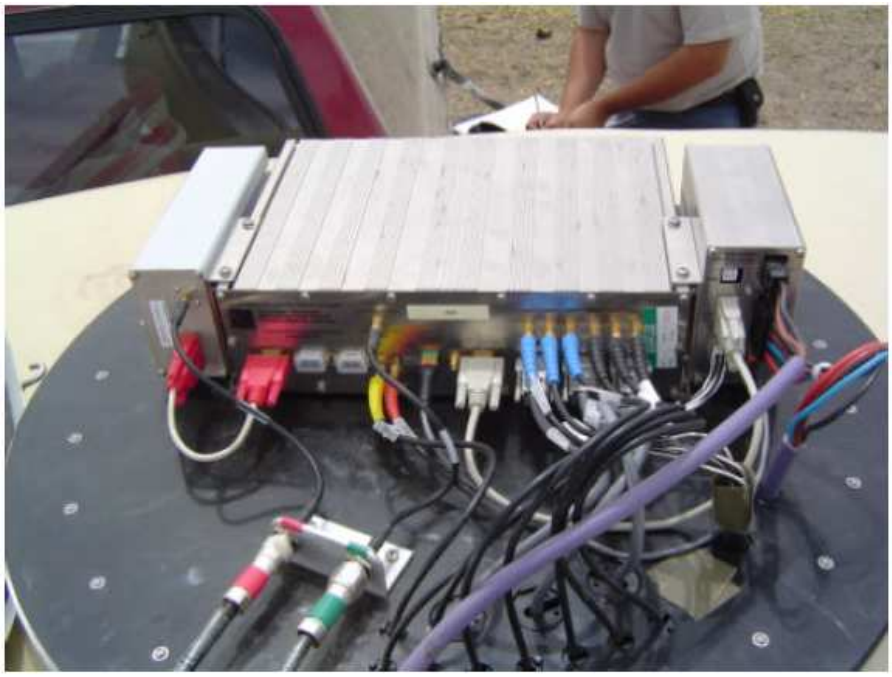

Figure 3.1: The electronics box is shown with the protective hatch removed. The cables connect the box to a power supply, the photo-tubes, and the two radios.

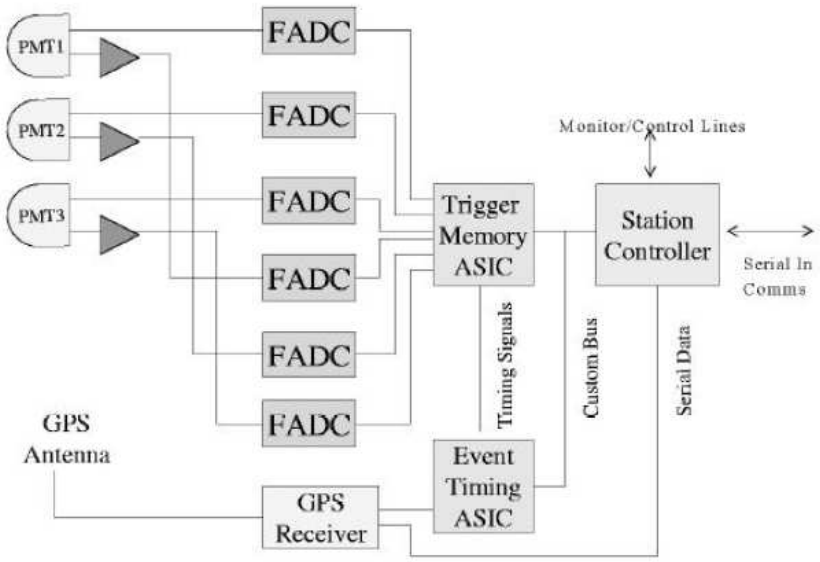

Figure 3.2: The electronics box contains the elements for digitizing photo-tube signals as well as low level trigger and timing circuitry.

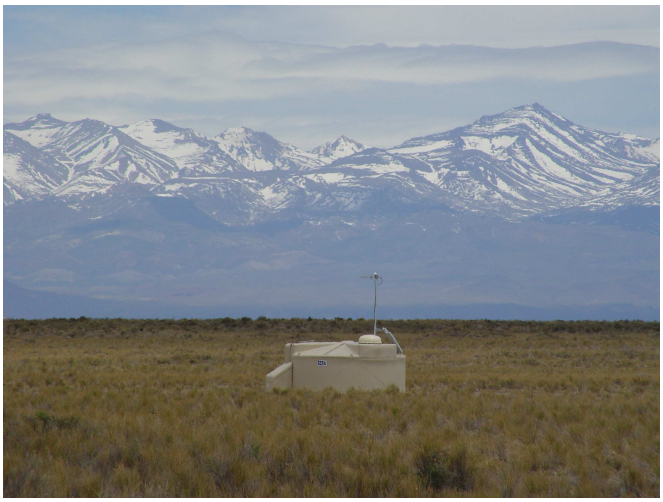

Figure 3.3: A surface detector station on the Pampa. Note the attached components, antenna, solar panels, etc. The photo-tubes and water are contained inside the plastic shell.

interest to the Pierre Auger Observatory create showers of secondaries that hit multiple detectors on the ground creating what we call an event.

3.1.4 Event triggering

Cosmic ray events are triggered by a series of three triggers that occur in stages and are therefore labeled as T1, T2, and T3. A T1 trigger is a single photo-tube with signal above threshold and can be triggered by the passage of any particle in the water of the detector whether it is from a cosmic ray shower, background radio activity, or even thermal emission in the photo-tube. The second level trigger or the T2 is a time coincidence of all three photo-multiplier tubes above threshold. This trigger is less subject to thermal emission and is primarily satisfied by the passage of single muons through a station. These muons are cosmic ray in origin but overwhelmingly from low energy cosmic rays (energy $< 10^{17}$eV) which produce a ground level flux of muons of about 80Hz per square meter. It is these cosmic rays that account for half the yearly radiation exposure at the Earth's surface. The T3 trigger is the first trigger that is designed to detect cosmic ray event of interest. In this case the coincidence is expanded to a geometry of triggered stations within the array. The basic trigger is a 3TOT, or 3 stations all with a time over threshold trigger. The three stations must be nearest neighbors and form a triangle with the station that contains the largest signal [21]. There is a secondary trigger that requires four station in the same basic configuration but does not require they all have a time over threshold condition. This 3$^{\text{rd}}$ level trigger known as a 4C+1 trigger is designed to detect very inclined showers.

3.1.5 Event recording

Every 3rd level trigger, either 3TOT or 4C+1, is followed by a readout request to all stations that have data regardless of whether the station was involved in the trigger or not. The data streams contain the digitized signals from the photomultipliers, timing information, as well as a calibration block that contains the most recently available calibration for the local station. The streams from each responding station are combined by the CDAS [23] and stored as a binary image using the ROOT [27] analysis package. These files usually contain many T3 events and typically cover a twenty four hour time period.

3.2 The Pierre Auger Fluorescence Detector

The fluorescence detector operates largely independently of the surface detector with only trigger information shared in real time. The motivation for this arrangement is the complementary measurement of some cosmic rays for the purposes of cross-calibration and advanced studies where the additional information provided by a second detector plays a crucial role. To maximize the number of showers observed by both detectors there are four fluorescence *eyes* each placed along the perimeter of the surface detector with all four facing inward. Each eye covers the 180° section of sky up to an elevation of 30° above the surface detector in front of it (see fig. 3.4).

3.2.1 Telescope design

The four fluorescence eyes contain six separate telescopes (see fig. 3.5) each covering an area of 30° by 30°. At the fundamental level a telescope consists of a camera of 440 photomultiplier tubes each representing a spot on the sky and a

Figure 3.4: The Los Leones flourescene detector building as seen from a point below and in front. The hatch coverings are motorized, opening during dark night periods to observe air fluorescence. Each hatch is for a single telescope.

mirror to focus incident light onto the active detector elements [22]. Building the sky coverage out of several mirror-camera pairs keeps costs low while still providing the desired reconstruction accuracy. Incident fluorescence light travels though an aperture entering the telescope bay, is reflected back in the direction it came from and focused on the photo-tube camera. Optimization of the telescope design involves a number of trade-offs but can be summarized best in terms of the light deposit from a cosmic ray shower at the camera face.

> As bright as possible, with excellent spatial resolution but fully containable within a single photo-tube.

Furthermore, in so far as possible none of these properties should vary with the location of the incident light on the camera. Light collection is maximized by enlarging the collecting area and correspondingly the mirror that focuses the collected light on the photo-tubes. The mirror size is 3.8 meters $\times$ 3.8 meters with a radius of curvature equal to 3.4 meters. The camera faces the mirror, not the sky, at a position about half the radius of curvature and is 90 centimeters square [22].

3.2.2 Optical systems

A number of optical systems are employed to ensure the quality of light at the camera. First of all only light from the fluorescence of nitrogen is of interest so a filter covers the aperture between the bay and the outside world. The filter specifications are principally designed to be transparent to the 391 nanometer line for molecular nitrogen but other wavelengths are permitted [22].

- Transmittance > 0.80 at 391 nm and at least 0.72 for the nitogen spectrum as a whole

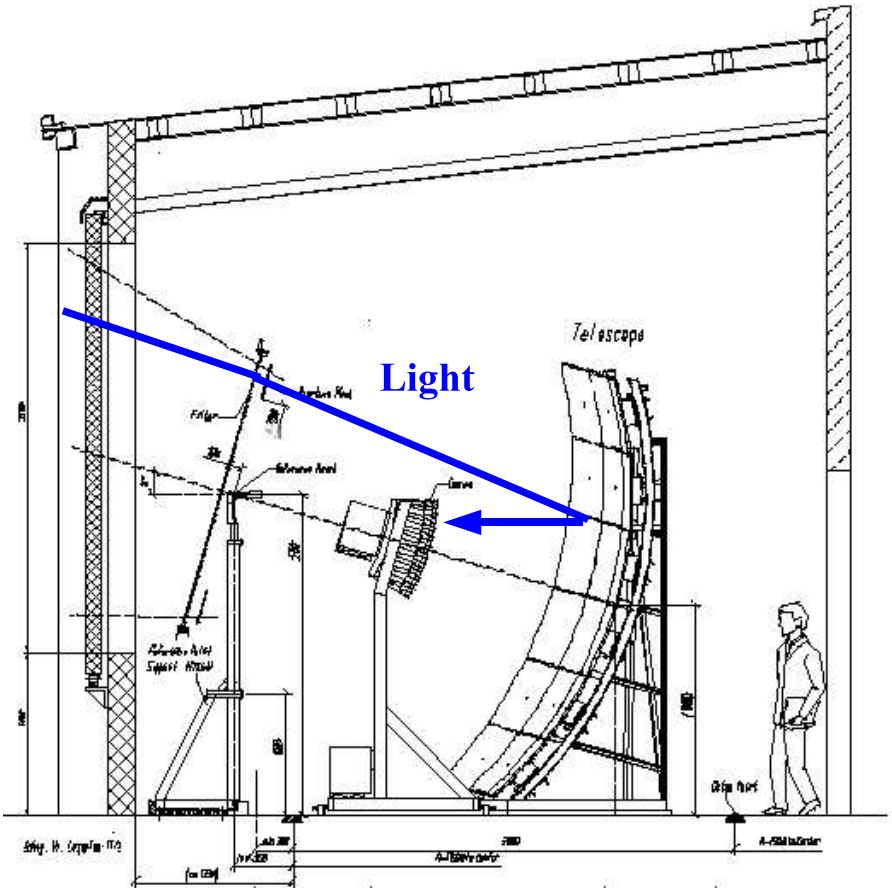

Figure 3.5: The path of light collection in a fluorescence telescope. The light enters from outside the building, is bent to correct for aberation, reflects off the mirror, and is collected at the camera.

- A ratio of 1.65 $\Rightarrow \frac{\text{nitogen transmittance}}{\sqrt{\text{sky transmittance}}}$

The wide field of view for each of the cameras requires a solution for coma aberation, or the elongation of point source light as the source appears further off the telescope axis. For this reason a Schmit diaphragm is employed to adjust the focus of incident light on the mirror surface. To further prevent the distortion of incident light near the edges of the diaphragm from spherical aberation a corrector ring annulus covers the outer 0.85 meters to 1.1 meters [22].

The mirror itself can be seen in fig. 3.6 and is a segmented design of thirty-six 0.65 $\times$ 0.65 meter square sections with a reflectivity in the range of 300-400 nanometers of greater than 90% . Each segment can be aligned individually with an overall tolerance for the whole mirror system of 2 millimeters in position and 0.2 mrad in angle [22].

3.2.3 Camera

The camera is a free standing structure between the aperture of the bay and the reflective mirror. 440 hexagonal photomultiplier tubes are arragned in honeycomb pattern with reflective *mercedes stars* separating the adjacent pixels. Each of the photomultiplier tubes contained within the bounding stars constitutes a single pixel of 1.5°. The size is chosen to allow an angular resolution on the shower axis of better than 0.5° [22]. The photo-tubes themselves are 45.6 millimeters in diameter and satisfy some quality assurance specifications.

- Linear to better than 3% up to a peak current of 10 mA
- The photo-cathode must have a uniform response of $\pm$15% over the entire surface

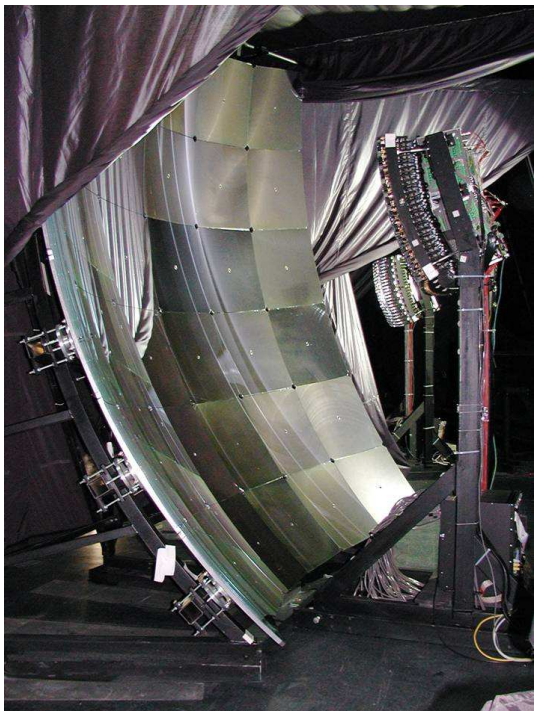

Figure 3.6: The segmented mirror design employed by the fluorescence telescopes. Light entering the building passes through a filter and corrector ring, reflects off the mirror, and is focused on a camera of 440 photomultiplier tubes.

- A half life of 350 coulombs[1].

The backplane of the camera consists of six layers of printed circuit board: high voltage, low voltage, two grounds, a signal, and a test. The entire unit is inclined at an angle of 15° with respect to the vertical and placed directly on the line of sight between the axis of the bay aperture and the mirror [22].

3.2.4 Event trigger

The trigger for the fluorescence detector begins at the level of an individual pixel. Each of the 440 photo-tubes is attached to an ADC that digitizes the analog output of the photo-tube to a range of 12 bits at a rate of 10 MHz. Even the darkest of night skies contain a significant photon background that is also time dependent: decreasing after sunset, increasing as dawn approaches, and varying with the position of the moon and ambient starlight. A fixed trigger level is therefore not practical and an averaging method is employed on the previous 10 digitizations. Each pixel is then sensitive to rapid changes in light level such as that associated with the momentary flash of a cosmic ray shower and the background is not relevant for the trigger as long as the ambient light intensity is below the light intensity expected from a shower.

The second level trigger is designed to capture coincidence between pixels to form an event. This is done with an FPGA that compares template patterns against the pixel triggers looking for a match. If one is found the trigger is passed and the event data is read out and stored for analysis. The patterns all contain five triggered pixels that are adjacent and more or less aligned[2]. If such

[1] given as the total charge integrated for all time at the anode for the gain to reduce to half its original value

[2] for instance, a blob of five pixels is not one of the patterns

a pattern can be found anywhere within the camera all channels are read out, even if they did not participate in the pattern match, and a fluorescence trigger is sent to CDAS which then requests any data from surface detector stations **whether or not there was a coincident surface detector trigger**. This allows the flourescene detector to form hybrid events even if the surface detector was insensitive to the event.

The ability for the flourescene detector to provide a trigger to the surface detector creates a major distinction between hybrid events, those for which the surface detector independently triggered (a golden hybrid event), and those for which it did not. A regular hybrid event, not golden, is better constrained during reconstruction than a fluorescene detector alone but in all other respects it is a purely fluorescene detector event. Golden hybrid events are much more useful, not only are they better constrained but they also independently measure many shower parameters because a surface detector event is fully reconstructable on its own, just like a fluorescence detector event.

CHAPTER 4

Water Quality and The Long Term Stability of the Surface Array

This chapter is an analysis I performed on a subsystem of the surface detector. It is necessary to investigate the properties of each subsystem to guarantee the reliable functioning of the entire instrument.

The Pierre Auger Observatory is designed to obtain the largest sample of ultra-high energy cosmic rays ever. Given the constraints on suitable locations, practicality, and money this goal is achieved by covering the largest area possible with ground detectors optimally spaced and running continuously. In fact the observatory is designed to run for twenty years and at this early stage it is important to know if the various components of the detector can continue to function for that length of time.

This chapter examines the long term functioning of the most important passive components of the surface detector, the water and the Tyvek®[1] bag that holds the water. Together these components govern the transmission of deposited Cherenkov light before it is received as signal in the photomultiplier tubes. A decrease in the transmission efficiency is a potential problem and could be an issue for the operation of the ground array.

[1]Tyvek is registered trademark of the DuPont corporation

4.1 Why does the Water Quality Matter?

Each station of the Pierre Auger surface detector is a water-Cherenkov detector which means that high energy particles entering the station are detected by the Cherenkov light created as they pass through the water. The individual photons bounce around the inside of the station until they are absorbed. Ideally absorption occurs only at the photocathode of one of the three photomultiplier tubes becoming part of the detected signal, however the water is not one hundred percent transparent nor is the Tyvek® one hundred percent reflective. Changes in the transparency of the water or the reflectivity of the Tyvek® affect the number of photons reaching the photocathode.

Of paramount importance is the ability of a station to detect the light deposit of a single vertical muon because that amount is used as the unit of measure to determine the energy deposited in any given station as the result of an extensive air shower [28]. The light deposit results in an electrical current that is integrated in time to give a charge that reflects the detected number of Cherenkov photons. The amount of this charge (hence referred to as Q_{VEM} - Vertical Equivalent Muon Area) is a fluctuating value dependent on a convolution of quantities ranging from static, such as the particular photomultiplier tubes in a station, to cyclic quantities like temperature. On a daily basis the most important of these is temperature [29] which results in a daily modulation of Q_{VEM}. This type of behavior was expected and is handled by the calibration and monitoring system which recomputes Q_{VEM} for each station every minute [30].

In principle, this system can measure the energy deposited in a station regardless of the calibration value obtained from vertical muons - but there are limits. Changes by a factor of two, so long as they occur over a time scale much longer than the one minute recalibration cycle, are not a problem, but we may

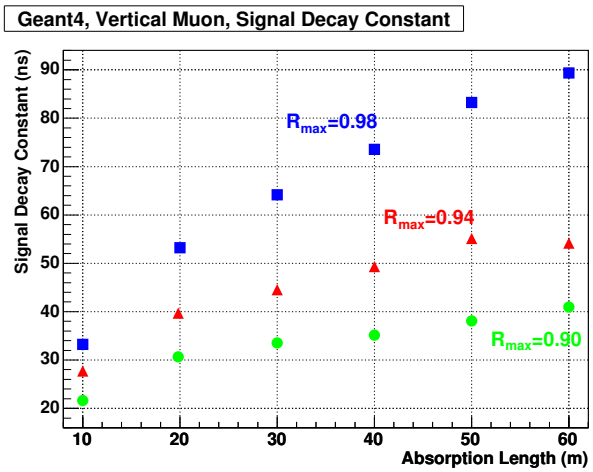

Figure 4.1: A monte-carlo simulation of how the Tyvek® reflectivity and absorption length in water (R_{max}) affect the signal decay constant from vertical muons.

not be able to correct for changes in Q_{VEM} by a factor of ten even if they occur over many years. Therefore the purpose of this study is to ascertain how much the value of Q_{VEM} is likely to change over the long term as a result of changes to the transmission of the water and the reflectivity of the Tyvek®.

4.2 Gauging the Rate of Cherenkov Light Absorption

The degree to which photons are absorbed can be measured by exploiting the diffuse scattering of the Cherenkov light. Diffuse light is detected at the photomultiplier tubes with a distinct time structure that is longer than the digitizing clock of 25 nanoseconds. When a muon passes through a station the amount of light detected rises sharply and then decays exponentially with a time constant dependent on the rate of photon absorption.

The time constant of the exponential, also called the signal decay constant,

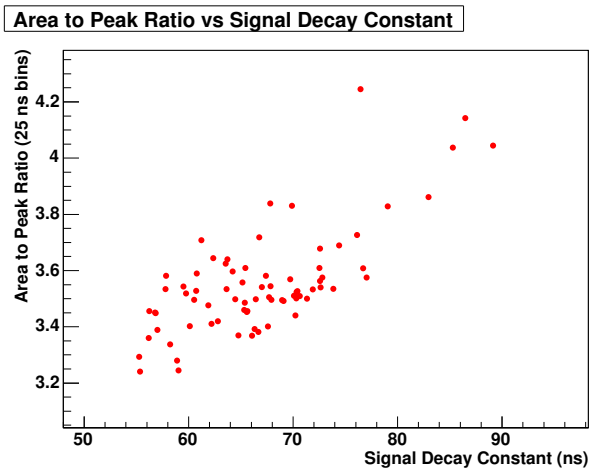

Figure 4.2: This example uses real stations to demonstrate the correlation between the area to peak ratio and the signal decay constant.

quantifies the amount of Cherenvok light that is absorbed in a way that is largely unrelated to the absolute photo-electron count. A shorter time constant indicates that photons are absorbed quickly inside the station, while a long time constant indicates that photons are allowed many reflections, traversing a lengthy path, before they are absorbed as seen in fig. 4.1.

It is advantageous to use this method rather than counting the absolute number of photons because absolute number depends on more than just the amount of absorption in a station.

Unfortunately direct use of the signal decay constant is hampered because it requires fitting the time structure of through going muons and the value of the time constant found is therefore dependent on the exact details of the fitting procedure. Nearly the same information can be obtained by simply dividing the maximal value of the time structure by its total area (see fig. 4.2 and fig. 4.3). The so called area to peak ratio is a routine monitoring quantity that is directly available with the monitoring information provided by the local station software.

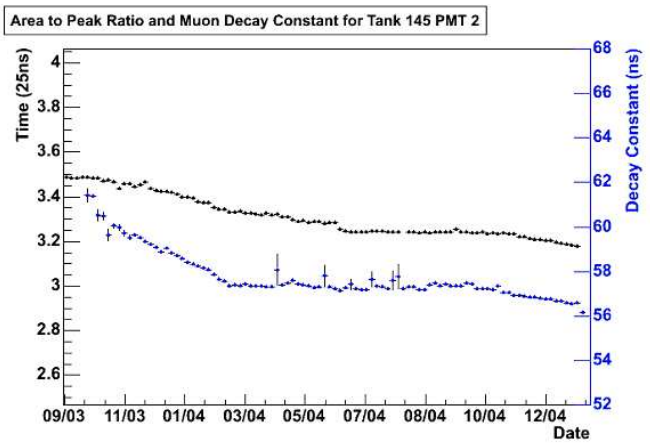

Figure 4.3: The area to peak ratio and the signal decay constant follow the same pattern of evolution within a station.

4.3 Long Term Trends in Water Quality

The number of stations has grown considerably during the construction phase of the observatory. Using the area to peak ratio we present the results obtained beginning with September 1, 2003 and ending with December 31, 2006. The total number of stations studied is seven hundred thirty-six with seventy-five of them available on September 1, 2003 so that the data obtained from these covers the entire twenty-seven month period. The remainder are stations deployed during the analysis period and therefore contain data from a fraction of the total period but are included provided they became available before May 1, 2005. This restriction is made so that all of the stations have had a minimum of twenty months to weather; allowing trends that may be multi-year or even multi-decade to exert an influence on the absorption of deposited Cherenkov light.

4.3.1 Functional Form of Water Quality

Previous work [31] showed that the area to peak ratio has a small positive correlation coefficient with temperature, therefore we expect a slight oscillation coupled to the annual temperature modulation. Examination of the evolution in the area to peak ratio revealed that nearly all stations have at least an initial period of decrease (seen in fig. 4.3 during the time period from September 2003 through June 2004). Combining these factors we decided to try and fit the observed behavior with one of two functions.

$$\text{A/P} = p_0\Big[1 - p_1 \cdot (1 - e^{\frac{-t}{p_2}})\Big] \times \Big[1 + p_3 \cdot \sin(2\pi(\frac{t}{T} - \phi))\Big] \quad (4.1)$$

$$\text{A/P} = p_0\Big[1 - p_1 \cdot \frac{t}{T}\Big] \times \Big[1 + p_3 \cdot \sin(2\pi(\frac{t}{T} - \phi))\Big] \quad (4.2)$$

Equation 4.1 is an exponential on top of a sine function. This allows for an initial period of decay followed by a stable point that oscillates in phase with seasonal changes. Equation 4.2 also allows for a decrease and a seasonal oscillation but the decreases does not slow down and stabilize over time.

The fit parameters are p_0 through p_3 with the following definitions; p_0 is the normalization with units of 25 ns bins, p_1 is the fractional loss (fraction of initial signal lost due to decay) and is a dimensionless quantity, p_2 is the characteristic time (time for the initial signal to decrease by $\frac{1}{e}$) with units of years and is only present in equation 4.1, p_3 is the seasonal amplitude (amplitude given as a fraction of the signal at the then current value) and is also a dimensionless quantity. The functions contain two additional parameters; T forces the period to be one year as we expect, and ϕ (a phase angle) adjusts the oscillation to coincide with the annual temperature oscillation. The independent variable t is the time in years.

4.3.2 Fitting Procedure

The monitoring data for all functioning stations is combined and processed to produce a time dependent record of the area to peak ratio for each photomultiplier tube. The data is binned into approximately five day intervals so that any daily fluctuations due to local weather phenomena are minimized. The time that each phototube first begins to take data is found and used as an offset to define t_0 of the fit[2]. Once the point t_0 is identified a chi-square minimization of the function yields the various fit parameters. A number of constraints are provided to improve the resultant fit.

1. The Overall Normalization (p_0) is constrained to the range of [1, 5.5] 25 ns bins

2. The Fractional Loss (p_1) must be between 0 and 1

3. The Characteristic Time (p_2) must be between 0 and 500 years

4. The Seasonal Amplitude (p_3) must be between 0 and 1 with an initial value of 0.005

5. The phase of the Seasonal Amplitude is allowed to vary in the range [0.1, 0.45] years with an initial value taken from the phase of oscillation in the average outdoor air temperature

The first condition (1) is based on the distribution of area to peak ratios from functioning stations recently deployed. The range is large compared to the width of the distribution and provides only a weak constraint on the fit. The second constraint (2) limits the fractional loss (p_1) to a range of 0% - 100% of the signal.

[2]In this way $t = 0$ is always two days before the first data point

This enforces the physicality of the measure. The constraints on the characteristic time (3) and the seasonal amplitude (4) are intended to enforce positivity, and in the case of the seasonal amplitudes the range reflects the small oscillations observed over the course of a year. The phase of the seasonal amplitude (5) is generally constrained to autumn in the southern hemisphere where the average outside air temperature is decreasing; a shift by π is forbidden.

Choosing which function to apply is decided by a goodness of fit test with the exponential on top of the sine (equation 4.1) attempted first (examples are shown in fig. 4.4 and 4.5). If $\frac{\chi^2}{\mathrm{NDF}}$ is greater than 500 or the Characteristic Time (p_2) is more than 10 years the linear function (equation 4.2) is tried and if it results in a smaller $\frac{\chi^2}{\mathrm{NDF}}$ the results of the alternate function are accepted (examples in fig. 4.6). If the linear function does not result in an improvement we revert to the results from the exponential fit. This procedure is repeated for every phototube of every station.

4.3.3 Quality Cuts

Hardware failures can occur at anytime and this is especially true during the deployment phase when the hardware is brand new (engineers call this *infant death*). Failures are detected with an on-line monitoring system and the maintenance staff is deployed to identify and fix the problem, either through repair or replacement. Depending on the parts serviced, the area to peak ratio may be unstable before maintenance and discontinous at the time of repair. Similar discontinuities can also occasionally arise during station recalibration, a procedure that has been done array wide several times during the period studied. For these reasons a series of cuts are employed to guarantee the accuracy of the fit.

The first step is a sweep to identify discontinuities within the measured area to

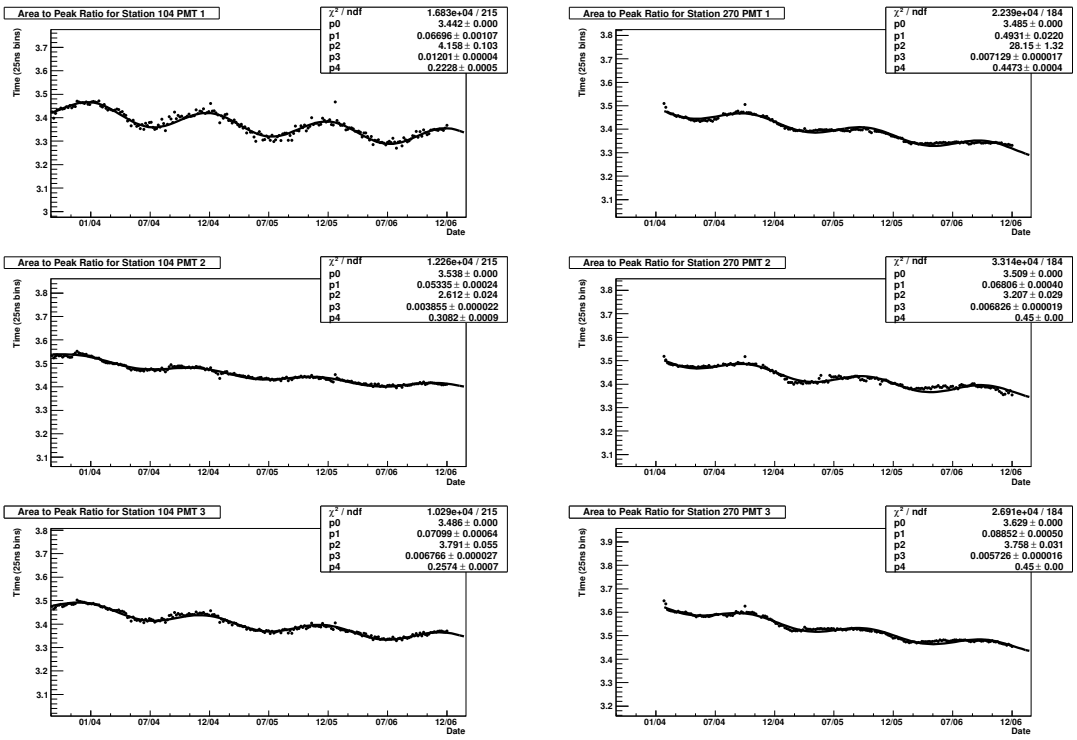

Figure 4.4: The fits to station 104 and station 270. The fits to the PMTs are best described by the exponential imposed on top of a sine function (equation 4.1).

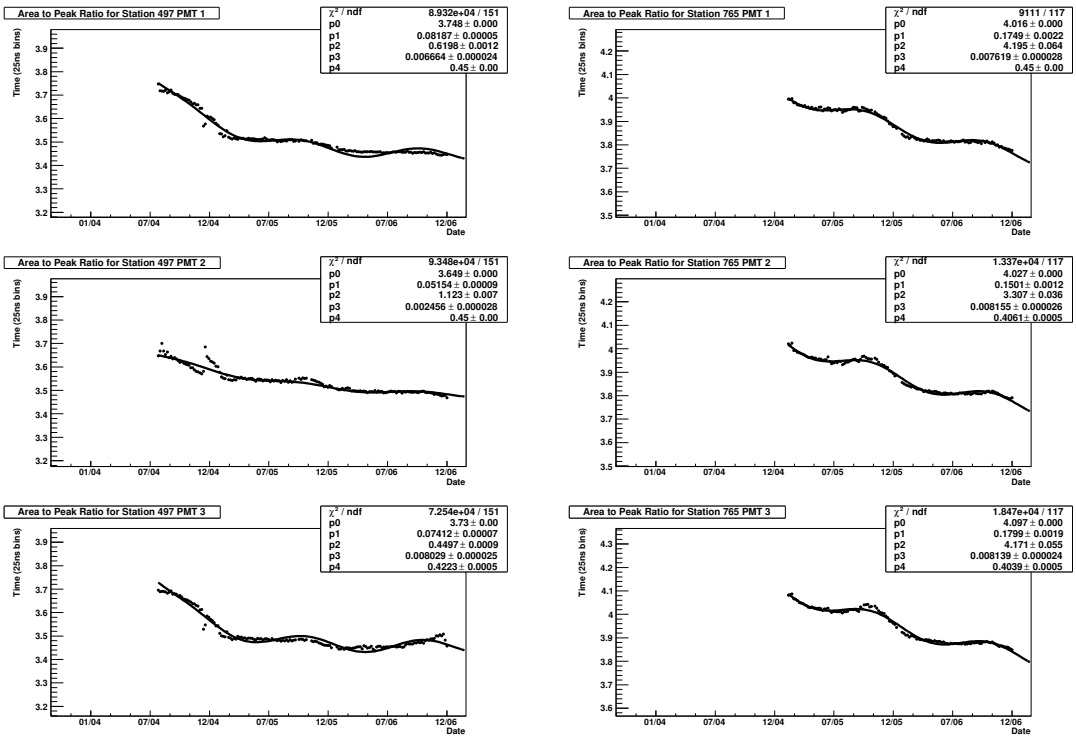

Figure 4.5: The fits to station 497 and station 765. The fits to the PMTs are best described by the exponential imposed on top of a sine function (equation 4.1).

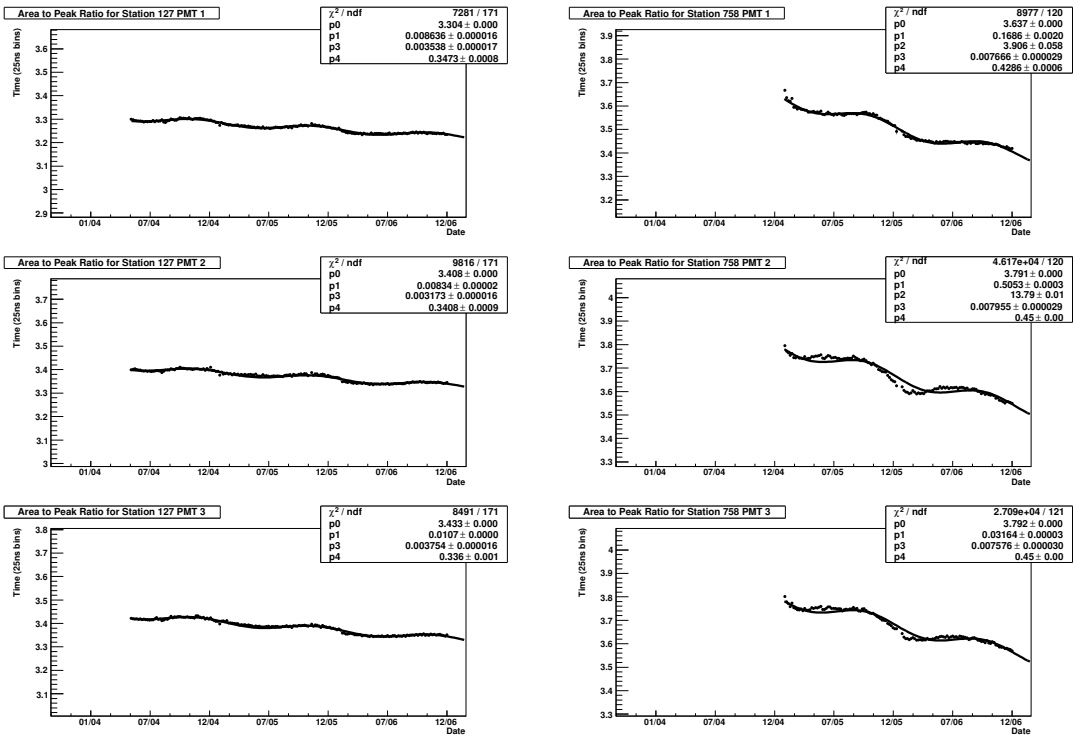

Figure 4.6: Several example fits to PMTs best described by the linear decrease on top of a sine function (equation 4.2).

peak ratio. Beginning with the time bin immediately after the first activation of the station a check is performed comparing the previous value of the area to peak ratio with the current value. Changes larger than 4% up or down are considered a discontinuity because the value is expected to be stable on a time period of five days. Visual analysis of the data suggested that an allowance had to be made for a short period of anomalous operation resulting in the choice to allow each phototube at most three discontinuities before it is rejected for instabilities. During the sweep periods without data are simply ignored, such that the last time bin with data is compared to the next time bin that contains data skipping the intervening dead period.

The second phase involves the identification of biasing effects not identified in the previous step. A loose cut of $\frac{\chi^2}{\mathrm{NDF}} < 3000$ is applied primarily to eliminate discontinuities that are *not* short, but pass phase one because they are akin to a step function; a single large discontinuity is less than the three allowed, and can result in a fit that does not contain reliable parameters. Fig. 4.7 is an example of phototubes with a step function separating two stable periods. The resulting fit is biased because the total period can not be described by a single function[3].

A final visual scan was used to further eliminate several fits that were not caught with the quantitative quality cuts. In this case the entire station was rejected, rather than rejecting the individual phototubes from that station. This resulted in the complete removal of six stations. Two of the visually removed stations can be seen in fig. 4.7.

Several stations eliminated in the visual scan contain at least one phototube that fails the quantitative quality cuts as well. In fig. 4.7 Station 300 phototube

[3]the phototubes shown in fig. 4.7 were not caught by the $\frac{\chi^2}{\mathrm{NDF}}$ cut because of a coincidence in the timing and size of the discontinuity, however the example is still valid

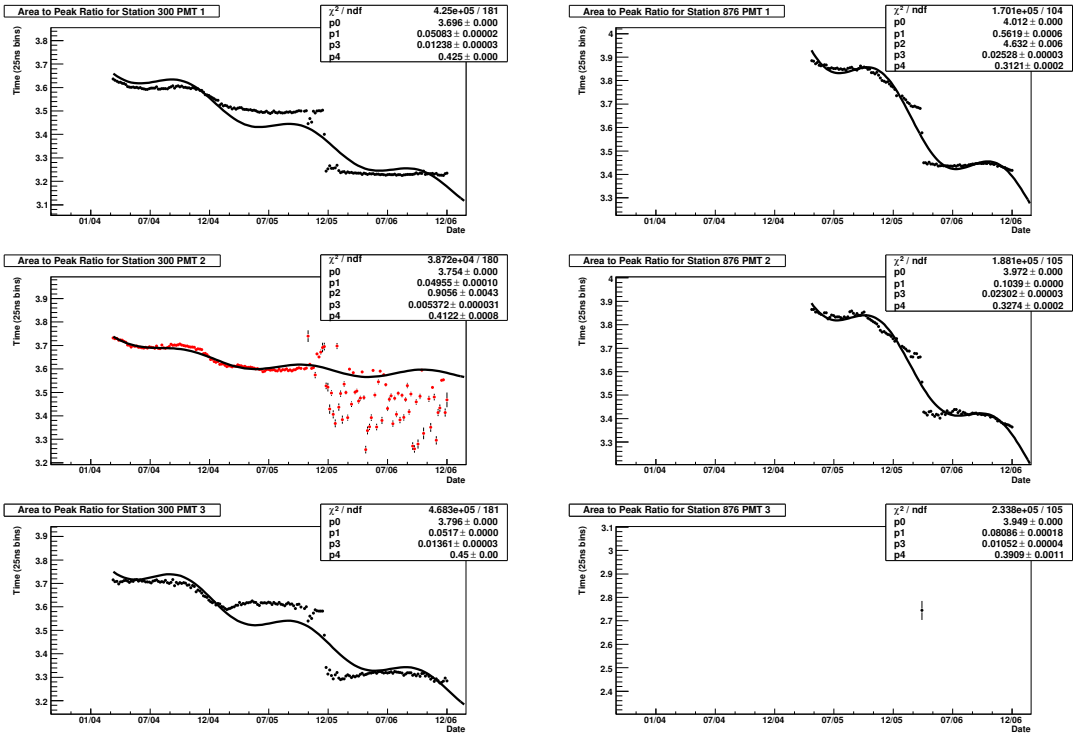

Figure 4.7: The fit with red markers is a PMT eliminated by quantitative quality cuts. Both of these stations, and four others like them, had to be eliminated by visual scan eliminating all the fits to any of the PMTs for these stations. **Left:** Station 300 had two PMTs (#1 and #3) that passed by accident. In these cases the single discontinuity covered enough time and was of the right size to allow an exponential fit to obtain an approximation that passed the loose cut on the reduced χ^2. **Right:** Station 876 came on-line late in the analysis period and a large linear fractional loss coupled with a sizable seasonal variation allows a function that obtains a good approximation despite the large discontinuity seen in the first half of 2006.

#2 was previously rejected by the quantitative cuts as indicated by the use of red markers for the area to peak ratio. The other fits use black data points and are the ones eliminated based on visual inspection.

4.4 Results

Of the 736 stations studied, 639 have at least one phototube that passes the criterion for inclusion in the final results yielding a data sample that covers $\simeq 87\%$ of the stations studied. The fit parameters are collected and analyzed for commonalities and/or correlations to identify long term trends the surface array is likely to exhibit.

4.4.1 Overall Normalization (p_0)

The overall normalization is not a quantity directly of interest in this work, however it is expected that the area to peak ratio for deployed stations is ~ 3.5 units [30]. The average value shown in fig. 4.8 is consistent with the expectation that the initial value collected during the fitting process is a bit higher than the array wide average which includes the decay observed in deployed stations.

4.4.2 Fractional Loss (p_1)

This is the measure most important to the long term stability of the Cherenkov light collection in the Pierre Auger surface detector. The array is expected to last twenty years and although the calibration system provides up to date values it is important to understand the changes the calibration system is compensating for.

There are two possible functional forms for the fitted behavior of each pho-

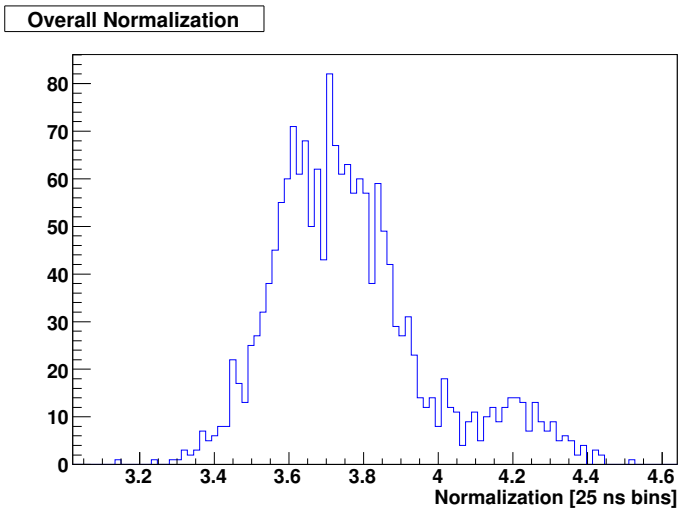

Figure 4.8: The overall normalization p_0 from the fits with an average value of 3.8 units (a unit is 25 ns bins). The bimodal distribution reflects that a portion of stations numbered higher than 570 tend to have a high initial value for the overall normalization.

tomultiplier tube, the exponential decay and the linear decay. Both functions contain a fractional loss term but the interpretations are slightly different. For the exponential the fractional loss is a limiting value that the station approaches asymptotically over time while for a linear function the fractional loss continues at the same magnitude every year. Fig. 4.9 is the distribution of fractional losses separated out by the type of function preferred. The linear phototubes always have a small fractional loss reflecting the small changes observed from year to year. For the exponential phototubes the largest fractional loss is unity suggesting that some stations will eventually become unuseable, however in these cases the final conclusion depends on the time scale over which the evolution is predicted to occur. Fig. 4.10 includes only the exponential phototubes, and relates the fractional loss to the characteristic time. Phototubes that decay quickly, a pe-

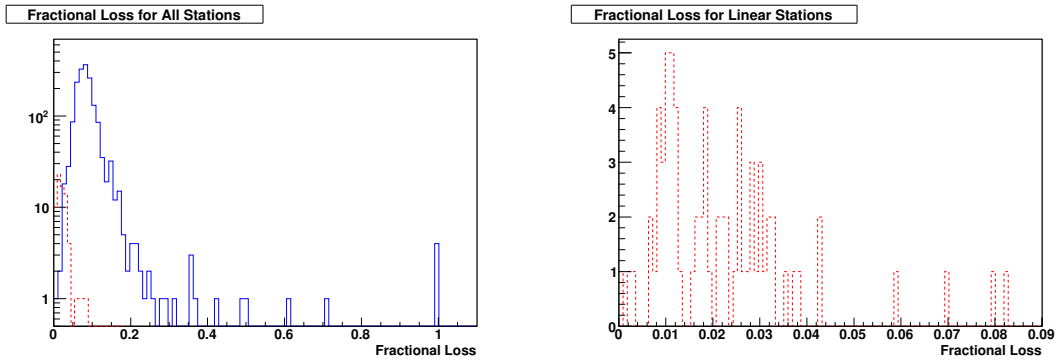

Figure 4.9: The fractional loss p_1 from the fits. **Left:** The fractional loss from exponential phototubes are shown in solid blue, while those from linear phototubes are shown in dashed red. **Right:** Taking just the linear phototubes the maximum fractional loss can be seen as less than 0.1.

riod of only a couple years, have a fractional loss of less than 0.2, with no obvious correlation between the parameters. However, as characteristic time increases, a strong positive correlation is noticeable. In this case the decay is slow, sometimes taking decades, but the final asymptotic value is smaller. This is reminiscent of the linear phototubes which decay slowly from year to year with a final limiting value of zero remaining signal. Therefore the long decay photo-multiplier tubes are the middle ground between a preferred linear fit and a preferred exponential fit. From fig. 4.10 it can be predicted that, with the exception of the three points clustered at a fractional loss of one and a characteristic time of eighteen years, none of the exponential phototubes will experience a signal loss greater than 0.5 during the planned twenty year operation of the array.

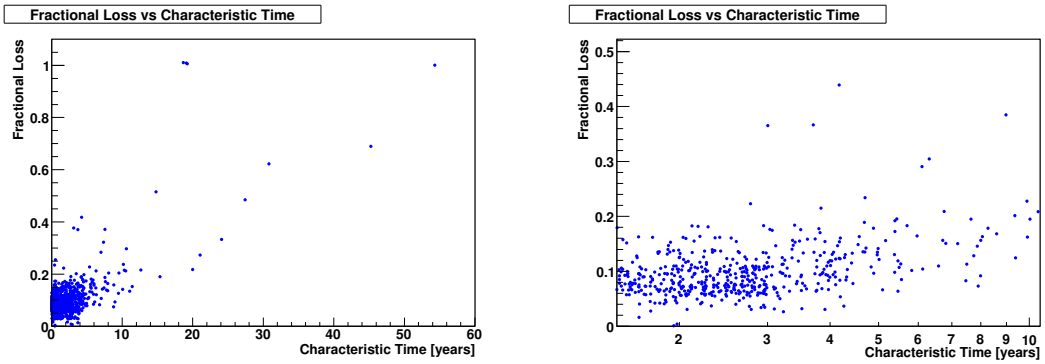

Figure 4.10: The fractional loss p_1 as a function of the characteristic time p_2 for exponential phototubes only. **Left:** Here the entire distribution is shown and the correlation between long characteristic time and large fractional loss' are clear. **Right:** Examining the phototubes with characteristic times less than ten years the maximum fractional loss' are much smaller and there is no apparent correlation between the measures.

4.4.3 Characteristic Time (p_2)

The characteristic time gives a measure of the time it takes exponential phototubes to stabilize. For many phototubes this period is short ($\sim$ 0.3 years) but it becomes increasingly long when the loss in signal is nearly zero or constant from year to year. The distribution of characteristic times can be seen in fig. 4.11 where the bulk of the phototubes settle on a time scale of less than two years. Combining the characteristic time and the fractional loss the area to peak ratio can be extrapolated into the future. Using ten years as a benchmark (half the planned life of the array), the remaining fraction of the original area to peak ratio is calculated. This provides useful insight into the evolution of the array. In fig. 4.12 the extrapolated remaining fraction of the area to peak ratio is shown for exponential phototubes as well as those that are changing linearly from year to

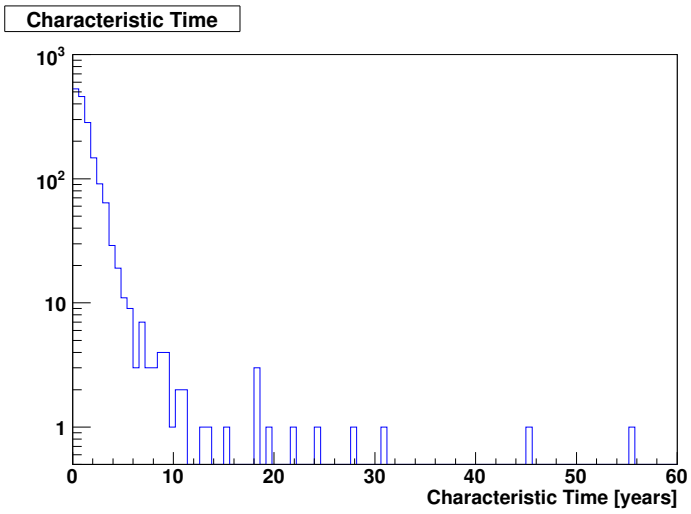

Figure 4.11: The characteristic time p_2 from the fits. Average value is 1.5 years.

year. After ten years the exponential phototubes have reached stability and are

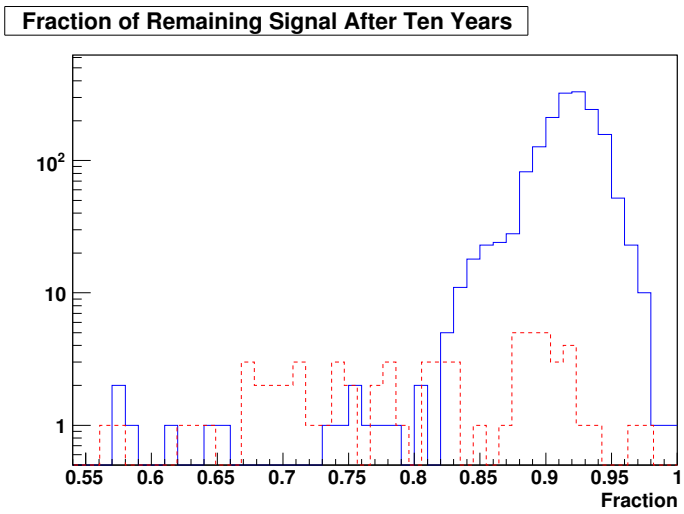

Figure 4.12: Combining the fraction loss p_1, the functional form, and the characteristic time p_2 when appropriate, an estimation of the remaining area to peak ratio after ten years of array operation can be obtained.

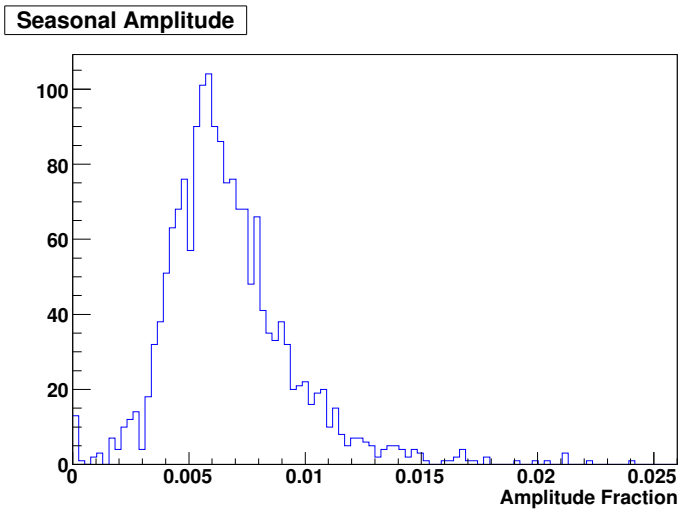

Figure 4.13: The seasonal amplitude p_3 from the fits. Average value is 6.8×10^{-3}.

not likely to appear any different in twenty years, however the linear phototubes occupy some of the smaller fractions and the extrapolations to longer time periods will increasingly separate them out. It may be necessary to replace the water or perform other maintenance on some of these stations within the operational life span of the array.

4.4.4 Seasonal Amplitude (p_3)

The seasonal amplitude p_3 is small. The changes in the area to peak ratio correlated to season are almost universally less than 0.1 (see fig. 4.13). The size of the amplitude also does not show any correlation to the characteristic time or the fractional loss (see fig. 4.14).

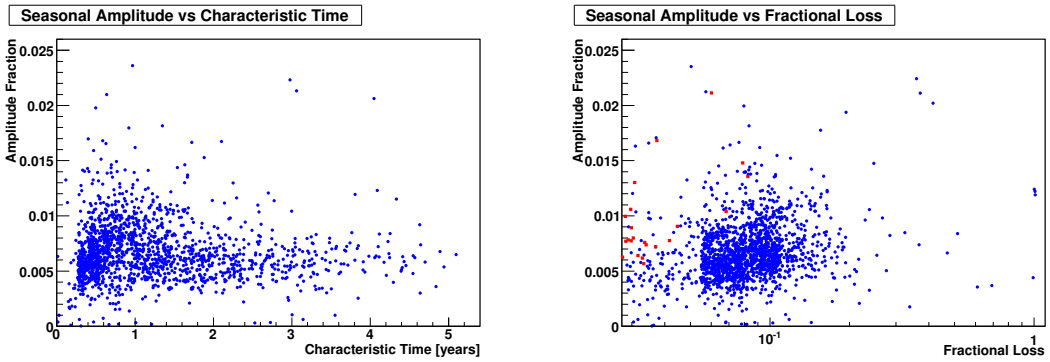

Figure 4.14: **Left:** Scatter plot of the seasonal amplitude and the characteristic time p_2. There is no apparent correlation. **Right:** Seasonal amplitude p_3 as a function of the fractional loss p_1 shown for exponential phototubes as blue circles and for linear phototubes as red squares. There is no apparent correlation.

4.5 Conclusion

The water stations of the Pierre Auger surface detector will function for the specified twenty year lifespan. We do not expect the changes in the absorption of Cherenkov photons by the water and/or the Tyvek® to pose a long term problem.

We have used the area to peak ratio as a measure of the water quality and Tyvek® reflectivity and discovered that water stations first lose signal and then generally stabilize. The signal loss begins after deployment and is fit well by an exponential with a characteristic time of less than a few of years. The total amount of the decrease is almost exclusively less than 20% of the area to peak ratio at the time of deployment. A loss of this magnitude will not adversely affect the operation of the surface detector and should be interpreted as a settling period. After this period, the water stations enter into a stable annual modulation coupled to the average annual temperature modulation. The amplitude of the modulation is less than 1% of the area to peak ratio at the time the water station

enters the period of stable oscillation. The oscillation is expected to continue into the foreseeable future.

A small number of photomultiplier tubes and the stations they are in seem to continue decaying beyond the settling period and may require maintenance at some point. The linear photomultiplier tubes constitute less than 5% of the total sample and those possibly requiring servicing are $\approx 1\%$ of the total.

We will continue to monitor the area to peak ratio for any further changes in the water quality and Tyvek® reflectivity, however aside from the annual modulation none are expected.

CHAPTER 5

Investigating the Composition of Cosmic Rays

Little is known about how cosmic rays with energies greater than 10^{18} eV come into being due in part to the extremely low event rate[1]. Proceeding with the simplest and most conventional scenarios ultra-high energy cosmic rays must be the result of some fantastically energetic phenomena occurring in other galaxies.

With literally billions of galaxies containing highly energetic astronomical phenomena that could fit the bill under unusual, though not impossible assumptions, candidates are easy to come by. One way to narrow the list is to check each potental source by making a map of the sky and attempt to match it against the map of detected cosmic rays. The method is fraught with dead-ends, false positives, incomplete catalouges, etc., but in the face of ignorance it is perhaps the best that can be done. Further complicating the task is evidence that most, if not all, ultra-high energy cosmic rays are nuclei meaning they are charged particles and therefore bend unpredictably in the random magnetic fields present in the void of space.

$$\theta \sim \text{charge} \cdot \text{length} \cdot \text{B}_{\text{field}}/\text{energy} \tag{5.1}$$

This is one way information on composition can help; heavier nuclei contain more protons and therefore bend more. Knowing this the additional deflection can be adjusted for in the search procedure. In addition the presence of elements

[1] one particle per square kilometer per century

heavier than hydrogen suggest that the acceleration process cannot occur in areas of high density because the nuclei would fragment upon collision. This also helps to narrow down the list of possible source objects.

5.1 Common Experimental Methods

Determining the composition of ultra-high energy cosmic rays grows from an understanding of the particle physics of the interactions involved. If primary cosmic rays interact via the strong force, as is the case for any hadron[2], then the cross section with air will be large and we can reasonably expect a shower that develops high in the atmosphere. And loosely speaking, the more hadrons involved, the higher the shower develops allowing us to separate light nuclei, with only a few hadrons, from those that are more massive. The other possibility, that cosmic rays do not interact via the strong force, limits us almost exclusively to photons or neutrinos. In these two cases the interaction is primarily electromagnetic for photons or weak for nuetrinos. Both of these forces have a "strength" that is less than that of the strong force and the showers begin much deeper in the atmosphere (or even within the Earth for neutrinos) leading to obvious phenomenological differences. The next sections describe common observable differences that stem from the particle physics of the first interaction.

Shower profiles

The longitudinal shower profile is a description of particle number as a function of material penetrated. It doesn't really matter if the shower is in air or lead so long

[2]mesons also interact strongly however none of them are stable and therefore unlikely to be candidates for cosmic rays

as we adjust for the difference in density. Observation of the profile yields one of the most effective techniques to discriminate composition. For ultra-high energy cosmic rays the initial interactions are highly inelastic[3] resulting in the creation of particles. The daughter particles, highly energetic themselves, participate in the same fashion leading to exponential growth in the particle number for the first several interaction lengths. When the average energy is no longer sufficient to produce additional particles, decay and absorption are the dominant processes and the particle count decreases nearly exponentially. The exact shape is given by the gaisser-hillas function 1.1 and the depth of maximum, referred to as X_{max}, is the compositionally sensitive parameter. The sensitivity derives from X_0, the depth of first interaction, which in turn derives from the cross section with air. Typical values of X_{max} are $\sim$700 g cm^{-2} for a hadronic primary cosmic ray of 10 EeV.

Particle counts & type

The charged particles within the aforementioned shower profile are almost entirely leptons, with only a small number of mesons and hadrons reaching the ground. Dominant among the leptons are the electrons and positrons which exceed by an order of magnitude the second most populous lepton, the muon[4]. The exact number of muons is set by the energy of the shower and the primary particle type. Muons are the result of pion decay and the pions themselves are created by strong force interactions. Photons and neutrinos do not interact via the strong force and therefore those showers lack a muon component. All hadronic showers contain some muons but the number of them is larger for showers that come from

[3]for 10 EeV cosmic rays $\sqrt{s} \sim$ 100TeV

[4]the productions of taus can be ignored unless the primary cosmic ray is a neutrino

heavier nuclei. Measuring the muon content of a shower is therefore sensitive to the composition of the primary particle.

Shower footprint

A further method for composition determination relies on the signals extensive air showers produce on the ground. By examining how the time structure varies across the shower footprint, some compositional sensitivity can be achieved bacause both the shower profile and the muon content effect particle distributions on the ground. A measurement of the time structure requires a detector equipped to collect the data needed and the method suffers a bit because ground based observables are typically heavily influenced by how much air a shower has penetrated. This leads to a strong zenith angle dependence because the amount of air between the first interaction and the detector on the ground is $\propto$ sec(zenith). The uncertainties in the time structure also make the definition of a reliable parameter difficult.

5.2 Short Review of Prior Results

Previous experiments have already exploited some of the techniques discussed to measure the composition of ultra-high energy cosmic rays. The results are consistent with primaries that are dominated by hadrons. I will take the next section to review some of these results.

AGASA

The AGASA (Akeno Giant Air Shower Array) experiment was a ground based detector in Japan [12] that used scintillator to count the number of charged

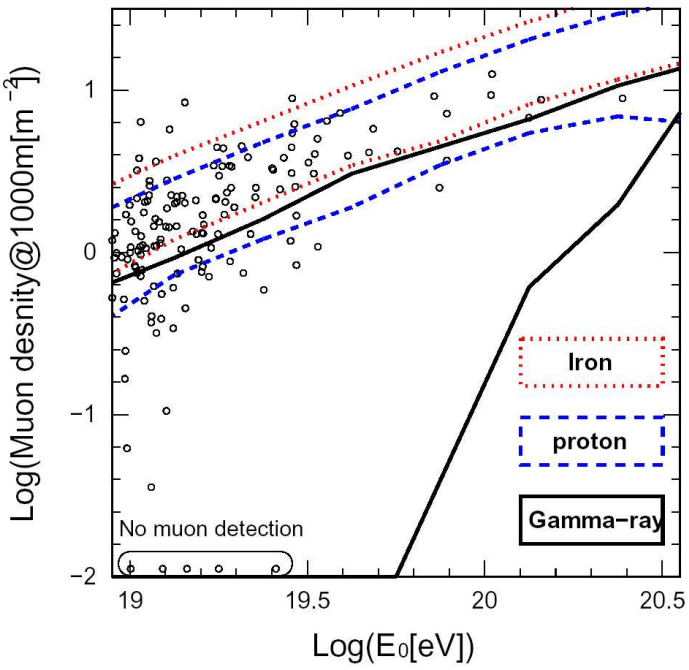

Figure 5.1: The number of muons measured by the AGASA experiment at a distance of 1000 meters from the shower core [32]. The circles are experimental data while the dashed blue, dotted red, and solid black lines represent proton, iron, and photon simulations respectively.

particles deposited. They exploited this feature to measure the muon content in a number of showers as seen in fig. 5.1.

HiRes

The HiRes (High Resolution Fly's Eye) experiment is a stereo fluorescence detector in Utah [13]. They used the observation of longitudinal shower profiles to estimate the depth of shower maximum, X_{max}, as a measure of composition. Not only can the absolute value of X_{max} be compared to expectations from simulations but also the evolution with energy, called the elongation rate. The elongation rate

from HiRes data is shown in fig. 5.2.

5.3 Prior Work With the Auger Detector

The hybrid nature of the Pierre Auger Observatory allows the application of several composition sensitive measures separately or in concert. Photon and neutrino showers are the easiest to distinguish from hadronic cosmic rays and searches in this domain have yielded the first results.

5.3.1 Hybrid photon limit

By observing shower profiles with the fluorescence detector a limit was deduced on the fraction of cosmic rays photons above 10^{19}eV. In this case it is expected that photons will produce showers with a deep X_{max}. For each observed cosmic ray event above 10^{19} eV simulations of photons are produced to create the expected distribution of X_{max} if the event was a photon. A cut is placed *a prior* near the edges of the X_{max} distribution and the measured X_{max} is compared for compatibility with a photon assumption. If the measured X_{max} is outside the acceptance region the event is rejected as a hadron; if it is within the acceptance region it is declared a photon. After adjusting for the efficiency of the cut a limit can be place on the fraction of photons PhotonFraction $= \frac{N_{photons}}{N_{non-photons}}$ with an energy greater than 10^{19} eV.

In ref. [33], a limit to the fraction of photons in the integral cosmic-ray flux of 16% (95% c.l.) above 10^{19}eV was obtained. The limit is based on 29 high-quality hybrid events registered in the period January 2004 - February 2006. The analysis has since been updated to include data collected until March 2007 yielding 55 events in total and a subsequent limit of 13% (95% c.l.) above 10^{19}eV.

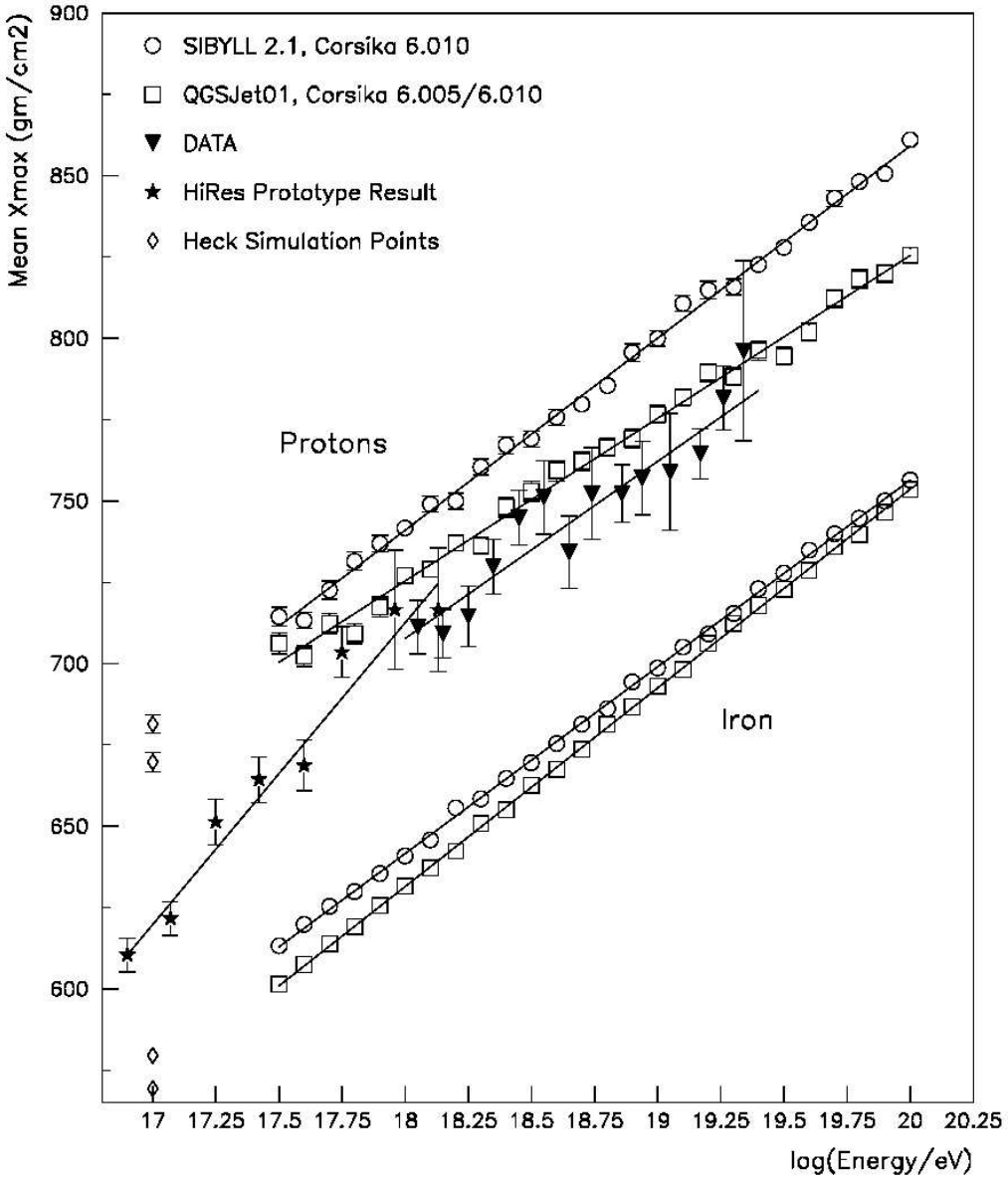

Figure 5.2: X_{max} from HiRes stereo data [1]. The data, shown as triangles, lie between the simulated expectations for protons and iron primary, shown as circles and squares. The data tend to favor a light to mixed composition.

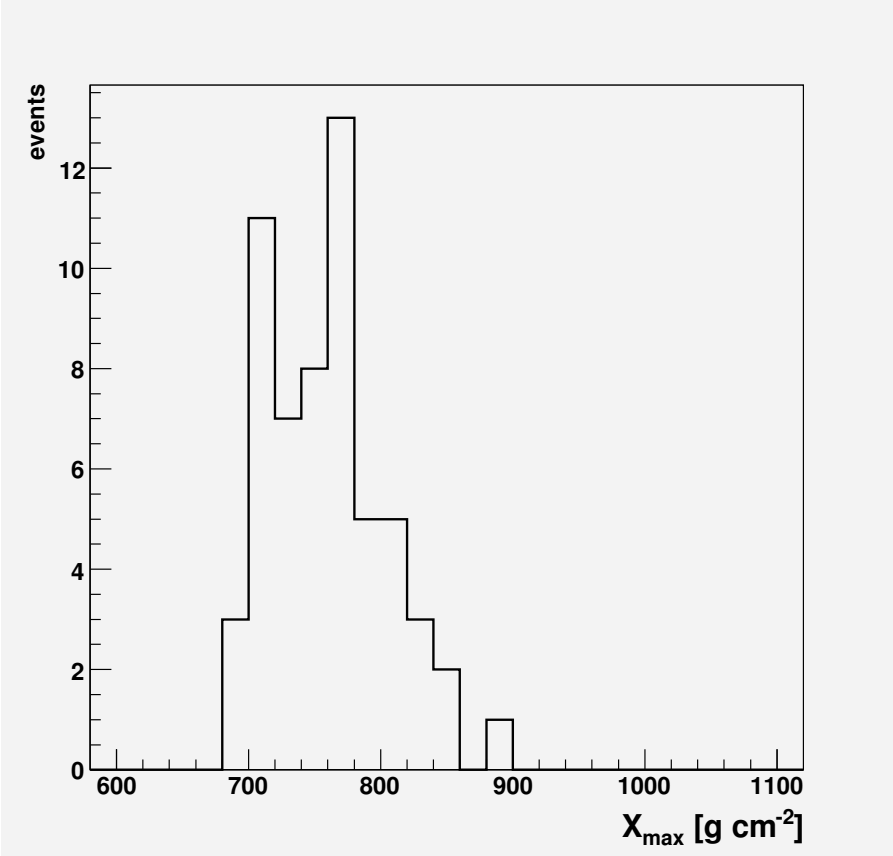

Figure 5.3: Observed $X_{\max}$ distribution with the Pierre Auger Observatory. Even the largest observed value of $X_{\max}$ ∼900 g cm^{-2} is well below the average value expected for photons (about ∼1000 g cm^{-2}, see e.g. Table 1 in ref [33]). The upper limit on the photon fraction is 13% (95% c.l.) above 10 EeV.

The measured $X_{\max}$ distribution is shown in fig. 5.3.

5.3.2 Neutrino limit

A neutrino limit has also been made possible by exploiting the shower footprint. Neutrinos are highly penetrating particles but nevertheless can result in showers observable by the array by looking for inclined showers that still contain a sig-

nificant electromagnetic component [34]. This signature is expected because any particle other than a neutrino (or photon) interacts at the top of the atmosphere and therefore the longitudinal profile is attenuated approximately proportional to the secant of the zenith angle. Electromagnetic particles have a tell-tale broad time structure in the digitization hardware and horizontal showers that display this characteristic for the bulk of the stations in an event are possible neutrinos. The absence of such showers allows a limit on the flux to be placed as shown in fig. 5.4.

5.3.3 Risetime & curvature analysis

The analysis presented in this section is particularly important because it formed the basis for this thesis.

One way to examine composition with the surface detector is to choose observables that are sensitive to the differences expected from various cosmic ray primaries. In this case the chosen measures are the risetime of the signal at 1000 meters from the core and the curvature of the shower front. Both are related to the shower maximum, and to a lesser degree, the muon content.

5.3.3.1 The Risetime

The arrival time distribution of particles in a shower is related to X_{max} due to the geometry of the situation. Most particle creation occurs before the shower reaches its maximum and for showers that develop early the difference in path lengths between produced particles is small. However, for showers which have a deeper X_{max} the particles are created along a much longer line increasing the spread of the time signals.

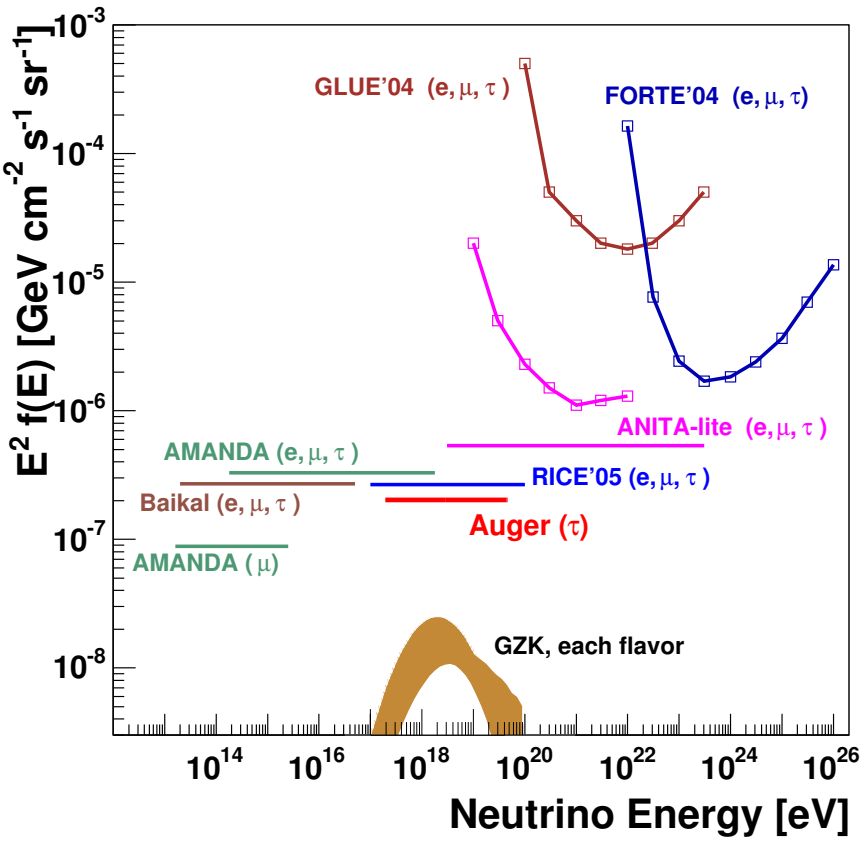

Figure 5.4: The Pierre Auger Observatory upper limit on the neutrino flux compared with other experiments in the same energy range [34]. The flux is calculated using only the interaction and decay modes for tau neutrinos. The inclusion of other neutrino flavors is still a work in progress [35].

It is also believed the risetime is related to the muon content of the shower in that muons essentially travel in straight lines once they are created while electromagnetic particles scatter multiple times. The result is that the paths for muons really are straight from the point of creation strengthening the argument about the difference in path lengths.

The overall result is that deep penetrating primaries (like protons) will have a longer risetime than shallow primaries (like iron), see fig. 5.5 and fig. 5.6. These two relationships (the muon content and depth of shower penetration) combine to give the risetime a strong distinguishing power between light and heavy primaries. The method used to measure the risetime can be found in chapter 7, in the section on the FADCPulseParametersUCLA module. Please also see the appendicies.

5.3.3.2 The curvature

The curvature is sensitive to the muon content and X_{max} of a shower through the effect on the shape of the shower front which is calculated based on the relative arrival times for the first particle at various distances from the shower core. All shower particles have a velocity of c (the speed of light) however muons travel in straight lines once created and therefore arrive first and with a narrower time spread compared to the electromagnetic component. A shower with a greater number of muons deposits these prompt signals, regardless of the distance to the shower core, in a greater number of stations resulting in a shower front that is flatter than muon poor showers. X_{max}, and by correlation X_0 influences the lateral spread of signals on the ground. An efficient model assumes a hemispherical shower front expanding from the point of first interaction (discussed in chapter 7). For showers that interact early the front of particles form an arc with a large

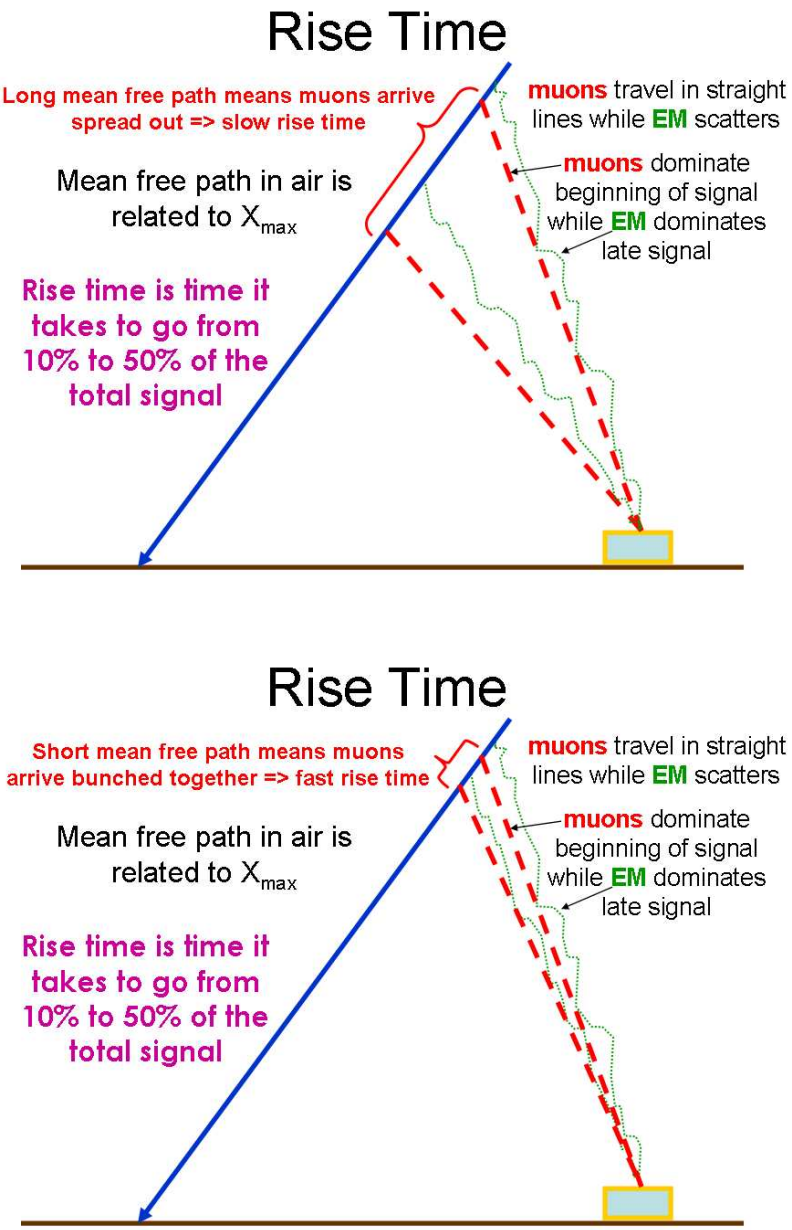

Figure 5.5: Description of how risetime relates to composition. Courtesy of D. Barnhill.

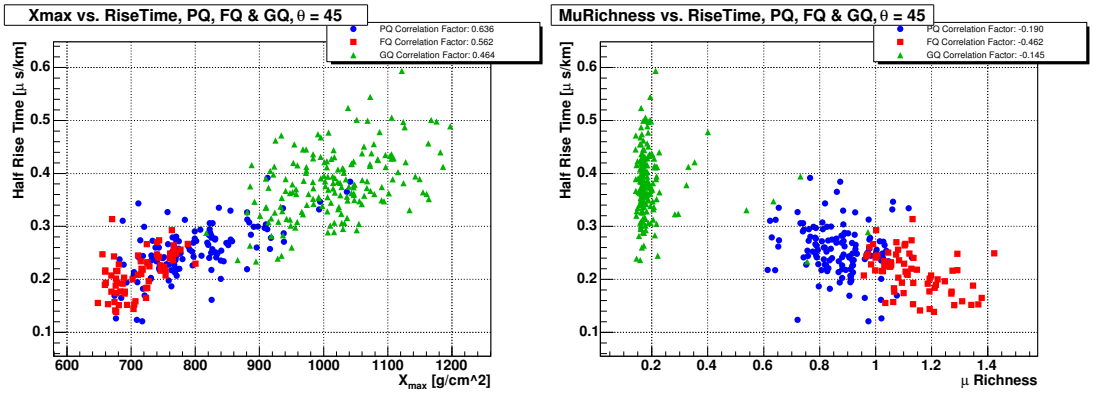

Figure 5.6: Monte-carlo X_{max} (left) and muon richness μ (right) versus risetime at 45 degree zenith angle. Iron (red squares), proton (blue circles), and photon (green triangles). μ is defined as $100 \cdot N_{\mu,max}/N_{\max}$.

radius of curvature whereas the opposite is true for showers that penetrate deeply. The result is that deep penetrating primaries (like protons) will have a smaller radius of curvature than shallow primaries (like iron), see fig. 5.7 and fig. 5.8. The curvature refered to in the figures is the geometrical *radius of curvature* with units of kilometers.

5.3.3.3 Parameterization

To be able to compare the real data to monte-carlo predictions using the risetime or curvature as described above, the monte-carlo predictions must be parameterized. It is not computationally feasible to simulate all possible angles and energies with the monte-carlo showers, thus the monte-carlo simulations are done at fixed angles and energies and a parameterization is made from this data to interpolate the values of the observables at any energy and angle.

The exact method followed is outlined in [4], but it is sufficient to state that the parameterization is done as a function of S(1000) and zenith angle, which

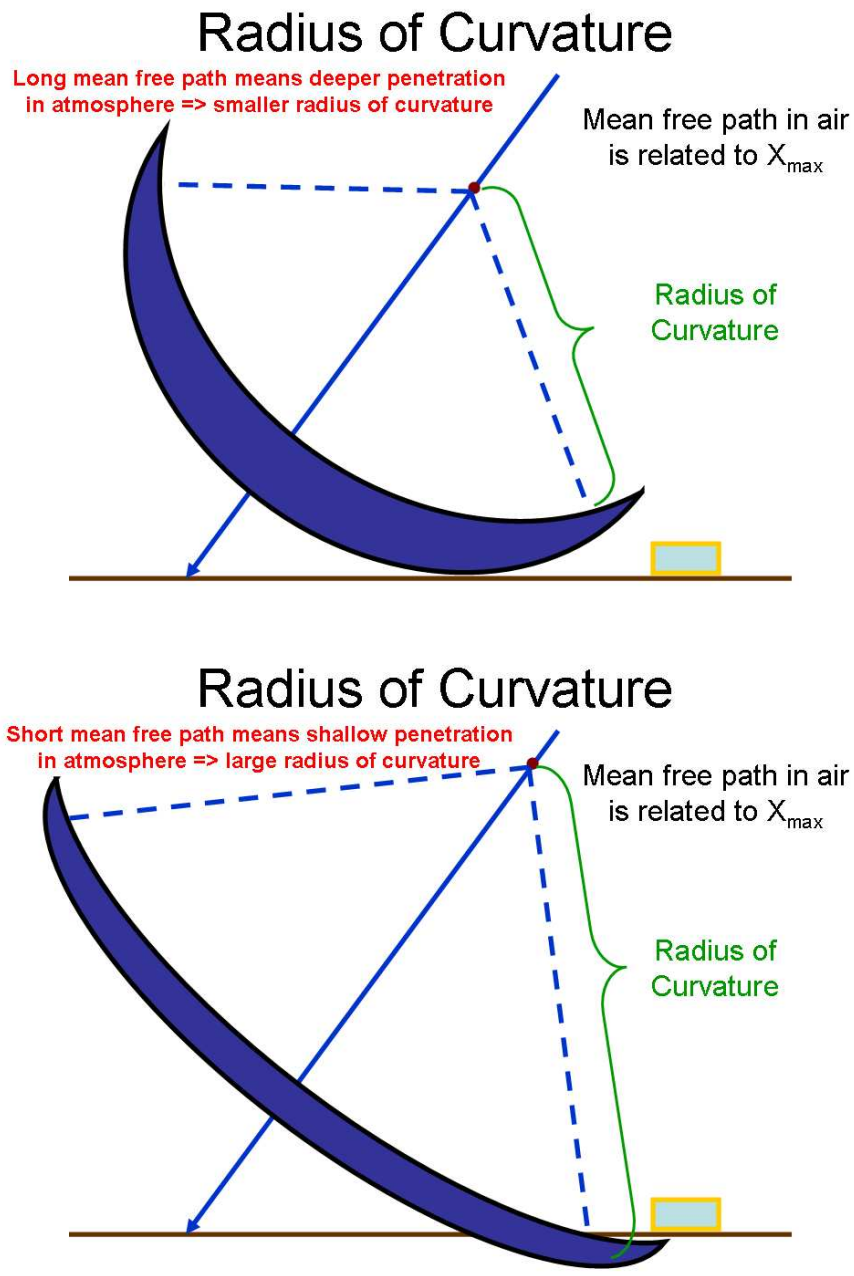

Figure 5.7: Description of how curvature relates to composition.

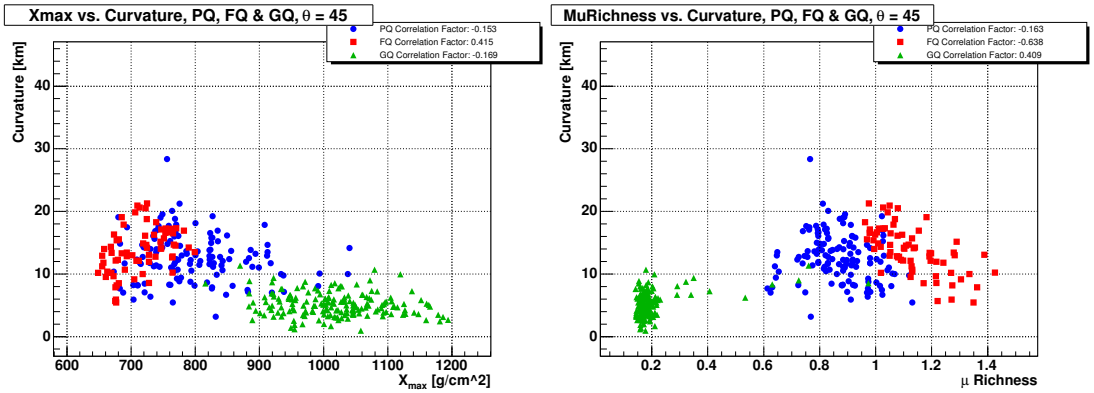

Figure 5.8: Monte-carlo $X_{\max}$ (left) and muon richness μ_{richness} (right) versus radius of curvature at 45 degree zenith angle. Iron (red squares), proton (blue circles), and photon (green triangles). μ_{richness} is defined as $100 \cdot N_{\mu,max}/N_{\max}$.

avoids the problem of energy determination before making the comparison to monte-carlo showers. Only after the comparisons are made with the monte-carlo predictions are energies assigned to the real showers, and that is only done to illustrate the trends with increasing energy and to assign a reasonable energy to the shower.

The showers used in the parameterization are simulated at fixed energies and fixed zenith angles. The energies used are 10, 31, and 100 EeV while the zenith angles are 0, 25, 36, 45, 53, and 60 degrees. The parameterization makes it possible to interpolate the predicted value of the parameter for any primary energy (really S(1000)) and zenith combination.

The difficulty in studying trends with energy for the surface detector observables compared to $X_{\max}$ studies, is that there is a strong zenith angle dependence, see fig. 5.9 and fig. 5.10. To plot the trend of the real data as a function of energy, this zenith angle dependence must be taken into account. The method is similar to the energy determination method presented at the 2005 International Cosmic

Ray Conference [36] (also see chapter 6), in that the values of the real data are projected onto what the values would be at 38°. More explicitly, for each shower the risetime and curvature is compared to a monte-carlo predicted value with the same S(1000) and zenith angle. The deviation from the monte-carlo prediction is defined in units of monte-carlo predicted standard deviation. The adjusted value at 38° is then calculated by taking the monte-carlo predicted mean value at 38° and adding the product of the number of standard deviations with the value of the monte-carlo predicted standard deviation at 38°:

$$\tau_{38} = \tau^{MC}(S_{38}(1000), 38) + \frac{\tau^{real} - \tau^{MC}(S(1000), \theta)}{\sigma_{\tau}^{MC}(S(1000), \theta)} \sigma_{\tau}^{MC}(S_{38}(1000), 38) \quad (5.2)$$

In the previous equation, τ_{38} is the angle-adjusted parameter, τ^{real} is the measured parameter of the event (along with the reconstructed S(1000) and zenith angle θ), and $S_{38}(1000)$ is the angle-adjusted value of S(1000) according to an energy converter such as the constant intensity cut based energy converter [36]. This is best illustrated with a simple example, in this case using the risetime. Shower X has an S(1000) of 50 VEM, a zenith angle of 50°, and a risetime of 200 ns. This is compared to a monte-carlo prediction (iron+qgsjet01c for example) for the same S(1000) and zenith angle. This monte-carlo model may predict a risetime of 160 ns and the predicted standard deviation is 20 ns (at 50 VEM and 50°). The corrected value of the risetime of shower X at 38° depends on the predicted value of 68 VEM at 38°. The 68 VEM value for the corrected S(1000) comes from the energy correction using the CIC energy converter. With this angle-corrected S(1000) as the input, the monte-carlo predicts an average risetime of 250 ns and a standard deviation of 15 ns. The final angle and S(1000) corrected value of the risetime for shower X would be 280 ns.

$$280 = 250 + \frac{200 - 160}{20} \cdot 15$$

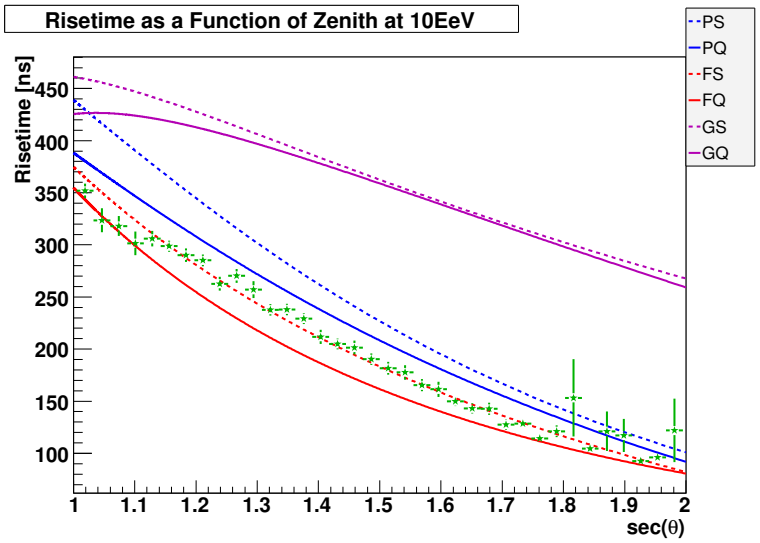

Figure 5.9: The risetime has a strong zenith angle dependence for fixed energies. These are monte-carlo predictions (lines) for the risetime at a fixed energy (according to the CIC+SD approach, [37]) plotted with real data (green markers). Blue = proton, red = iron, solid = qgsjet01c, dashed = sibyll2.1

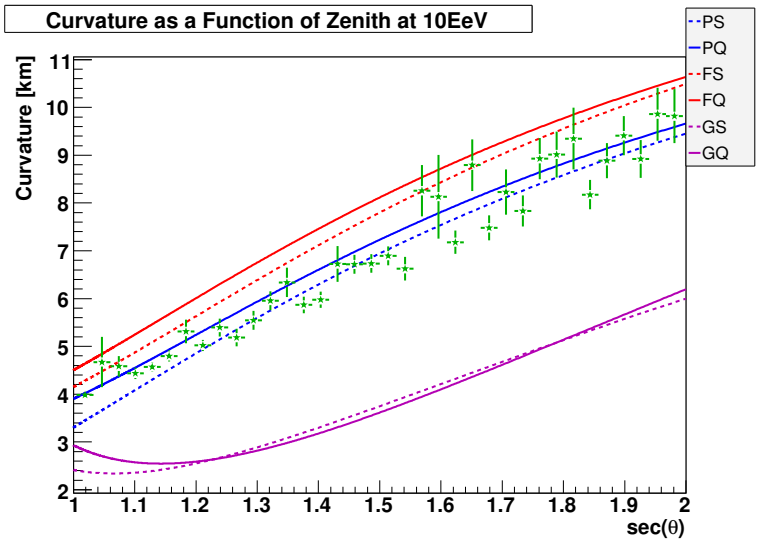

Figure 5.10: The curvature has a strong zenith angle dependence for fixed energies. These are monte-carlo predictions (lines) for the curvature at a fixed energy (according to the CIC+SD approach, [37]) plotted with real data (green markers). Blue = proton, red = iron, solid = qgsjet01c, dashed = sibyll2.1

5.3.3.4 Results

The data used in this analysis is from the period of January 1, 2004 to October 8, 2006. The zenith angle is required to be between 0 and 60 degrees and the hexagonal T5 was used in the data selection. The reconstruction was performed using the offline reconstruction [38], with a fixed slope in the Lateral Distribution Function (LDF). The curvature used is provided by the same reconstruction by fitting a hemisphere to the trigger times of the surface detector stations. The start times used in the fitting were corrected using a cleaning procedure developed to remove single muons that are unrelated to the event [39]. The risetime data was fit using a quadratic function fixed to 40 ns at the shower core, i.e. $40+ar+br^2$ [40]. The risetime in a tank is defined as the time it takes the signal to increase from 10% to 50% of the total signal and includes an asymmetry correction [41].

$$\begin{gathered} t_{\frac{1}{2}\text{corrected}} = t_{\frac{1}{2}} - g \cdot \cos\zeta \\ \textit{with} \\ g = \alpha + \gamma \cdot r^2 \\ \alpha = -66.61 + 95.13 \cdot \sec\theta - 30.73 \cdot \sec^2\theta \\ \gamma = -0.0009721 + 0.001993 \cdot \sec\theta - \\ 0.001259 \cdot \sec^2\theta + 0.0002546 \cdot \sec^3\theta \end{gathered} \tag{5.3}$$

Only non-saturated tanks with a signal larger than 10 VEM were used in the fits and the stations are weighted according to the following formula.

$$\begin{gathered} \sigma_{t_{\frac{1}{2}}} = \frac{j}{\mathrm{S}} + k \\ \textit{with} \\ j = 80.0 + (5.071 \times 10^{-7} + 6.48 \times 10^{-4} \cdot \sec\theta - \\ 3.051 \times 10^{-4} \cdot \sec^2\theta) \cdot r^2 \\ k = -16.46 \cdot \sec\theta + 36.16 \end{gathered} \tag{5.4}$$

In addition, quality cuts were made requiring 5 or more stations to be used in the LDF fit, and that the reconstruction stage be greater than or equal to 4 (specific to the offline reconstruction).

After performing the transformation of the risetime and curvature to the value at 38°, it is easy to plot the trend with energy. The energy is assigned according to the CIC+SD method [37], but since the comparisons of real data with monte-carlo predictions are made using S(1000), the results could be translated in energy according to the difference between CIC+FD [36] and CIC+SD. In fact, the correction of the S(1000) value to the $S_{38}(1000)$ value is not very important in that the result of the average behavior is stable with less than a 5% energy-independent change.

In fig. 5.11 and fig. 5.12, the result is shown for the transformation of the risetime and curvature respectively. The lines are the monte-carlo predictions, with the red lines being iron simulations and the blue lines are protons, while solid lines are simulations done with qgsjet01c [42] and the dashed lines are using sibyll2.1 [43] (Aires [44] was used for all the simulations). Also included in the plot is a fit to the data, shown as a dashed black line. The slope of the fitted line for risetime is -0.57 ± 4.4 with a χ^2/ndf of 8.6/8 and for curvature the slope is 1.4 ± 0.13 with a χ^2/ndf of 6.4/8.

When doing this transformation, a certain monte-carlo model is used as the basis of the transformation. For the above plots, the iron+qgsjet combination is used. It is interesting to see that the result is nearly independent of the choice of this model, even though the behavior is quite different with zenith and energy [45]. This is to be expected though, as long as the parameterization is sound, because the transformations are smooth with angle and are not drastically different in shape.

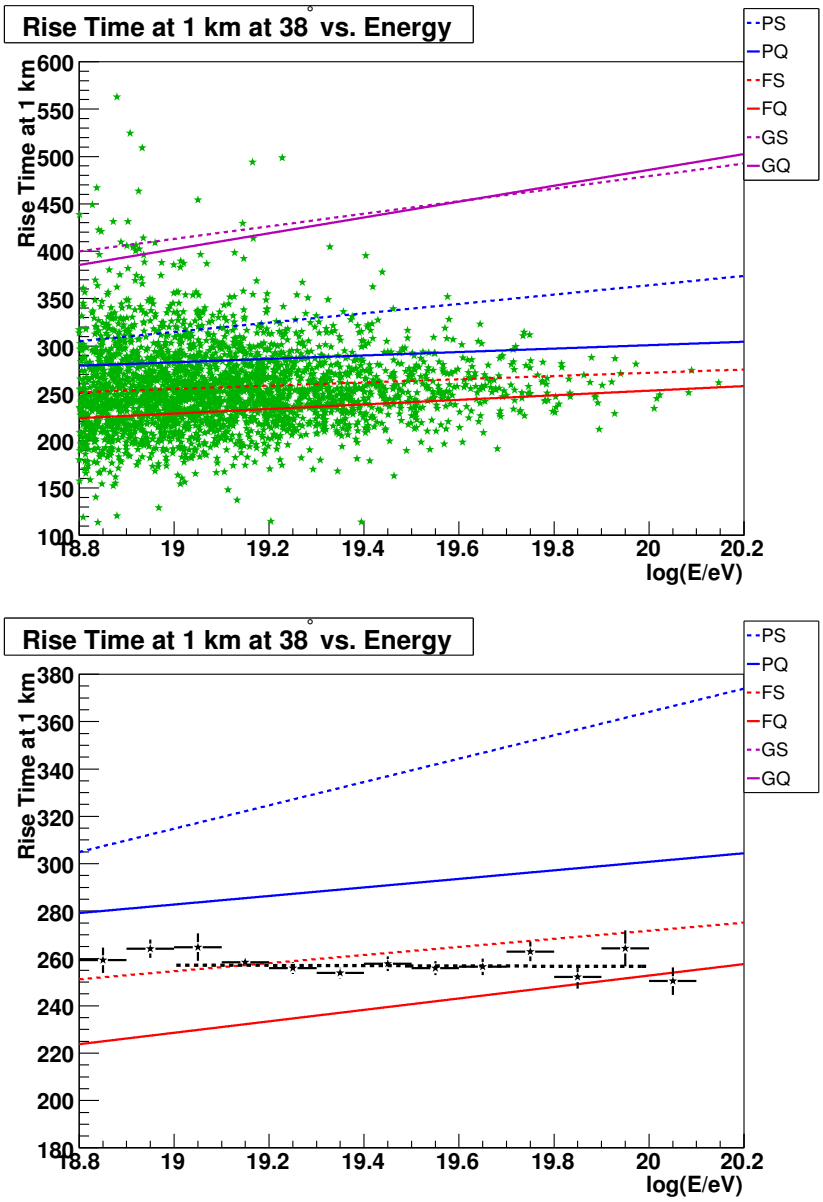

Figure 5.11: A plot of monte-carlo predictions (lines) for the risetime as a function of energy at a fixed angle (38°). Data (scatter plot with green markers on top and binned plot with black markers on bottom) is plotted on top of the monte-carlo predictions to show energy trends. Blue = proton, red = iron, solid = qgsjet01, dashed = sibyll2.1. A dashed black line is the result of a line fit to the data.

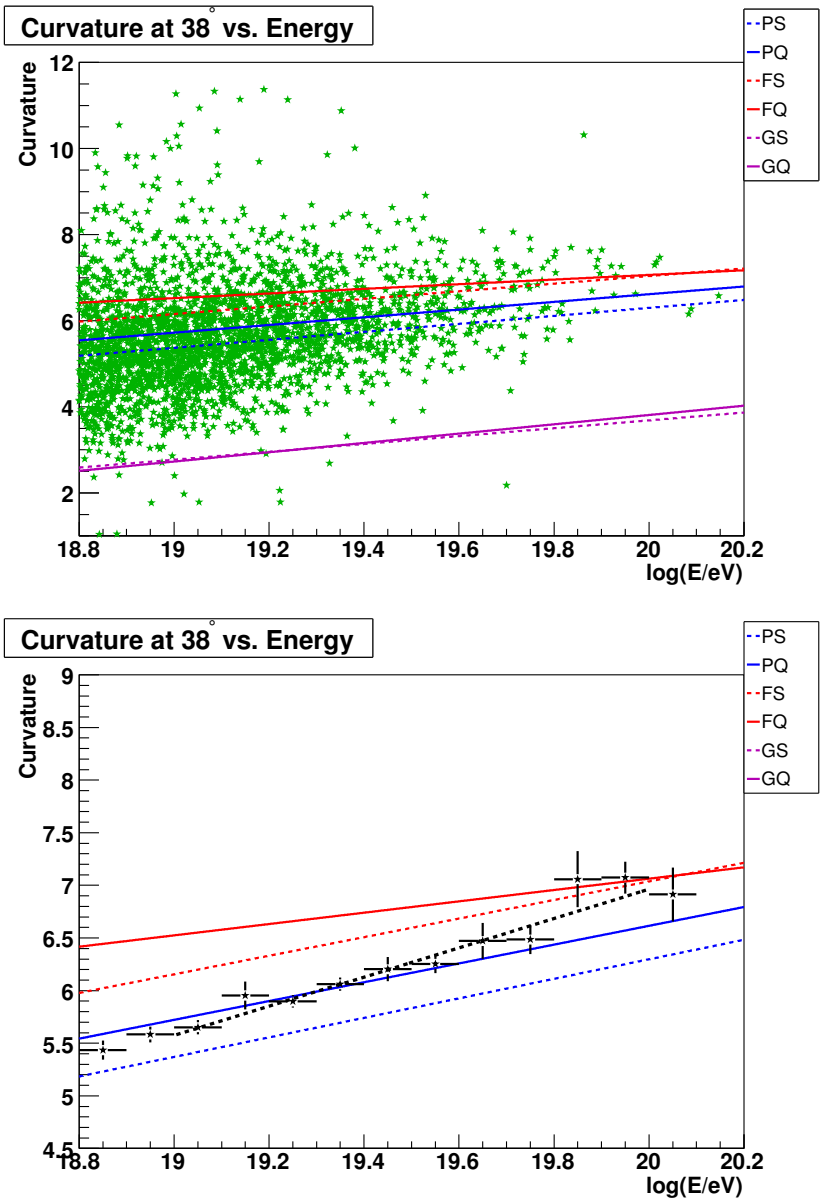

Figure 5.12: A plot of monte-carlo predictions (lines) for the curvature as a function of energy at a fixed angle (38°). Data (scatter plot with green markers on top and binned plot with black markers on bottom) is plotted on top of the monte-carlo predictions to show energy trends. Blue = proton, red = iron, solid = qgsjet01, dashed = sibyll2.1. A dashed black line is the result of a line fit to the data.

It is also possible to check that the spread of the distributions is similar to what is predicted from the monte-carlo showers. This is done by calculating the standard deviation of the real data in each bin of $S_{38}(1000)$ and comparing it to the parameterized monte-carlo predicted standard deviation in that same bin and to plot the result as a function of energy. This plot is shown in fig. 5.13 and fig. 5.14. The method used in this analysis corrects for the angular dependence, it must be checked that there is no systematic effect with angle. This was shown for the risetime in [45].

5.3.4 Fluorescence detector elongation rate

The most recent result for the Pierre Auger Observatory on the composition front was presented at the 30$^{\text{th}}$ ICRC in July of 2007. It used the fluorescence detector of the Pierre Auger Observatory to directly measure the X_{max} of cosmic ray showers with a resolution of 20 g cm^{-2} [46]. Because of the accuracy of the measurement, the X_{max}'s from hybrid events are the standard against which all purely surface detector methods are compared. Using events collected between the 1$^{\text{st}}$ of December 2004 and the 30$^{\text{th}}$ of April 2007 the average value of X_{max} as a function of energy has been determined [47] and is shown in fig. 5.15. The mean value of X_{max} can be compared directly to the expectation from shower simulations to gauge the mixture between heavy and light elements at a given energy. The conclusions of these comparisons however depend on the shower simulation assumed. A rather model independent way to extract information on the composition is to compare the slope of a line fit to the average X_{max} as a function of energy as seen in fig. 5.15. **All** models predict a linear increase if the composition is constant, therefore a slope that is not uniform indicates a composition that is similarly non-uniform.

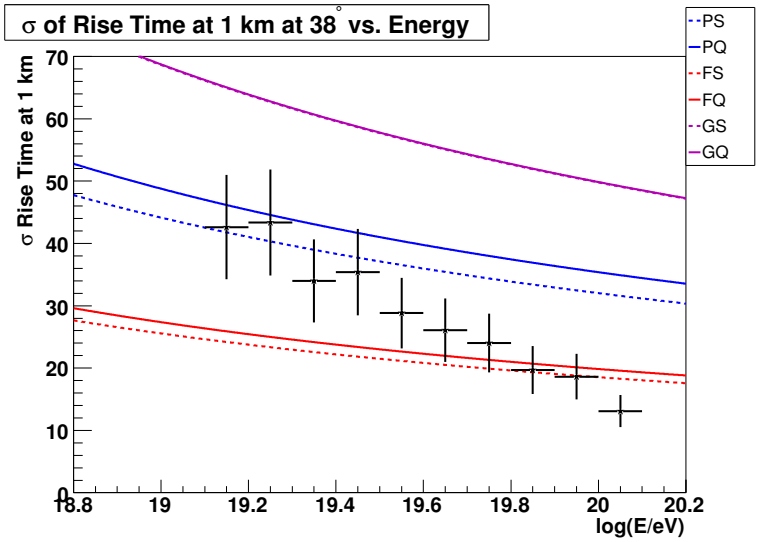

Figure 5.13: A plot of monte-carlo predictions (lines) for the RMS of the risetime as a function of energy at a fixed angle (38°). Data (black markers) is plotted on top of the monte-carlo predictions.

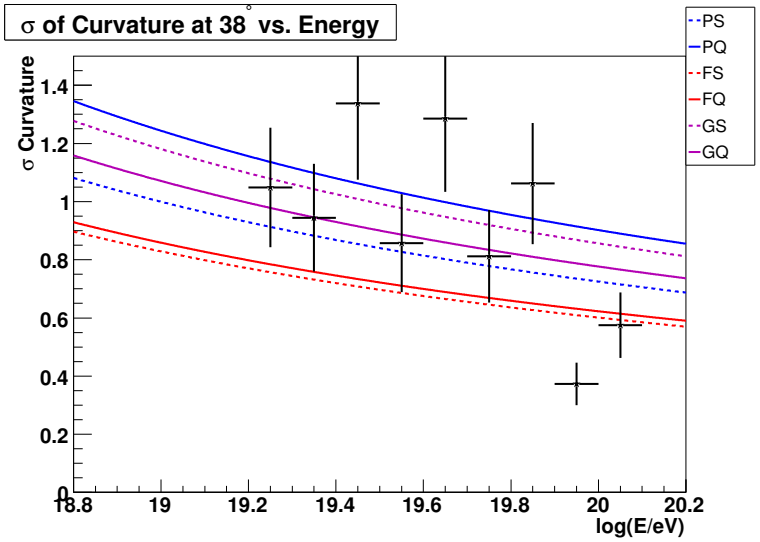

Figure 5.14: A plot of monte-carlo predictions (lines) for the RMS of the curvature as a function of energy at a fixed angle (38°). Data (black markers) is plotted on top of the monte-carlo predictions.

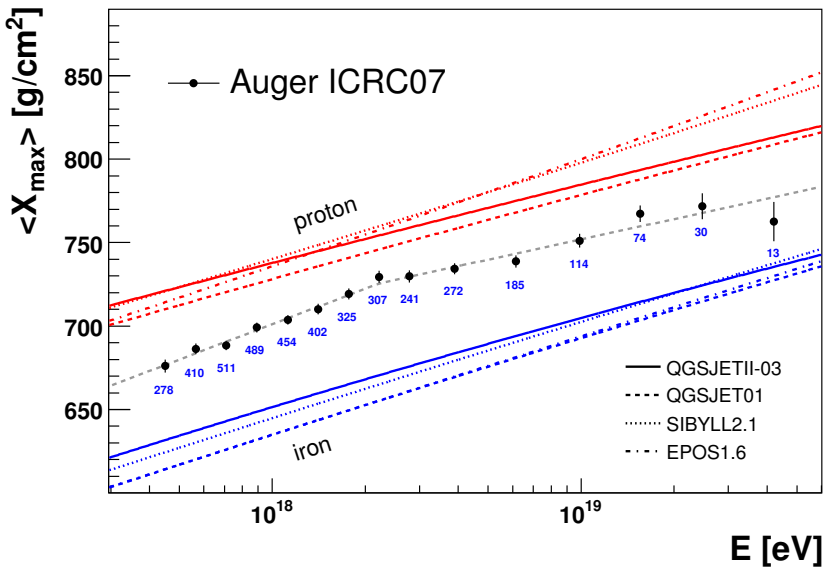

Figure 5.15: The average X_{max} of hybrid showers from the Pierre Auger Observatory. The dashed grey line is a fit to the data containing a single break-point and the commonly referred to "elongation rate" is the slope of those lines. The probability of the broken line fit is 63% while a line without a break in the slope has a less than 3% chance of describing the data [47]. A change in the elongation rate is indicative of a change in composition.

CHAPTER 6

Atmospheric Development, S(1000), and Energy Determination

A hybrid detector like the Pierre Auger Observatory has the ability to measure the longitudinal development with a fluorescence detector as well as the lateral distribution with a surface detector providing the entire three dimensional structure of the air shower (see fig. 6.1). However, this is not the only way to accomplish a three dimensional reconstruction of shower development. It is possible to obtain the same three dimensional information using the surface detector alone; a tremendous advantage because the surface detector observes approximately ten times as many events at higher energies due to its much longer duty cycle.

This chapter is a study I did to compare the three dimensional shape of cosmic ray air showers in both real data and simulations. The purpose was to gain some insight into how the two compared and to speculate on the possible reasons for any differences.

6.1 Atmospheric attenuation

The particle densities vary primarily as a function of the shower zenith because the average grammage of atmosphere that must be penetrated, and hence the atmospheric attenuation, increases as the secant of the zenith angle (see fig. 6.2).

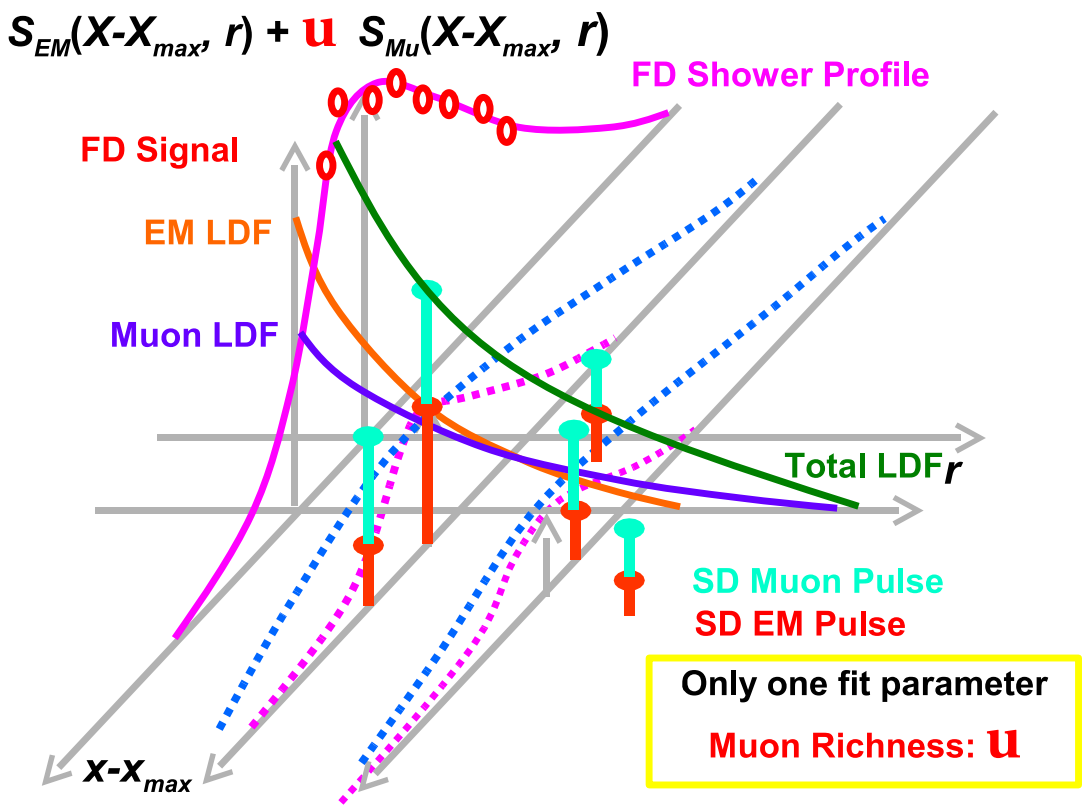

Figure 6.1: Schematic development of a cosmic ray shower. At a radius (r) of zero the core of the shower shown as the pink line is observed by the fluoresence detector while the lateral spread is a property measured by the surface detector. As the zenith angle increases the shower maximum is further from the surface detector (in the figure the maximum of the pink line shifts backward) and the signals deposited in the stations are smaller.

A third degree polynomial in the sine of the zenith angle squared well represents this effect and provides a smooth continuous interpolation over the range of zenith angles. A simple linear interpolation suffices to model the particle densities between selected radial distances. These two models form the basis of the mapping that we are going to create where the secant of the zenith angle and the radial attenuation form the orthogonal axes, longitudinal development and lateral development, respectively (see fig. 6.1).

Applying this method to simulated particle densities reveals that X_{max} and muon richness can both be inferred from the shape of the mapping and then compared directly to real data using the constant intensity cut method [48]. The comparison of a monte-carlo mapping to what is observed in real data is a hypothesis test of the assumptions on composition and model used as inputs for the monte-carlo mapping.

6.1.1 Constant intensity

Obtaining the particle densities from real data using the constant intensity cut method involves an assumption. The assumption in this case is that cosmic rays arrive uniformly from all zenith angles on large scales (large scales being on the same order as the angular binning used to determine the constant intensity cut curve). This assumption is supported by angular analyses to date [49, 17]. Since the Pierre Auger surface detector is essentially a plane on the ground whose cross-sectional area varies with shower zenith angle the flux is not constant as a function of the zenith angle; rather we find that for a uniform isotropic sky we should expect the number of events to be constant in the sine of the zenith angle squared [50].

To obtain a parameterization of S(1000), or any other distance, in the con-

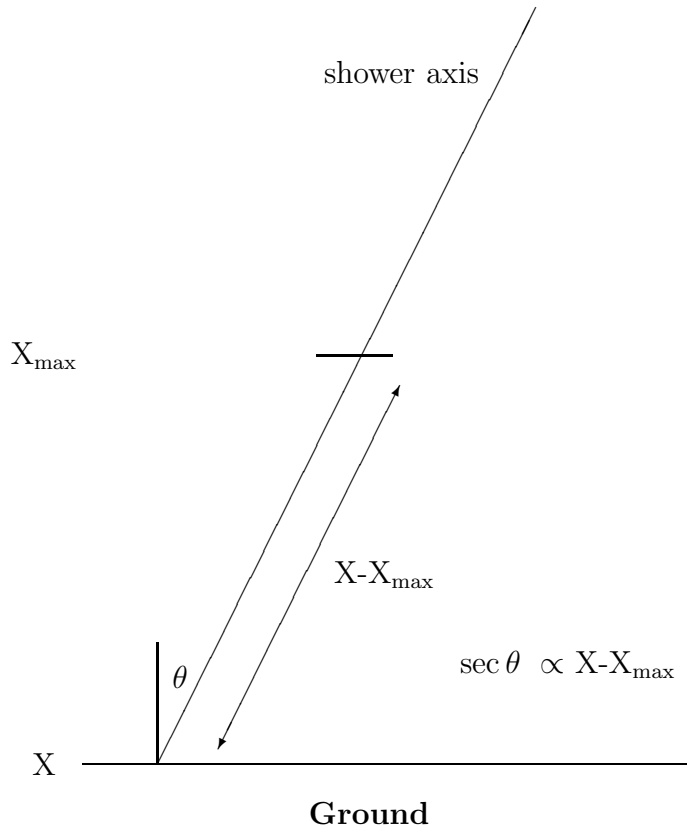

Figure 6.2: The distance through the atmosphere along the shower axis between X and X_{max} is proportional to the zenith angle of the shower. X and X_{max} are atmosphereic depths measured from the *top* of the atmosphere.

stant intensity cut method a set of real reconstructed showers is required. These showers are reconstructed in the same fashion as the monte-carlo showers The events are then divided into zenith bins of 0.1 in the sine squared of the zenith angle and in each bin the events are ordered starting from the one with the greatest S(1000). A cut is imposed at the N^{th} event from the top when N can be any arbitrary value; in our case we used the 150^{th} highest event in each zenith angle bin. The cut is best visualized as taking the S(1000) values obtained when a horizontal line extending from the y-axis at 150 intersects the flux for each angular bin seen in fig. 6.3. In actuality a linear fit using the logarithm of the fifteen S(1000) values above and below the 150^{th} event helps to smooth out statistical fluctuations and it is the central value of this fit that is taken as the S(1000) of the 150^{th} event. The S(1000) values for each sine squared zenith bin are then plotted and fit with a third degree polynomial as shown in fig. 6.4 to obtain an interpolation for intermediate angles.

The choice to use the 150^{th} highest event is arbitrary and a different choice will produce a slightly different curve. Fig. 6.5 is the ratio of the fitted constant intensity cut produced from other choices of event cuts to the chosen cut. It is worth mentioning that constant intensity is only the behavior of the average shower at a given cut in event number. It is the average because each cosmic ray has a unique zenith angle so to cover the available phase space in zenith angle many cosmic ray showers of various zenith angles are needed. If cosmic rays are a mixed composition the assumption of similar events across zenith angles may no longer hold, a possibility that can be explored with this method by choosing progressively higher cut in event for constant intensity and comparing those mappings to monte-carlo.

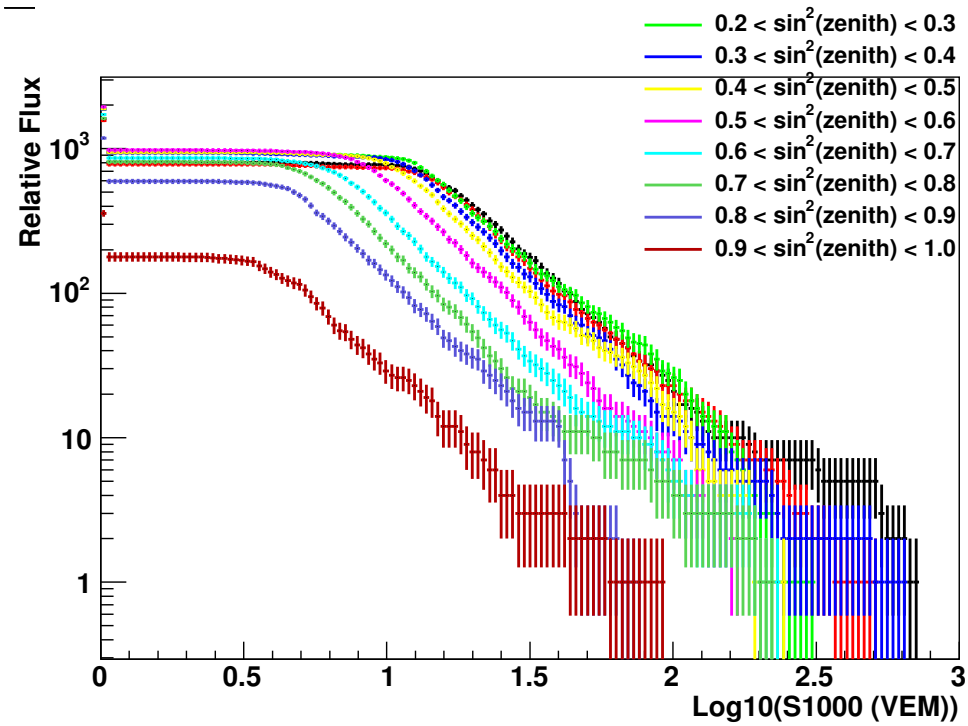

Figure 6.3: The intergral flux of cosmic rays binned by the zenith angle. At increasing values of S(1000) on the x-axis the number of cosmic rays observed above that threshold is progessively smaller. Assuming constant intensity predicts the flux in all angle bins to be the same. The differences seen in the figure are only the result of atmopheric attenuation that differs from zenith angle to zenith angle.

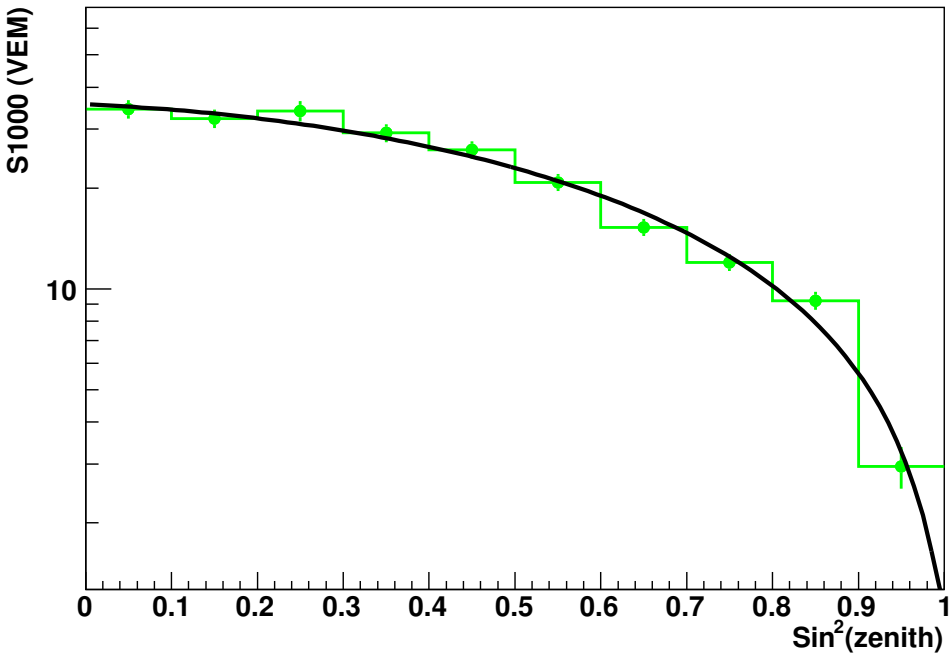

Figure 6.4: Choosing an integral flux of 150 for each zenith bin in fig. 6.3 leads to a corresponding S(1000) value. Plotting the S(1000) values as a function of zenith the atmospheric attenuation curve can be extracted.

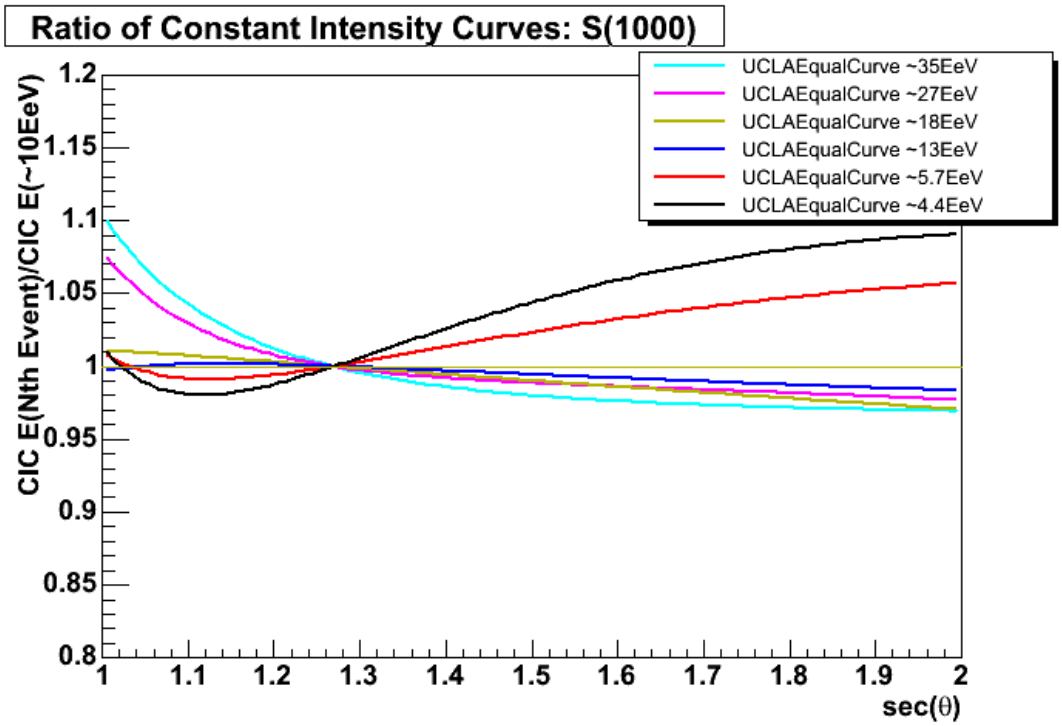

Figure 6.5: The ratio of constant intensity curves obtained at a choice of flux other than 150 events. Choosing a smaller number of events is the same as choosing a higher energy and vice-versa.

6.1.2 Projections in zenith and radius

The first step in making a three dimensional plot is the production of projections in the secant of the zenith angle. It is important to remember that longitudinal development is proportional to the secant of the shower zenith because the average grammage of atmosphere that must be penetrated, and hence the atmospheric attenuation, increases as the secant of the zenith angle. The lateral development is a function of the radial distance and is obtained by choosing to evaluate the signal at a radius other than 1000 meters. In this work we used every radius between 600 and 2000 meters in steps of 200 meters. Intermediate radii are obtained using a linear interpolation between the steps.

Fig. 6.6 is an example of the radius equal to 1000 meters. The curve from the constant intensity cut (shown in black) has been normalized to the proton+qgsjet+aires combination at thirty-eight degrees. If we take the fluorescence normalization at thirty-eight degrees instead, we can plot the ratio of the monte-carlo curves to the fluorescence normalized constant intensity cut curve seen in fig. 6.6. This not only illustrates the relative difference between the normalization methods, it sharpens the comparison we are making between compositions and hadronization models because a monte-carlo that predicted exactly the same shape as constant intensity would appear as a horizontal line when the ratio was taken.

The absolute value of the ratio is determined by the fractional difference between monte-carlo ground signals and the fluorescence normalization using golden hybrid shower as done in [51, 36]. The hybrid calibration associates showers of 10 EeV with much larger signals than the simulations do resulting in ratios that are much less than one. The probable origin of the difference is discussed in [52].

For S(1000) the composition and model that best reproduces the **shape** of

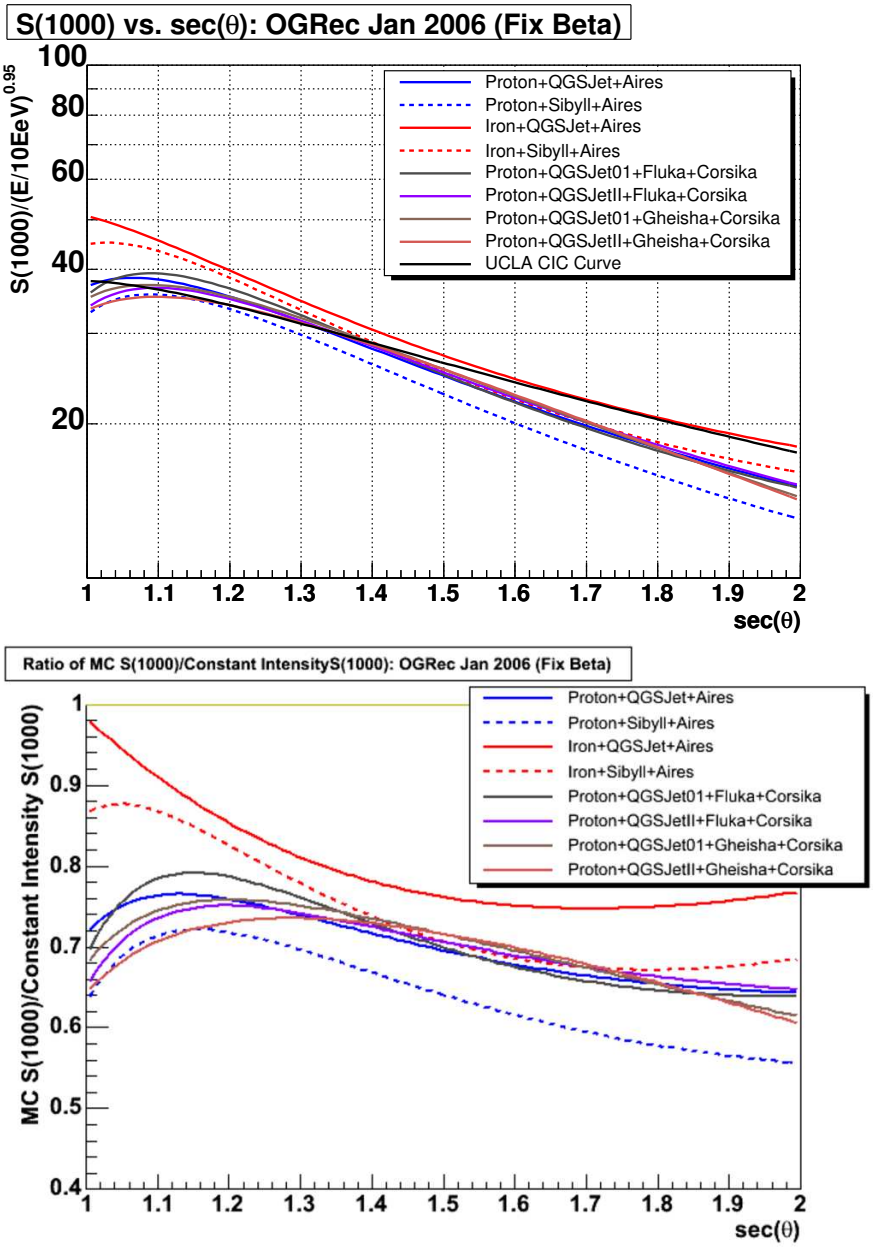

Figure 6.6: **Top:** The predicted attenuation curves at 1000 meters from the shower core by various simulations. The Constant Intensity Curve is shown normalized to the aires+proton+qgsjet simulation as well as using the hybrid technique. **Bottom:** Taking the ratio of each simulated attenuation curve by the constant intensity curve using the fluoresence normalization.

constant intensity is the combination of proton+qgsjet, a combination that differs from the fluorescence normalization by 26% at a zenith angle of thirty-eight degrees (recall this angle is the point we use to normalize the constant intensity curve).

Floating beta in the reconstruction allows a meaningful prediction of particle densities at the other distances (S(r)). They are correlated to S(1000) but are independent as they depend on the lateral distribution of shower particles. A broader distribution of particles on the ground tends to make the beta parameter smaller while a tight distribution results in a larger beta during the fitting of a lateral distribution function explained in section 7.1. Fig. 6.7 is a selection of attenuation curves for three different radii. The ratios to the constant intensity curve is shown in fig. 6.8.

6.2 Mapping the 3-dimensional shower development

With the parameterization of the particle density as a function of the zenith angle and the linear interpolation between radial distances complete, a fully three dimensional shape of particle densities can be created for each monte-carlo (see fig. 6.9) as well as the constant intensity cut.

The particle densities observed by the Pierre Auger surface detector fall within the lower right quadrant of fig. 6.1. Dividing the monte-carlo predicted shapes by the shape of constant intensity will produce a flat plane (just as it would produce a flat line in the previous section) if that monte-carlo predicts that same particle densities throughout the phase space. None of the models are truly satisfactory as shown in fig. 6.10.

The absolute value of the ratio is set by fluorescence detector data.

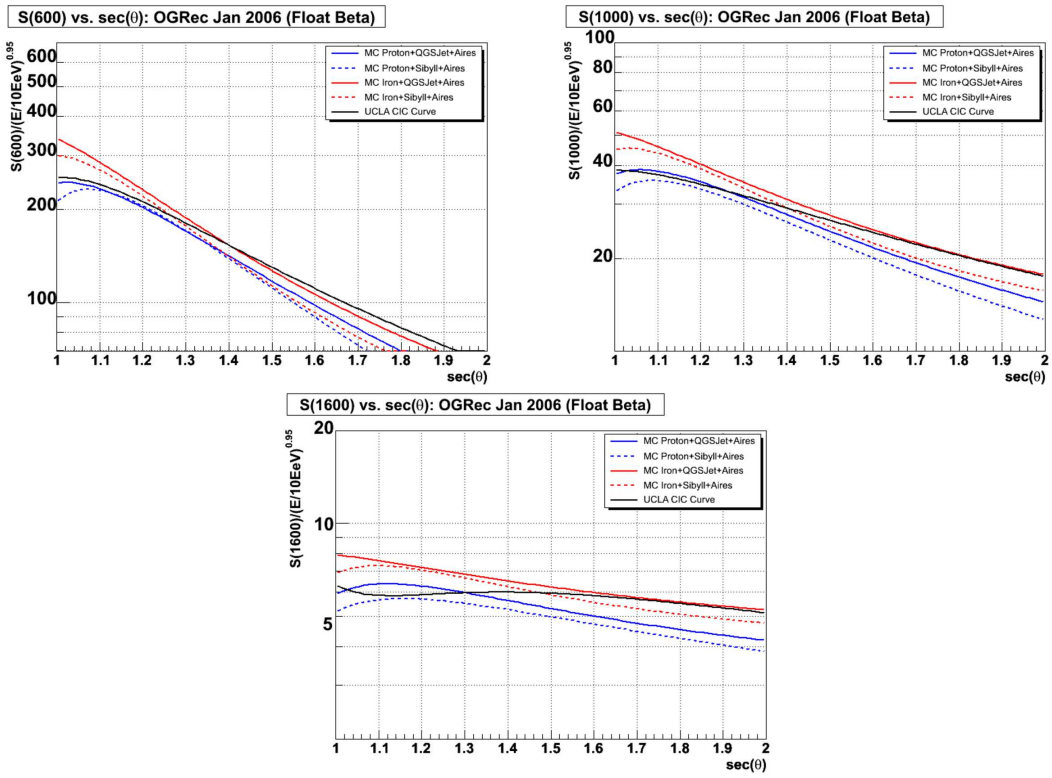

Figure 6.7: The comparison between monte-carlo shapes of the attenuation curve at three different radii. The constant intensity curve at the same radius is shown as a black line.

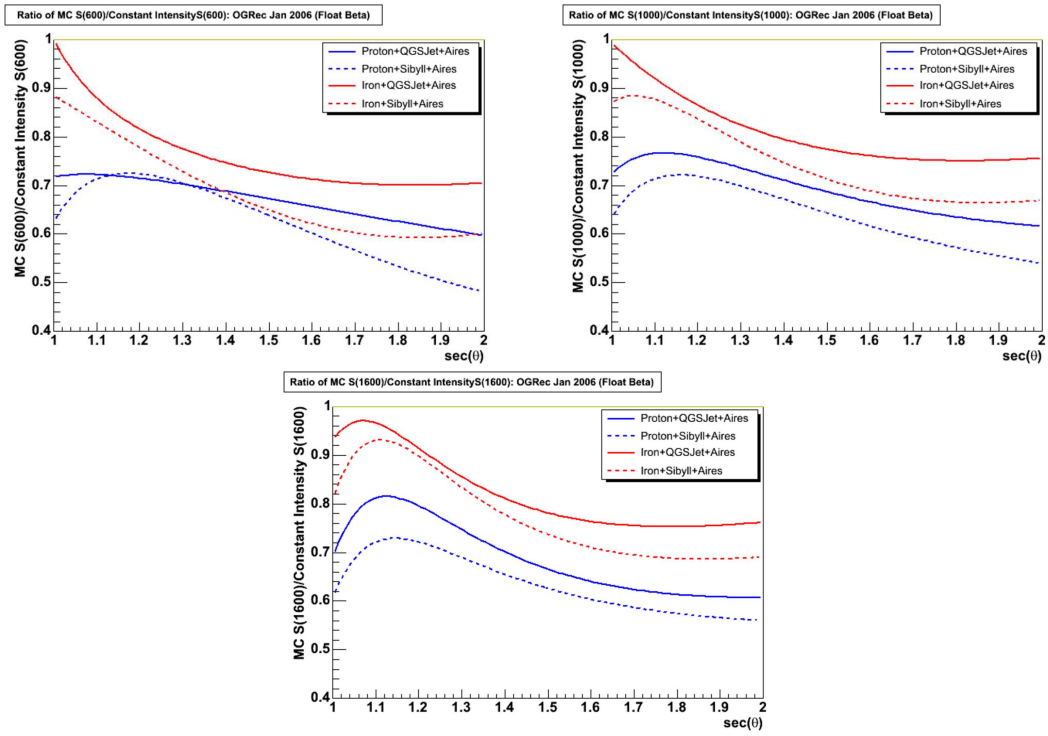

Figure 6.8: The comparison between monte-carlo shapes of the attenuation curve at three different radii. The difference relative to the fluoresence normalized constant intensity curve is shown.

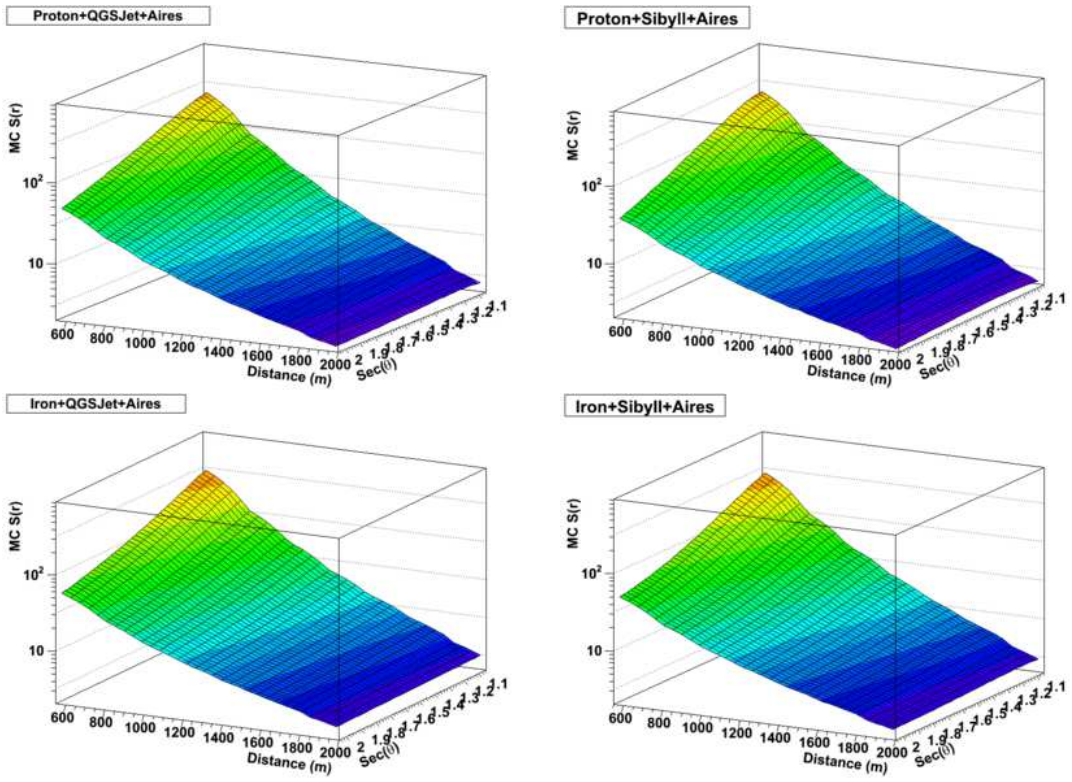

Figure 6.9: The predicted surface obtained using four representative models. The surface is limited to the lower right quadrant (quadrant number four) of fig. 6.1 because that is the portion of an air shower observable with the Pierre Auger surface detector.

6.3 Conclusions

We have covered the phase space in both the shower zenith and the distance from the shower core. Using that information it is possible to evaluate the full development of extensive air showers in both the lateral and longitudinal directions using only information from the surface detector. The Pierre Auger Observatory is fortunate that the altitude of the detector is situated in the vicinity of X_{max}. Due to this fact a local maximum at 1000 meters is observable in the attenuation

curve. Multiple scattering in the atmosphere results in a delay of X_{max} at increasing radii and this local X_{max} (which we will refer to as X_{max} despite the fact that the traditional X_{max} occurs at a different atmospheric depth) is useful for composition. At 1000 meters for vertical 10 EeV proton showers this X_{max} is predicted to be underground. As the zenith angle of an incident shower increases, X_{max} passes through the observing level (the ground) to a point well above the surface detector in terms of atmospheric depth. If primary cosmic rays are protons this effect should be clearly evident in the form of a maximum in the constant intensity curve at the angle where X_{max} coincides with ground level. Angles greater

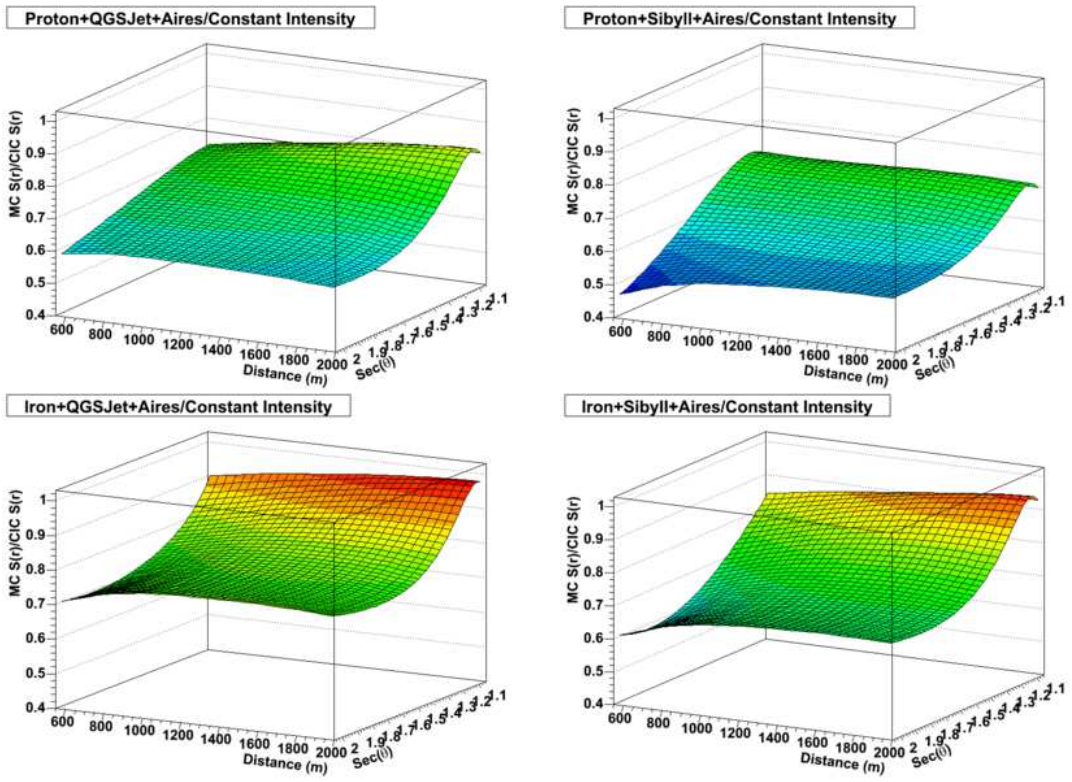

Figure 6.10: The ratio of the surface predicted by simulation to that obtained from real data using the constant intensity method. A perfect reproduction results in a flat plane.

than or less than that angle are predicted to yield a smaller S(1000) because the particle number and subsequently the particle density is not at its maximum.

The situation for showers inclined by more then forty-five degrees is also interesting. In these cases X_{max} is sufficiently removed from the observing level that the muonic component of the shower begins to dominate the signals on the ground. At an incident angle of sixty degrees the electro-magnetic cascade is reduced to the point that these showers are essentially a comparison of the muon number between observed showers and those simulated by monte-carlo.

The shape of the constant intensity cut curve exhibits the maximum expected if the primary particles are protons however the inclined showers suggest a muon richness exceeding that of both a monte-carlo proton or a monte-carlo iron primary. This picture of cosmic rays with a proton like X_{max} but an iron (or greater) like muon richness is inconsistent with the models shown in fig. 6.11. The implication is that the monte-carlos do not well represent the muon richness.

The relative ratio between the fluorescence normalized constant intensity cut and the simulated energy converters remains relatively constant regardless of the distance chosen to evaluate the lateral distribution function. Even far from the core where the showers are almost exclusively muons the ratio is essentially the same. If simulated showers are missing muons we would expect the ratio to change as the ground particle densities become increasingly dominated by muons. The fact that it does not is inconsistent with the idea that simulated showers are missing muons.

6.3.1 $\mathbf{X}_{max}$

It is known that protons on average have a deeper shower maximum (Xmax) than iron primaries. The Pierre Auger Detector is located at an elevation of

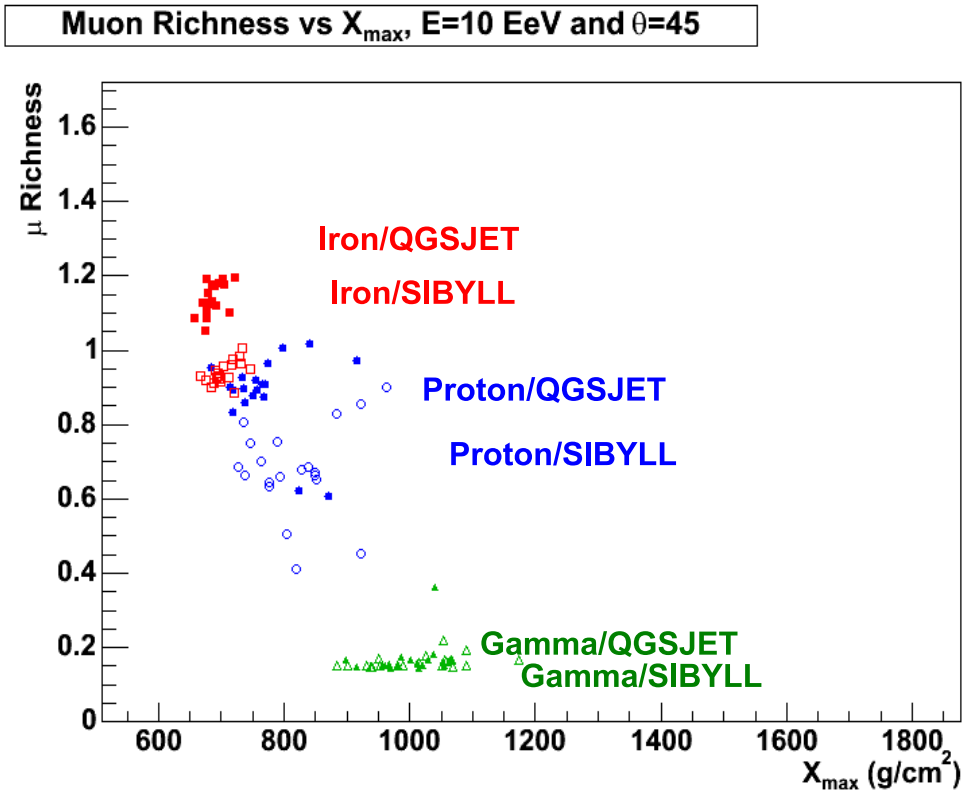

Figure 6.11: The location of several models in the space of X_{max} and muon richness. The combination of a proton like X_{max} but an iron like muon richness does not exist.

1400 meters, which corresponds to roughly 870 g cm^{-2} of atmosphere vertically. This depth of 870 g cm^{-2} just happens to be similar to the depth proton showers reach X_{max} at 1000 meters, therefore we expect vertical proton showers to reach the X_{max} past the observation level of the surface detector. This is in contrast to iron showers which reach that X_{max} before the observation level of the surface detector. The net effect is that for protons the particle densities will increases slightly as the showers become inclined until the average X_{max}, and hence N_{max}, is right at the observation level of the surface detector. After that point the particle densities will decrease with increasing zenith angle. This turn-over will not be observed for iron because X_{max} occurs before the observation level of the detector even for the vertical case therefore the particle density decreases in the familiar exponential fashion when plotted as a function of the secant of the zenith angle.

6.3.2 Muon richness

For highly inclined showers the additional atmosphere penetrated reduces the electromagnetic portion so much that the remaining particles are primarily energetic muons at the observing level of the detector. Primary cosmic ray protons produce fewer of these muons than an iron primary and therefore also produce a smaller particle density on average. This is observed for the two compositions as well as between hadronization models because qgsjet tends to produce more muons than sibyll. When these simulations are further compared to the constant intensity cut curve we can see that the real data is predicting a muon content that exceeds even the most muon rich combination of iron and qgsjet.

6.3.3 Model systematics

It is clear that the model differences are extrema for both vertical and inclined showers. For middle zenith angles, showers of the same energy produce a similar S(1000) regardless of the assumptions about primary or hadronization model. In the case of S(1000), showers with a zenith angle of 38 degrees are the least influenced by composition and/or model. The systematic differences between monte-carlos can be further reduced by using S(600) (see fig. 6.12), because as we move closer to the shower core the electromagnetic cascade is the largest contributor to the observed signals and as is the case in fluorescence this part of the monte-carlo is the most reliable.

At the minimum of S(600) - 38 degrees the systematic difference between monte-carlos is reduced to ten percent. However even at this minimum systematic difference between monte-carlos' the fluorescence predicted S(1000) is still over twenty percent higher for a 10 EeV shower. It is unlikely, even given the short comings that have been identified in the monte-carlo, that this difference is solely due to simulations. Therefore it is likely that the fluorescence determined normalization is at least ten percent (possibly twenty percent) too high.

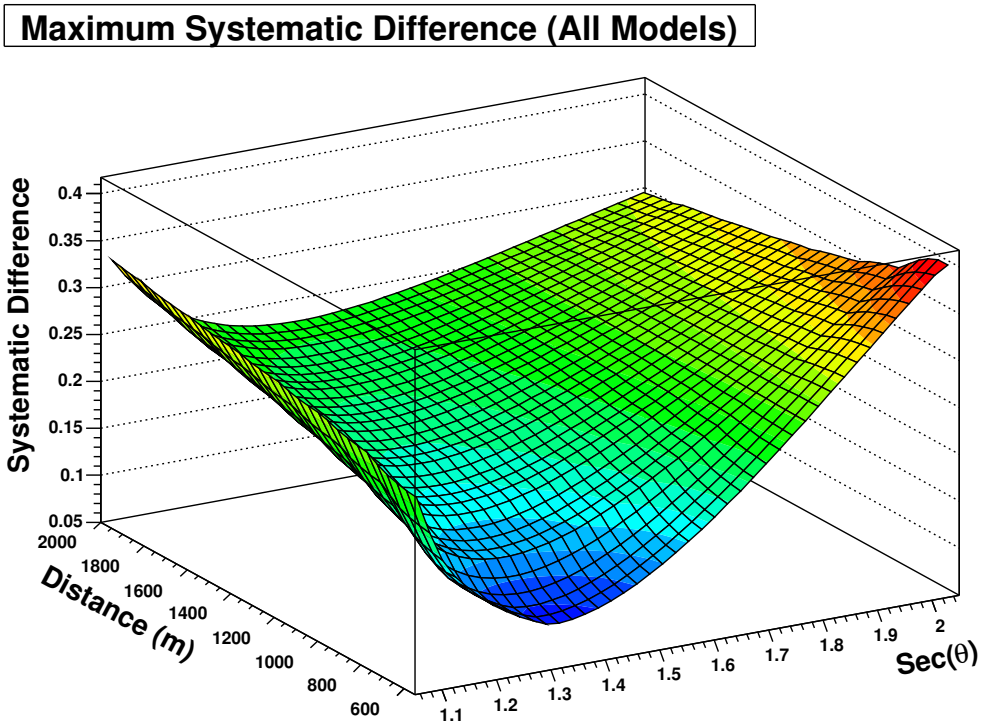

Figure 6.12: The surface created by taking the largest systematic difference in the predicted ground particle density between the four combinations of model (qgsjet01c or sybill 2.1) and primary (Proton or Iron). The minimum is the zenith angle and core distance for which the best agreement between the simulations is realized.

CHAPTER 7

Composition Analysis of Ultra-High Energy Cosmic Rays with the Surface Detector

The principle of universality posits that air shower development can be described completely by three fundamental parameters: the number of charged particles at the shower maximum (N_{max}), the depth of shower maximum (X_{max}), and finally the muon content ($\mu_{richness}$ - when expressed as the ratio of muons to electrons at their respective maxima). The first of these is linked to the primary energy while the latter two are most frequently associated with the primary composition. Fluorescence detectors maintain an advantage over surface detectors because they directly measure X_{max} during shower reconstruction, the surface detector by contrast does not. The surface detector disadvantage in direct measurement is offset by indirect sensitivity to both the shower maximum and the $\mu_{richness}$[1], plus a data rate nearly an order of magnitude higher. Composition analysis utilizing the surface detector is a trade off - statistics for sensitivity.

7.1 Surface Detector Analysis Methods

The strength of a surface detector is exposure. Due to the near 100% duty cycle far more cosmic rays can be detected with an array on the ground than in an

[1] muons do not contribute in any meaningful way to air fluorescence

equivalent amount of time with a fluorescence detector. The different techniques lead to independent reconstruction methods but the goal is always the same: the best possible measurement of the original energy, direction, and mass of the primary.

From the point of view of a cosmic ray shower the surface detector is a plane with essentially no vertical extent. All the information is obtained when the shower front passes through the plane, and because the stations are spaced fairly sparsely so too is the sampling of the shower front. There are many ways of implementing the details of a reconstruction of the raw surface detector data, however the following will describe the principles behind the "offline" [38] reconstruction because that software is the basis for the analysis in the next sections.

Acceptance

Acceptance is a measurement of the detectors ability to observe a given cosmic ray shower. Since the shower front is only sampled where there are stations it is possible for a very small shower to simply miss (the trigger requires at least three stations to be "hit"). These small showers are low energy, but as the energy increases so too does the footprint of the shower and eventually a point is reached where virtually no matter how the shower lands the trigger conditions will be met. For the Pierre Auger surface detector the saturation point is defined to be the energy when 90% of all cosmic rays would be detected, a condition that is satisfied at an energy of 3 EeV [21].

Angular reconstruction

The angular reconstruction is obtained from the timing. That is to say that each station records, with nanosecond accuracy, when the first particle of the

shower arrived. When multiple stations are triggered it is possible to triangulate the direction the shower front is approaching from by assuming the shower front can be approximated as a plane of particles all traveling at the speed of light (c). The accuracy of the reconstructed approach vector increases with triggered station multiplicity (see fig. 7.1) and, the flatness of the shower front since a plane is assumed (showers that develop higher in the atmosphere, or those with a greater number of muons tend to have flatter shower fronts).

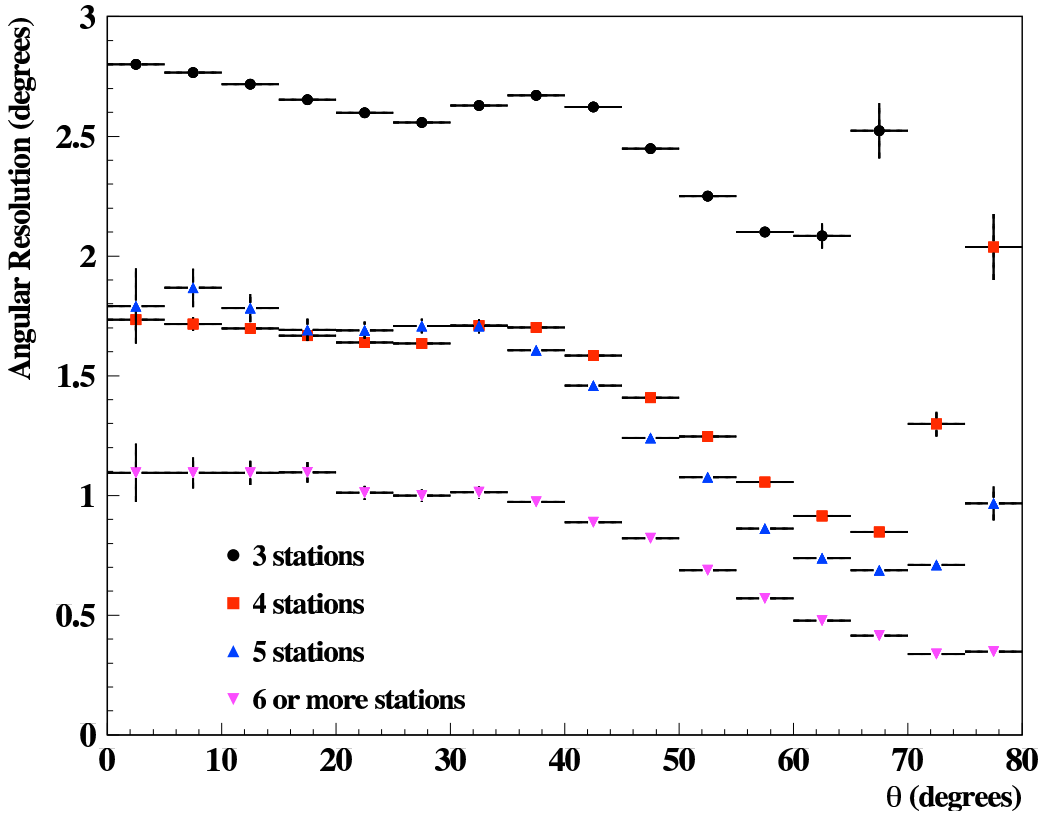

Figure 7.1: The surface detector is excellent at obtaining the pointing direction of the original cosmic ray. The accuracy improves with the number of stations triggered and the inclination of the shower. Values comparable to 1.5° are common for showers with an energy ∼10 EeV and above. Graphic obtained from [17].

The lateral distribution function

Energy reconstruction with a surface detector is based on an integration of the number of particles that pass through the detection plane multiplied by the average energy of the particles.

$$\text{Total Energy} \propto \sum_i \mathrm{E}_i \cdot \int_0^\infty \mathrm{N}_i(|\vec{r}|)\, dr$$

$\mathrm{N}_i(|\vec{r}|)$ is the density of shower particle species i at distance $|\vec{r}|$ from the shower core

E_i is the average energy for shower particle species i at the detector

In reality the integration method above is not actually used during the reconstruction of surface detector showers but the concept is the same. The function $\mathrm{N}(|\vec{r}|)$ is a description of the particle densities as a function of distance from the shower core and qualitatively we expect something large near $\vec{r} = 0$ that decreases with increasing distance. $\mathrm{N}(|\vec{r}|)$ is called the *lateral distribution function* and its form must be assumed. The assumption is guided by real showers and a desire to choose something that accurately describes the density of particles regardless of the individual shower characteristics.

$$f_{\mathrm{LDF}}(r) = \left(\frac{r}{r_{1000}}\right)^{\beta} \left(\frac{r + r_{700}}{r_{1000} + r_{700}}\right)^{\beta+\gamma} \tag{7.1}$$

with r_{700} =700 m. Initial estimates for β and γ are obtained as in [38]). The error on the signals this fit is done against are from twin tank studies [53].

$$\sigma_S(\theta) = (0.32 + 0.42 \sec\theta)\sqrt{S} \tag{7.2}$$

In an individual event the density of particles is sampled at each station and the above formula is fit to that data so the density can be interpolated at all

distances. Rather then integrate the density to arrive at a total, a reference point is chosen and the density is simply evaluated at that point. Everything else being equal, the larger the density the greater the energy of the shower. In actuality the density depends strongly on the shower's zenith angle as well as weakly on any number of atmospheric conditions, however the zenith angle is already known and the weather can be monitored so those effects can be factored out to arrive at a number that is well correlated with the calonometric energy measured by the fluorescence detector as shown in fig. 7.2. The other function of fitting the LDF is to determine the shower core. The process begins with an initial guess based on the station signals and their distances from each other. The guess is the "center of mass" of this system and is used to initially place the stations at distances from the estimated core. During the fitting process the core position is also floated.

S(1000)

As was mentioned above, energy measurement is done from a reference point on the LDF. A prime concern (but not necessarily the only one[2]), are statistical errors. In this case the dominant statistical error comes from the variation in X_{max} of the shower. Surface detectors are not capable of directly measuring X_{max} of a given shower and therefore as X_{max} fluctuates so too does the signal at the ground. The result is a statistical error in the ground energy deposit based on the depth of shower maximum. The uncertainty can be reduced by an intelligent choice of reference distance at which the LDF is evaluated. Given the altitude, detector spacing, and cosmic ray energies of interest to the Pierre Auger Observatory the

[2]depending on the method used to convert the reference value to a final energy it can be advantageous to choose other reference points and accept the larger statistical uncertainty

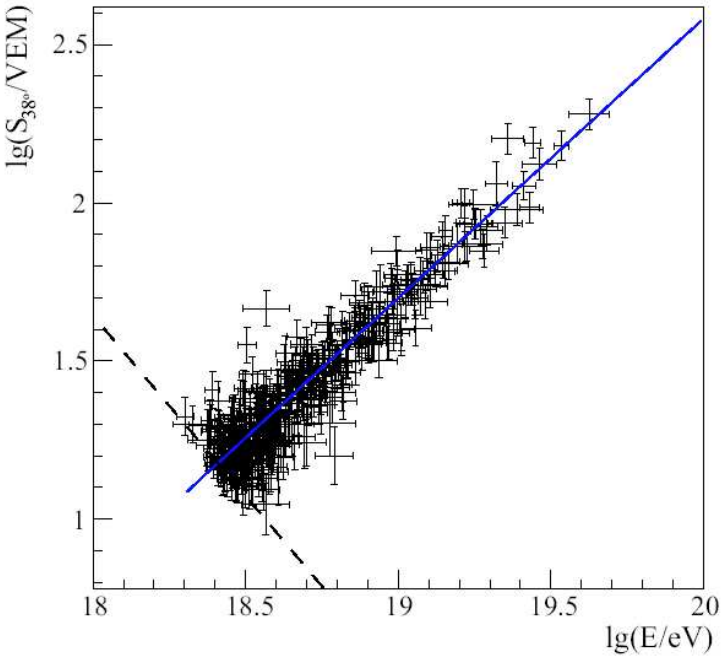

Figure 7.2: The ground parameter S(1000) as a function of the energy determined by the fluorescence detector for golden hybrid showers. Each black point is an event with the associated statistical uncertainty in S(1000) and energy. The data are fit with a single power-law through an iterative procedure designed to eliminate bias in the results by removing low energy events to the left of a line normal to the best fit. The solid blue line shown is the fit after convergence. The dashed black line is the anti-bias cut normal to that fit. Graphic obtained from [51].

best choice is 1000 meters from the shower core. This distance is special because of the 1.5 km spacing of the stations [54].

Shower front shape

The final reconstruction step is to remove the assumption that the shower front is planar. Rather a spherical shower front is assumed and that geometry is fit to the station trigger times. Although there is no a priori reason to use a spherical front it does have some advantages.

> ...[The] spherical model is the simplest model there is. It does not imply a notion of axis as [a] parabola does with its cylindrical symmetry. You do not need [a] core location to fit for sphere. (apart from the time variance model) It is station-time fit only. You do not need to fit [the] ldf first (or iteratively later).
> *Darko Veberic, Private Communication*

The usefulness of including the curvature of the shower front is a more accurate determination of the shower axis. Combining a timing fit, as in the angular reconstruction, with the fit for the core location during the LDF stage, a shower axis is defined. By using the initial plane fit as a first approximation the curvature fit can be performed with an initial value that is already defined. The initial value also serves as a constraint on the magnitude the improved timing fit is allowed to alter the incident angle. When possible, fitting the shower front with a curve leads to an improvement of the overall angular reconstruction. Additionally, the shower front curvature is also sensitive to the mass of the original primary and is therefore useful in that respect as well.

7.2 Software

Hardware and software are integrally linked in a modern experiment like the Pierre Auger Observatory. While some software is used to operate the hardware other software is used purely in the analysis phase. The tools provided for analysis are as important as the actual detectors for obtaining reliable results in an efficient and reproducible manner.

7.2.1 Shower simulation software

Simulated showers are created for the purposes of testing and tuning analyses, or the estimation of parameters that are either difficult or impossible to measure from real data. Simulation of a surface detector relies on accurately reproducing the true distribution of shower particles on the ground in every way including (but not limited to) the locations, energies, arrival times, and individual directions with some applications depending heavily on accuracy in one aspect more than another. For specialized cases the simulation can be tuned for the specific task at hand gaining efficiency. Ideally simulations track the creation, propagation, and destruction of every particle in the air shower, from first interaction until the ground. Unfortunately the computing resources to carry out such a detailed simulation are at present quite limited so a technique called thinning is employed. Thinning is a method whereby the enormous number of low energy particles are merged into a single particle that carries an additional variable called the weight, representing the number of particles the merged one now represents[3]. The thinned shower is saved in this state to reduce the disk space required for

[3]this saves the computing time needed to follow each individual particle explicitly

additional energies, momenta, and positions if the shower had not been thinned[4]. The exact energy at which thinning begins is a user definable parameter often called the thinning level with typically "good" values in the range of 1-100 TeV for ultra-high energy cosmic ray simulations. A second limitation of air shower simulations stems from the energy of the primary cosmic ray. The first several interactions occur at energies higher than any Earth based accelerator, and the cross section for various strong force interactions have not been measured but instead must be extrapolated from data at lower energies. This uncertainty is evidenced by the array of *hardronic interaction models* available and the range of results they produce. A few of the common ones are qgsjet01c [42], qgsjetII [55], sibyll [43, 56], and a comparatively newer model called EPOS [57][5]. Two common shower simulation packages that I used are Aires and Corsika. A short description of both packages is next.

7.2.1.1 Corsika

Corsika [58, 59] is an air shower simulation package widely used in surface detector simulations. Simulated air showers can be initiated by a variety of primary particles and the user has a good number of choices for interaction models at both low [60] and high energy. Optimizations are available for specialized uses, including thinning, and the output files are compatible with the detector simulation software used by the Pierre Auger Collaboration.

[4]the space saved is roughly computed as the substitution of a weight for an energy-momentum vector and a 2D position (z is fixed to ground), for a saving of about a factor of six

[5]I frequently abbreviate the various models, be on the lookout for shortened names or first letters as substitutes for the full model name

7.2.1.2 Aires

AIRES [44] is another widely used air shower simulation package. It does not have the variety of interaction models that Corsika offers but it does cover the common ones from above except for EPOS. There are differences in the handling of low energy hadronic interactions as well as electromagnetic interactions, but on the whole results are similar. Primaries of various masses are allowed and thinning is also available, although unlike Corsika the thinning level is affected by the primary energy. One great advantage is the output file size which is much smaller than Corsika. The output files are compatible with the Pierre Auger detector simulation software.

7.2.1.3 The offline

The second step for shower simulation is turning the particle distribution on the ground into the corresponding response of the detector. This is done largely by software produced internally for the collaboration and it goes by the name of **The Offline**. The structure is modular with each step in the simulation handled in order with the output of one being fed as input to the next. The tank simulation, which involves the propagation of particles through matter, uses the Geant4 [62] package to produce and track Cherenkov photons until they are incident on the photomultiplier tubes. From there the simulation proceeds through a simulation of the photo-tubes, followed by the electronic response to the photo-tube output and so on down through station level triggers and finally the array level trigger. The output of this process is indistinguishable from data collected by the actual array and can be fed to the reconstruction as if it were a real shower.

```
<sequenceFile>
   <loop numTimes="unbounded">
     <module> SimShowerReader </module>
     <loop numTimes="10">
        <module> EventGenerator </module>
        <module> TankSim        </module>
        <module> TriggerSim     </module>
        <module> EventExporter  </module>
     </loop>
   </loop>
</sequenceFile>
```

Figure 7.3: Simplified example in which an XML file sets a sequence of modules to conduct a simulation of the surface array. `<loop>` and `<module>` tags are interpreted by the Run Controller, which invokes the modules in the proper sequence. In this example, simulated showers are read from a file, and each shower is thrown onto the array in 10 random positions by an `EventGenerator`. Subsequent modules simulate the response of the surface detectors, trigger, and then export the simulated data to file [61].

7.2.2 Shower reconstruction software

The Offline also functions as the primary reconstruction software. In this usage the modules are processed in the order necessary to fully reconstruct the primary cosmic ray, direction, energy, and in so far as possible the particle type.

By default the surface reconstruction is processed by the chain of modules shown in fig. 7.4. Each module handles a step in the reconstruction process with the goals of the most basic reconstruction being an energy and a direction. The default reconstruction (see fig. 7.5) also calculates a number of observables useful for composition analysis as side effects of determining the shower energy and direction. The most important of these are the curvature of the shower front which comes from the reconstruction of the shower direction and the slope of the lateral distribution function (beta) which is a part of the energy reconstruction.

```
<sequenceFile>
   <loop numTimes="unbounded">
      <module> EventFileReaderOG </module>
      <module> SdCalibratorOG </module>
      <module> SdEventSelectorOG </module>
      <module> SdPlaneFitOG </module>
      <module> LDFFinderOG </module>
   </loop>
</sequenceFile>
```

Figure 7.4: The basic sequence to read in real or simulated shower data and perform a reconstruction on that data.

7.2.3 FADCPulseParametersUCLA

The default reconstruction can be augmented to include additional modules designed to calculate other useful observables. Many of the composition studies to date [34, 45, 4] as well as section 5.3.3 have relied on the time structure of the shower front, in particular on the **risetime**. The module FADCPulseParametersUCLA is responsible for the determination of this observable for use in later analyses. The module was coded exclusively at the University of California, Los Angeles and as it forms the basis for the analysis in this thesis and the basis for the photon limit of the surface detector [63] the full source code can be found in appendix A. Fig. 7.6 is an example of the algorithm applied to a real event. The first step is a determination of a risetime corrected for shower asymmetries due to the zenith angle. The uncertainty on the risetime is derived from twin-tank studies [53]. Finally a plot of risetime as a function of core distance is produced and then fit with a second order polynomial. Typically the value interpolated at 1000 meters is used as the risetime of the entire event.

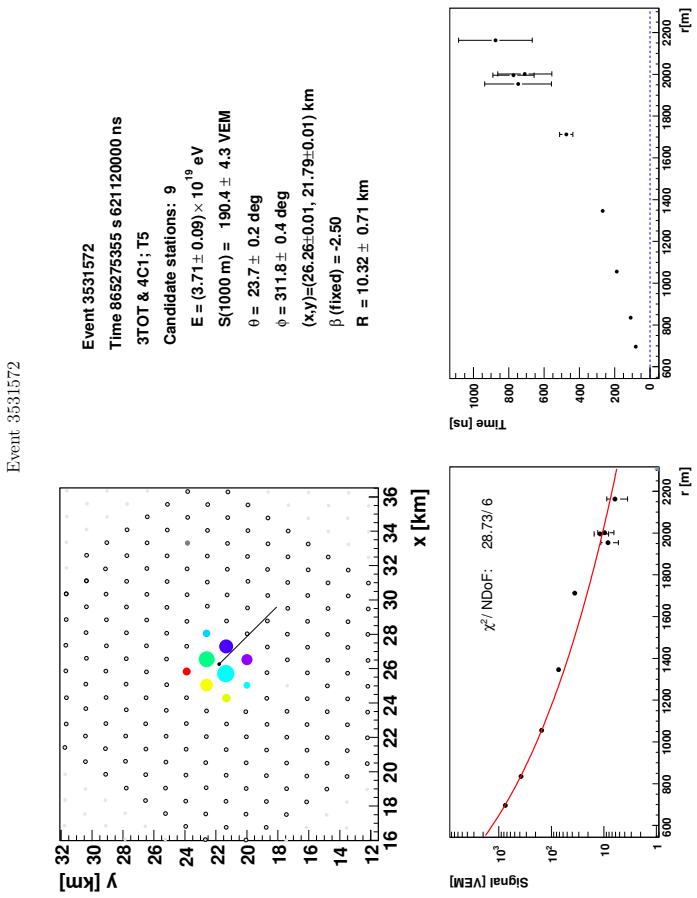

Figure 7.5: Using the offline reconstruction and the module sequence in fig. 7.4, an event can be completely reconstructed. This display is event 3531572. A view of the surface array with the triggered stations is shown along with the LDF fit and the timing of the triggers relative those expected if the shower front was a plane. The final reconstructed values are displayed as text.

7.2.4 Composition analysis software

Determining the composition of primary cosmic rays is a task that relies heavily on shower simulations to draw conclusions. For this reason it is imperative to

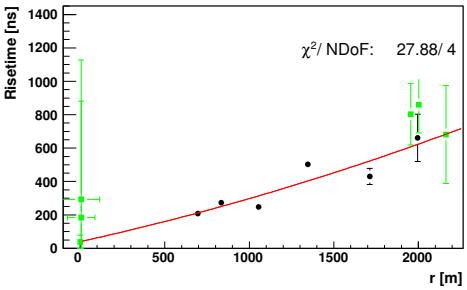

Event 3531572

Candidate stations: 9

E = (3.71 ± 0.09) × 10^{19} eV

θ = 23.7 ± 0.2 deg

ϕ = 311.8 ± 0.4 deg

Risetime = 297.71 ± 46.24 ns

Xmax = -1.00

Xmax Error Up = -1.00

Xmax Error Down = -1.00

Figure 7.6: **Left:** A fit to the risetime for event 3531572. The green markers are stations not used in the fitting procedure. **Right:** The results from the fit to the risetime and some details about the event.

design analysis software that is capable of handling both real and simulated data in a coherent and, in-so-far-as-possible, agnostic way. That is to say the software should treat simulated inputs in exactly the same fashion as real inputs, even utilizing the same source code when possible. The *offline* software produced by the Pierre Auger Collaboration follows this principle by providing a simulation chain that mimics the data collected by the actual detector. The reconstruction can then proceed in an identical manner whether the shower was real or simulated. This approach has been adopted for an analysis of primary composition as well.

Three primary tasks are identifiable to build a conversion from surface detector observables to X_{max}.

1. Provide access to the data, both real and simulation.

2. Build a conversion based on some data that can then be applied to other data.

3. Produce results in a manner that allows checks to be done and conclusions

to be drawn.

The tasks above are necessarily abstract. It is not clear before the analysis is complete what the conversion will entail, and by corollary what "checks" might need to be investigated. Therefore the specific properties can not be determined and the number of possible implementations is uncountable. Providing access to data is the most concrete task in that the number of different sources of data was known at the outset.

UCLA Data Shower reconstructions done locally at UCLA. Stored as a ROOT [27] *Ntuple* containing custom fields for reconstructed parameters.

ADST Data ADST is an acronym for Advanced Data Summary Tree. This is also a ROOT [27] file but in this case containing non-ROOT objects. This was a new format whose purpose was to provide a uniform method for distributing reconstructed data throughout the collaboration. The files contain not just numerical results but also enough information to provide a visual display of the reconstructed shower.

Flat Text Data A simple text file containing the numerical values of interest. This is the most basic way to maintain inputs for an analysis and as such should be included if, for no other reason, than any sources of data can always be converted to flat text and then read in via this method.

In addition, each of these formats can contain real data or simulated data and the reconstruction method can be either surface detector alone, fluorescence detector alone, or both together (hybrid). This leads to quite a few possibilities, but is definitely an improvement over the situation with the first two tasks.

Because each of the three primary tasks has multiple possible realizations an abstract interface for each of the tasks was the most appropriate design.

Therefore the analysis software contains three base classes, each with polymorphic characteristics. The base classes fill the traditional role, providing virtual functions for the methods all derived classes have in common. A pseudocode example in fig. 7.7 demonstrates the usefulness of this approach. Notice parameter two of the function `MakeXmaxVsEnergy()`‡, it is of type `Observable` not of type `FluorescenceDetectorData`. Yet the program accepts the call to `MakeXmaxVsEnergy()` in the main part of the program despite the type mismatch. This is allowed because `FluorescenceDetectorData` derives from `Observable`. If the various types of data (surface detector, fluorescence detector, discrete monte-carlo, etc.) did not derive from a common base, `Observable`, the function `MakeXmaxVsEnergy()` would have to be copied for each type of data with only minor differences. Furthermore, if a bug was found or a change was made the developer would have to remember to change each copy.

Besides the traditional functionality mentioned above the polymorphic interface allows one other useful trait; the tasks can be expanded to include functionality not foreseen at the outset simply by adding a new derived class to the base class for that task. This is particularly important for the `Parameterization` class where it is not clear at the start how many and in what fashion the surface detector observables will combine to yield the final composition result. All that is required to introduce a new type of parameterization is a method to build the parameterization and a method to copy the parameterization[6]. Both methods are virtual in the base class so a simple substitution of one parameterization for another in the final analysis code changes the method used to compute primary mass from surface detector observables.

The polymorphic design outlined is essential to the goal that the analysis be

[6]the term parameterization is used loosely here, any method to convert one variable to another is acceptable, it need not rely on a parameterized fit

```
class CompositionResults
{

 public:

  //...

  // Functions to add graphs to the class
  TGraph* MakeXmaxVsEnergy(const char* title, const Observable&
    theData, const double bin_size = 0.5, const bool useBinning =
    true);‡

  //...
};

int main()
{
  // Load the Golden Hybrid Data (a text file)
  FluorescenceDetectorData ADSTGoldenHybridData("GoldenRec_2006.dat",
    eTXT);

  // Declare a variable of type CompositionResults
  // This variable will hold the graphs made
  CompositionResults Results;

  // Make a graph using the Golden Hybrid Data loaded above
  Results.MakeXmaxVsEnergy("Average Xmax vs Energy",
    ADSTGoldenHybridData);

  //...Do other things, draw graph...

  return 0;
}
```

Figure 7.7: Pseudo-code example using polymorphic data structures to minimize code redundancy. `MakeXmaxVsEnergy()` can take any data structure that inherits from the class `Observable`.

transparent to the data source, and it is intentionally general enough to accommodate new methods as the analysis proceeds and expands.

7.3 Motivation

The goal of my composition analysis is a measurement of the shower maximum (X_{max}) by purely surface detector observables. An X_{max} determined by the surface detector alone can not, and should not, replace a direct measurement by the fluorescence detectors but rather compliment it by providing an estimated value for the great quantity of events that escape observation by the more direct technique. I have chosen to use surface detector observables to characterize X_{max}, rather than simply comparing them to predicted values from simulation as was done in section 5.3.3. The reasons for this choice are as follows.

1. X_{max} is a fundamental shower parameter, and together with two other fundamental shower parameters N_{max} and $\mu_{richness}$, are capable of explaining most detector observables. to a combination of these parameters.

2. X_{max} is measured by the fluorescence detector and therefore I can exploit golden hybrid showers to calibrate the simulations and minimize the systematic errors introduced by relying on a particular simulation.

3. X_{max} is a parameter the community at large is familiar with and therefore does not require a detailed explanation of what is measured. Furthermore, the derived X_{max} can be compared directly in the same context as past results on the topic of cosmic ray composition.

The largest potential drawback of transforming surface detector observables to X_{max} stems from item number 1 and the roles of the other two fundamental parameters. Converting a surface detector observable to X_{max} requires that any dependence the observable has on parameters other than X_{max} be adjusted for in the conversion process first or the result contains a systematic effect. Additionally

the fluctuations on a surface detector observable are a combined sum of the measurement uncertainty and the fluctuations introduced due to the effect of the three fundamental parameters as shown in 7.3.

$$\sigma^2_{\mathrm{SD-Observable}} = \sigma^2_{\mathrm{detector-measurement}} + \sigma^2_{\mathrm{N_{max}}} + \sigma^2_{\mathrm{X_{max}}} + \sigma^2_{\mu_{\mathrm{richness}}} \tag{7.3}$$

The variance in $\mathrm{X_{max}}$ from shower to shower is smaller than the variance introduced by the sum of the other terms resulting in fluctuations in the surface detector observable that are large and mostly uncorrelated to the variance introduced by $\mathrm{X_{max}}$. This is true **even** if the conversion is designed to account for the global effects of $\mathrm{N_{max}}$ and μ_{richness}. It is therefore essential to the usefulness of the conversion that it be constructed to maintain as much sensitivity as possible to the variance in the shower maximum.

7.3.1 Data selection

The principal technique used to guarantee the variance in $\mathrm{X_{max}}$ is measurable is to select the best quality cosmic ray events and take them as representative of the entire sample. The selection criteria are much more than the simple reconstruction success and aperture requirements used in constructing a spectrum [51]; although those are applied as well. Rather, the cuts select the "best-of-the-best" events in the hope that these cosmic rays are constrained so well that the surface detector observables allow $\mathrm{X_{max}}$ to be reliably extracted.

The exact selection criteria depend on the observable in question and are best broken into four categories.

1. Cuts that apply to all events

2. Cuts for the risetime

3. Cuts for beta (the exponent in the lateral distribution function)

4. Cuts for the radius of curvature

Because of the requirements to determine each observable and differences in the amount of X_{max} information contained within, the three observables use different selection criteria. It is possible that some events allow an estimate of X_{max} from one or two of the observables but not the other. In general the criteria are most important at the lower energies because in surface detector events the number of triggered stations, and therefore the amount of information collected, largely determines how well constrained the event is. Since the number of triggered stations scales with energy the highest energy events are the best constrained and nearly always pass the cuts for all three observables. At lower energies many events are discarded and in this region it is particularly important to show that the selection is not a bias against certain values of X_{max}. The criteria are listed in table 7.1. The development of the criteria was guided by shower simulations

Table of Selection Criteria

General Cuts	Risetime Cuts	Beta Cuts	Radius of Curvature Cuts
Energy$\geq$*3.0 EeV*	$\sigma_{\text{risetime}} \leq$*100.0 ns*	*Energy*$\geq$*8.0 EeV*	*Energy*$\geq$*9.0 EeV*
0.0$\leq \theta \leq$*70.5 degrees*	*20.0*$\leq \theta \leq$*55.0 degrees*	*5.0*$\leq \theta \leq$*60.0 degrees*	*0.0*$\leq \theta \leq$*40.0 degrees*
# of Stations$\geq$*4*	*50.0*$\leq t_{1/2} \leq$*1*$\cdot 10^5$ *ns*	$\sigma_{\text{beta}} \leq$*10.0*	*# of Stations*$\geq$*5*
The Event is a T5		*Beta* $\frac{\chi^2}{Ndof} \leq$*1.5*	R_c $\frac{\chi^2}{Ndof} \leq$*5.0*
Reconstruction Stage$\geq$*4.0*		*Beta is* **not** *fixed and no saturation*	$\sigma_{\text{curve}} \geq$*80.0 m*
			1.0$\leq R_c \leq$*1*$\cdot 10^5$ *m*

Table 7.1: The four principle categories of selection criteria. The general cuts are applied to every event and then depending on the surface detector variable used the corresponding cuts are subsequently applied.

and a more detailed discussion of the process can be found in section 7.4. For

now a look at the biases will suffice.

7.3.1.1 Cut biases

A direct method of searching for biases in X_{max} introduced by the selection criteria is to apply the selections to the set of golden hybrid showers and plot the elongation rate. Since the entire set of original showers were observed by the fluorescence detector the average value of X_{max} as a function of energy is known. Application of the selection criteria may reduce the statistics but if the criteria is unbiased the new average value should only reflect the statistical fluctuations and not demonstrate a systematic effect. The target is the elongation rate from [47] and was shown in fig. 5.15. I first reproduce the results using the data obtained from the Auger Observer [64] as a consistency check; applying the selection criteria for fluorescence showers I obtain fig. 7.8. The golden hybrid data is further reduced by applying the selection criteria for each of the surface detector observables changing the average value of X_{max} at each energy as shown in fig. 7.9.

Biases are expected to appear if the selections prefer showers with a particular X_{max}. This is of great concern for the fluorescence detector because all possible X_{max} values are not observable at all geometries [47]. This is not the case for the surface detector where differences in X_{max} primarily lead to fluctuations in ground particle densities. Provided the detector acceptance is saturated, such fluctuations are a non-issue. However selections that require more than the standard three stations or indirectly favor large energy deposits raise the threshold for saturation and possibly reintroduce a bias. The radius of curvature in particular requires many stations before it can be determined, and the strong energy dependence observed in the parameterization of that observable suggests that deeper

shower maxima, and thus higher ground particle densities, could be favored.

With the current statistics for large hybrid showers it is impossible to tell for sure if any of the observables are biased near the threshold, but even if they were the bias would disappear for large showers far from the threshold effects. Just as the accuracy with which the individual observables can be measured increases with the size of the shower, so the biases should decrease. The conclusion is the elongation rate for the highest energies, which is the most interesting and my goal in this analysis, is also the most reliable.

A second line of reasoning is based on the parameterizations from simulations.

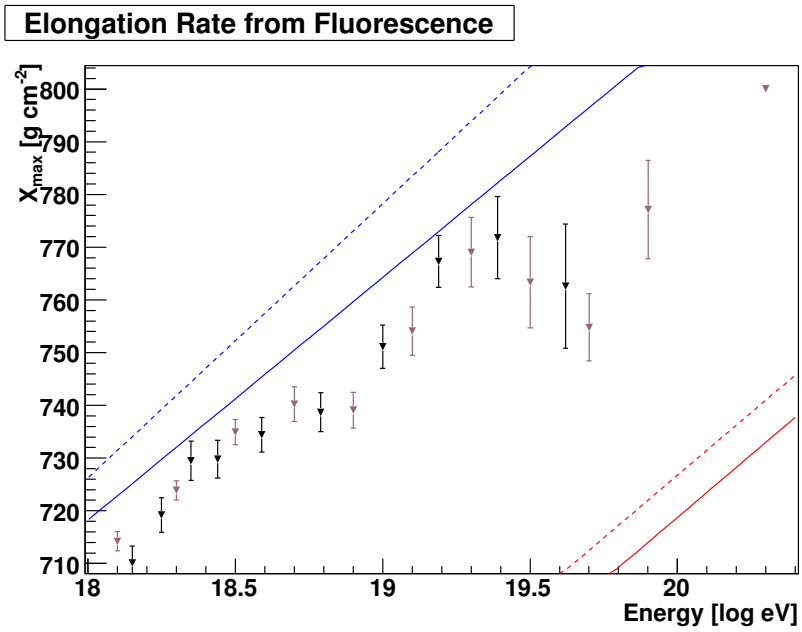

Figure 7.8: The black triangles are the data from [47]. The brown triangles are a reproduction of that data. There are small difference in the average values obtained stemming from unavoidable differences in the data set and binning. The blue (red) lines are the predicted elongation rate for protons (iron). The solid lines are qgsjet, dashed lines are sibyll.

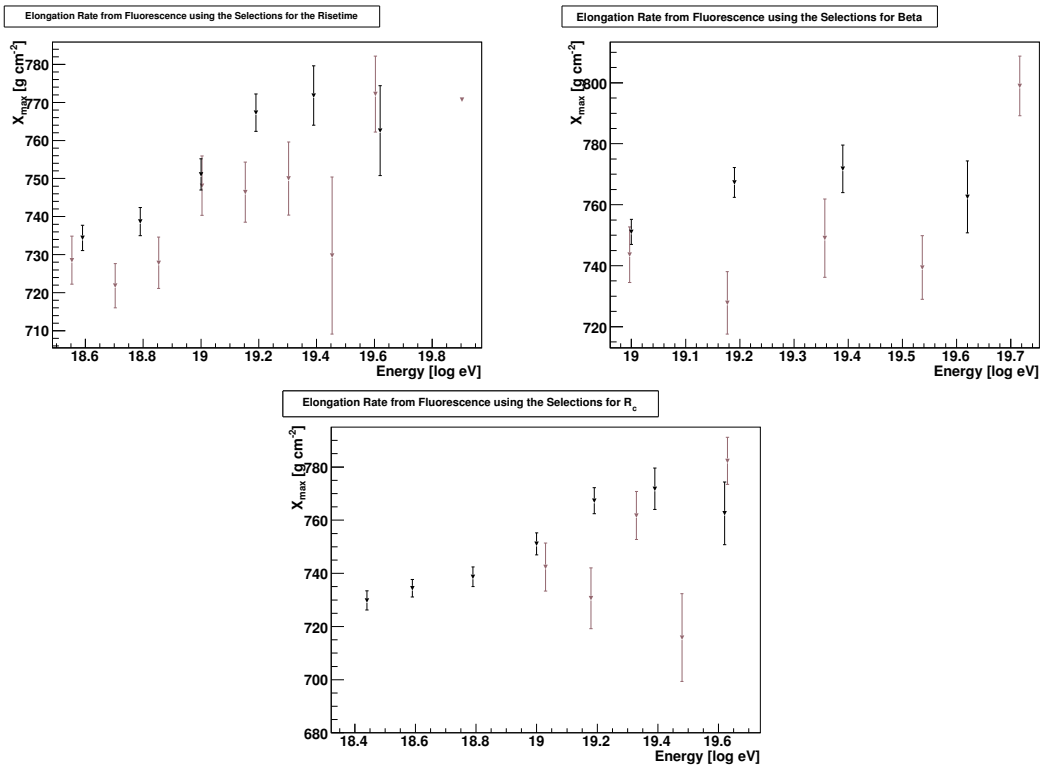

Figure 7.9: The golden hybrid data with the selection criteria for the three surface observables applied. The black triangles are the original data while the brown triangles are the results after the surface detector selection criteria. In general the error bars are compatible between the two sets and a systematic effect does not appear likely. **Top-Left:** The fluorescence elongation rate after the application of the selection criteria for the risetime. **Top-Right:** The fluorescence elongation rate after the application of the selection criteria for beta. **Bottom-Center:** The fluorescence elongation rate after the application of the selection criteria for the radius of curvature.

If a particular X_{max} did not lead to selectable reconstructions of the ground observables those showers would be noticeably absent from the parameterization. In no cases is an artificial absence observed. In fact many of the ground observ-

ables used are reconstructible far beyond the bounds of the selection criteria. The selections are overly tight because of the need to minimize the influence of other shower properties.

7.4 Building the Parameterizations

The risetime, beta, and radius of curvature all have a zenith angle dependence that stems from the evolution of the shower. This is usual and is naturally incorporated into the parameterization if we work as a function of X-X_{max} where X is the depth of the detector in the atmosphere. Fig. 7.10 is a visual description followed by the mathematical formulation in equation 7.4

$$\text{X-X}_{max} = 870.0 \sec\theta - \text{X}_{max} \tag{7.4}$$

The other even larger benefit of working with X-X_{max} is a potential exploitation of the universal nature of shower development. Shower simulations are only as good as the physics they are trying to reproduce. And low energy cascades, of the type that occur after a shower has reached its maximum, are very well understood. The differences in simulations are largely the result of the comparatively poorly understood ultra-energetic interactions that dominate above the shower maximum. If, and this is a big if, the value of the surface detector observables are dependent mostly on the position of the shower maximum, and therefore decoupled from the physics that occurs before that point, it will matter very little which simulation is used.

The risetime is the most universal of the chosen observables so I will illustrate the point using that observable as an example. In fig. 7.11 the risetime is plotted for proton and iron showers using various simulations and each of them is then fit with a quadratic function. The important result is that the functions are

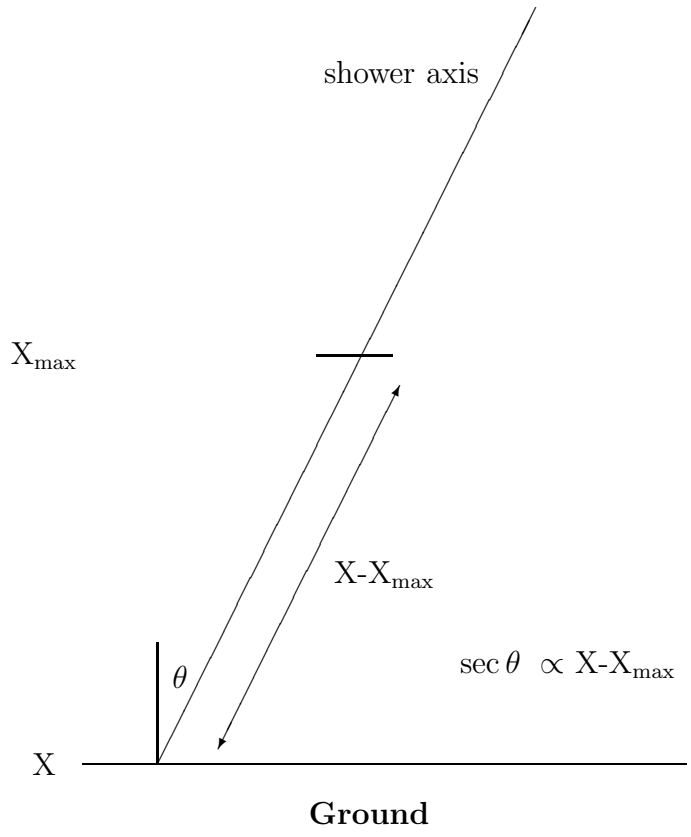

Figure 7.10: The distance through the atmosphere along the shower axis between X and X_{max} is proportional to the zenith angle of the shower. X and X_{max} are atmospheric depths measured from the *top* of the atmosphere.

nearly identical even though the points being fit shift around. The risetime is essentially universal because a change in X_{max}, for instance between proton and iron showers, is accompanied by a change in the risetime such that the simulated data moves along the curve but not off the curve resulting in a function that does not depend on the simulation used to obtain it. Beyond universality the

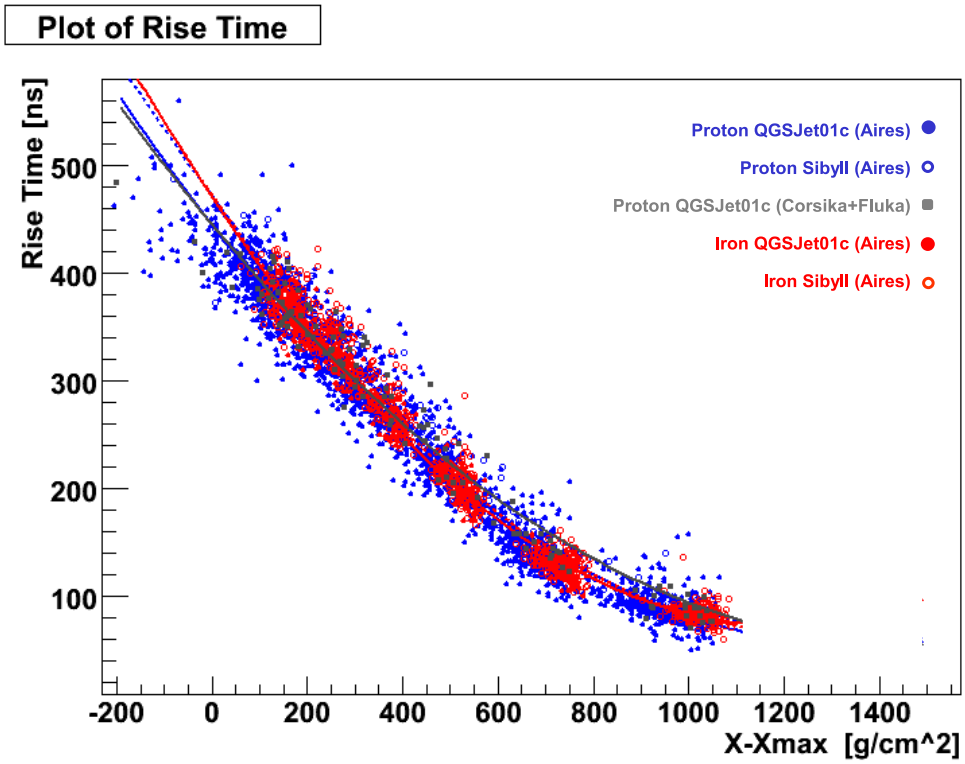

Figure 7.11: The universality of the risetime between different simulations.

risetime is even more special in that simulations predict the functional form is independent of energy as well. This is unique among surface detector observables and a property certainly not shared by either beta or the radius of curvature. The risetime is only effected by the primary energy though the second order process of the primary energies' effect on X_{max} as shown in fig. 7.12. This suggests that the risetime derives purely from X_{max} and does not contain a component from

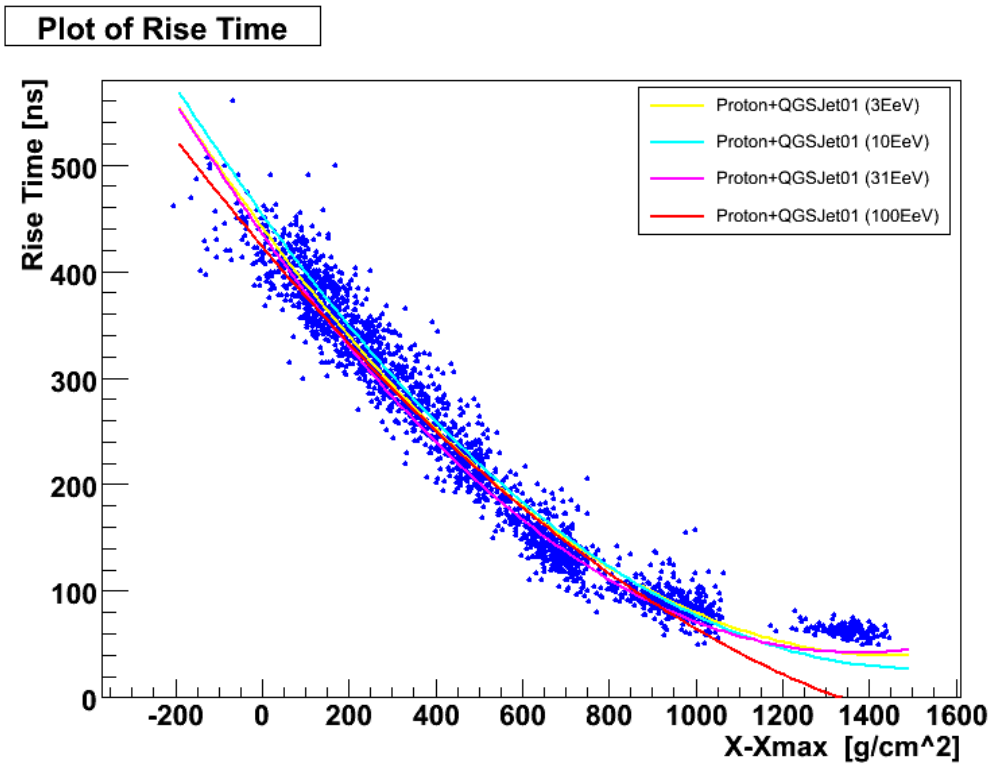

Figure 7.12: The risetime is only effected by X-X_{max}. Even a dependence on the energy of the shower is absent.

either of the two other fundamental shower parameters N_{max} or $\mu_{richness}$[7].

Since the other two observables, beta and the radius of curvature, have a dependence beyond that of X_{max}, the parameterization takes the form of a function that varies with energy. In these cases a linear function is used to describe the relationship between the observable and X-X_{max} where the slope and intercept are different depending on the primary energy. Additionally the functional form of the risetime is well approximated by a linear function over the range of zenith

[7]simulations involving photon showers, which contain almost no muon component, exhibit a modified conversion from risetime to X-X_{max} suggesting that $\mu_{richness}$ does play a role but the differences are below the observable distinction for hadronic primaries

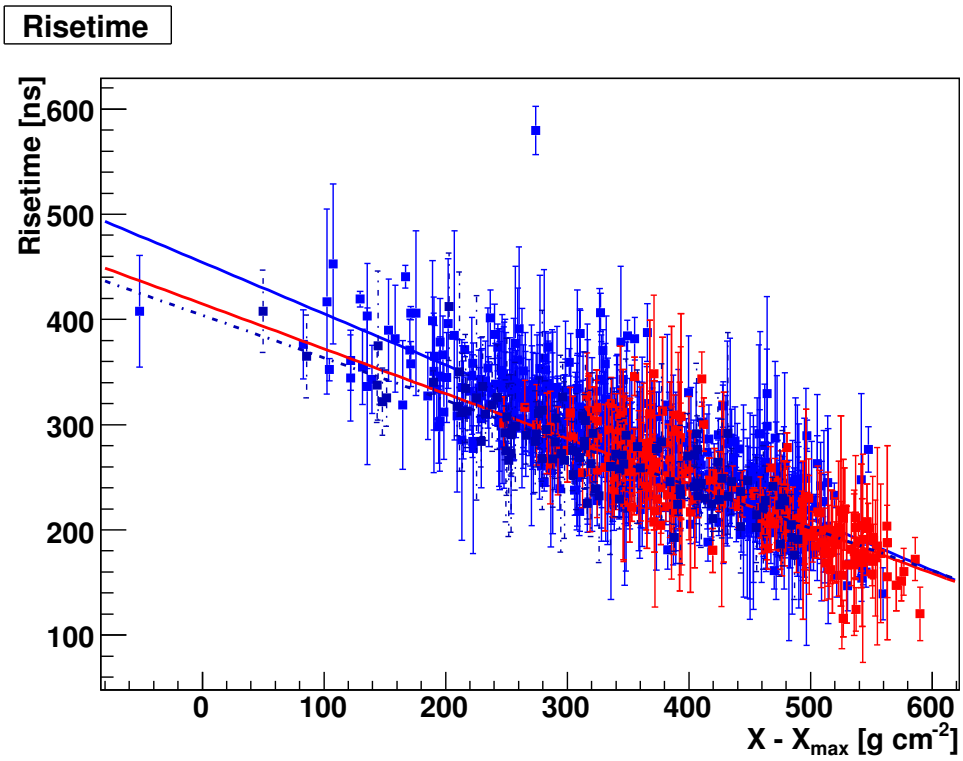

Figure 7.13: The parameterization of the risetime based on three different models. The blue points are proton+qgsjet, the red are iron+qgsjet, and the dashed dark blue are proton+EPOS. Notice how the points tend to shift along the line depending on the shower maximum for the given model but not off the line even though there are other significant differences in the fundamental shower properties between the models.

angles used in the final analysis. The universality of the parameterizations can be seen in fig. 7.13, 7.14, and 7.15.

I will cover a few of the more important selection criteria now that the ideas behind the parameterizations have been introduced. The various angular ranges were determined based on where the sensitivity to X_{max} is achieved. For instance in fig. 7.11 it is clear that at large values of X-X_{max} the risetime does not vary

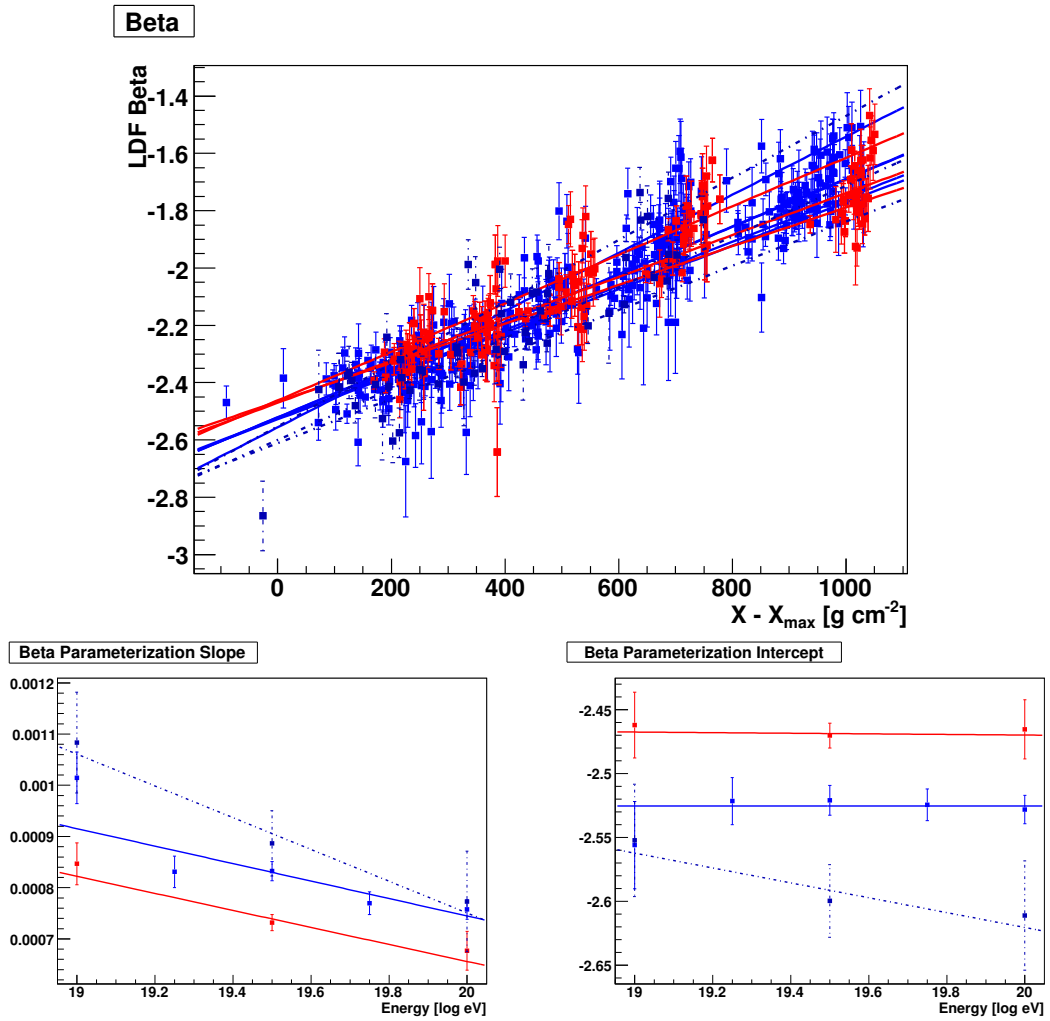

Figure 7.14: The parameterization of beta based on three different models. The blue points are proton+qgsjet, the red are iron+qgsjet, and the dashed dark blue are proton+EPOS. **Top:** Here are linear fits to the data points broken up by energy. Notice in particular how the red and blue points are shifted along the lines but not off the lines. The resulting fits are very similar in slope and intercept. **Bottom-Right:** Taking the slope from each line on top, the change in the slope as a function of energy can be parameterized. **Bottom-Left:** Taking the intercept from each line on top, the change in the intercept as a function of energy can be parameterized.

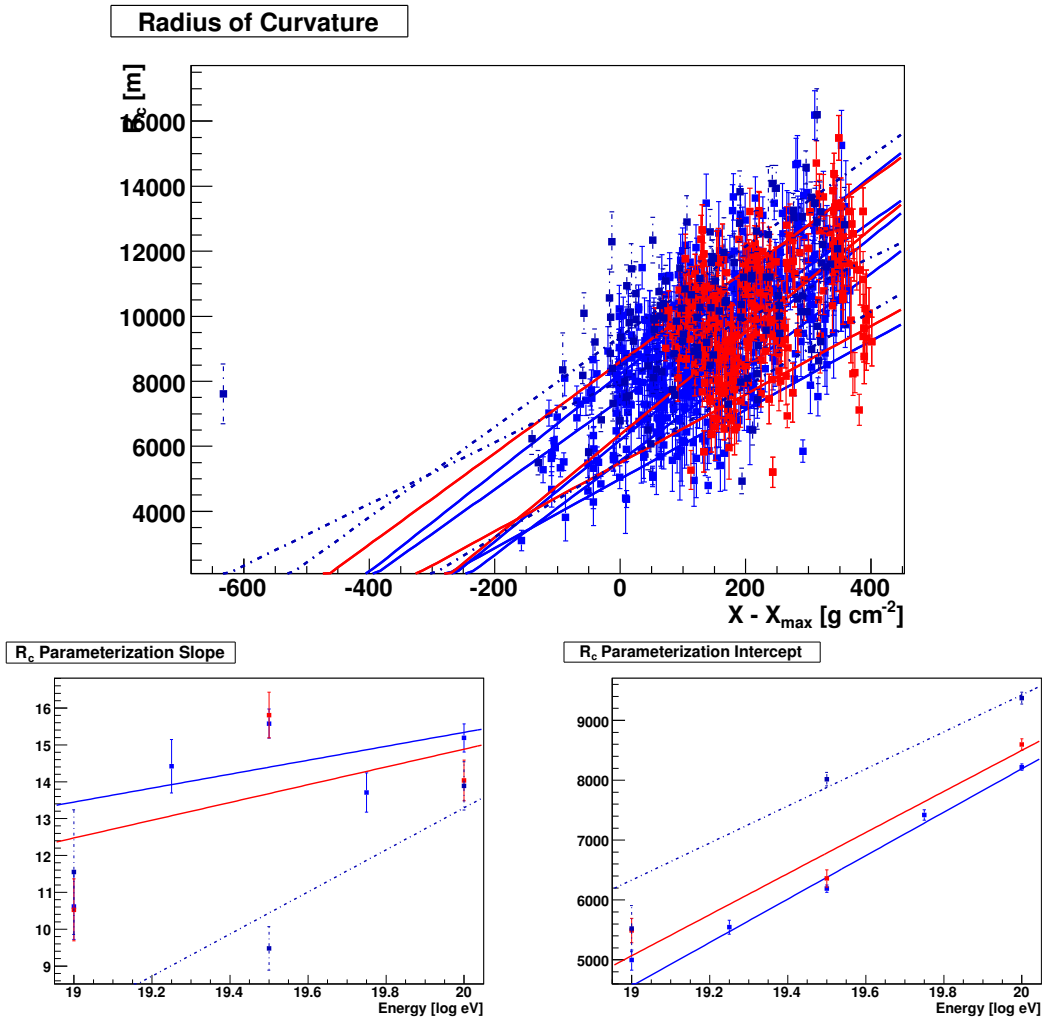

Figure 7.15: The parameterization of the radius of curvature based on three different models. The blue points are proton+qgsjet, the red are iron+qgsjet, and the dashed dark blue are proton+EPOS. **Top:** Here are linear fits to the data points broken up by energy. Notice in particular how the red and blue points are shifted along the lines but not off the lines. The resulting fits are very similar in slope and intercept. **Bottom-Right:** Taking the slope from each line on top, the change in the slope as a function of energy can be parameterized. **Bottom-Left:** Taking the intercept from each line on top, the change in the intercept as a function of energy can be parameterized.

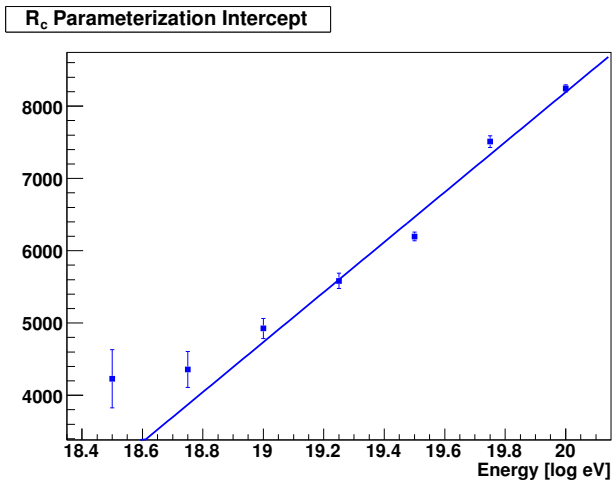

Figure 7.16: The parameterization of the radius of curvature from proton+qgsjet simulations when angles up to 50 degrees and energies down to 3 EeV are allowed. Notice the departure from the parameterized behavior.

much anymore. These are inclined showers so attenuated that there is nothing but muons left and the influence of X_{max} is almost gone. Similarly the radius of curvature is only used above 9 EeV and at a zenith angle of less than 40 degrees because as fig. 7.16 shows the radius of curvature deviates from the linear parameterization used if the selection is made looser. The explanation is two fold: (1) the radius of curvature requires at least five stations to fit and can be hard to calculate accurately at low energy and (2) a hemisphere model is used for the radius of curvature. The hemisphere model implicitly implies that all particles originate at a single point spreading out from there. How much they have spread out depends on how long the shower has been developing. For a near vertical shower, the leadinging edge of particles intersect the ground with a single radius of curvature, but in the case of an inclined shower the stations on the far side of the axis are much further away from the first interaction and the radius of curvature is not uniform across the array. The radius of curvature from inclinded

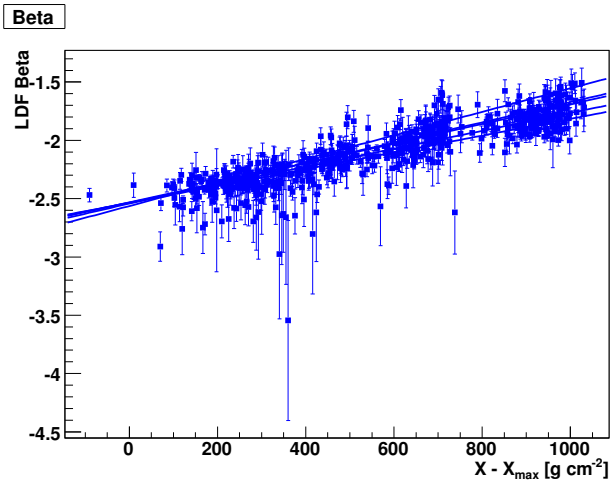

Figure 7.17: The scatter plot of beta as a function of X-X_{max} from proton+qgsjet simulations when saturated events are allowed. A distinct tail to larger negative values appears. Compare this figure to fig. 7.19 which uses the cut on saturation.

showers does not contain much information about X_{max}, it has more to do with shower asymmetries.

The selections for beta require a good reduced chi square for the lateral distribution function and that none of the stations in the event be saturated. Both criteria are designed to eliminate a tail in the reconstruction of beta. Unfortunately the second condition makes beta less useful at higher energies where most events contain a saturated station. In fig. 7.17 saturated events are allowed and a noticeable tail to large negative values of beta appears. While these are a minority, the values are so different from the unbiased reconstructions that they lead to an X-X_{max} of several thousand. The net effect is a skew in the average estimated X_{max} for any energy bins containing a saturated event.

The selection criteria for each variable were developed to keep the simulations consistent with the parameterizations used and the estimated X-X_{max} consistent

with the proton+qgsjet monte-carlo.

7.5 Composition Results

The proton and qgsjet model is useful because it is a proxy for the average of all the currently available models. Not only is the muon content between the extremes but the shower maximum is as well, and for these reasons I have chosen it as the standard for this analysis despite the fact that it does not reproduce some of the bulk properties of Pierre Auger data as discussed in chapter 6.

To begin with the parameterization of the conversions based on the proton+qgsjet combination are formed. These are shown in fig. 7.18, 7.19, and 7.20.

Each parameterization is built after the application of the selection criteria for that observable. Those parameterizations are then applied to the real data converting the risetime, beta, and radius of curvature to X-X_{max} separately depending on the selection criteria each event satisfies. In many cases this leads to three distinct estimates of X-X_{max} for the event although the differences in selection criteria do not guarantee that. X_{max} alone is obtained by subtraction of X using equation 7.4 and the reconstructed zenith angle.

The derived value of X_{max} can then be compared to the measured value of X_{max} for the set of golden hybrid showers. The comparison is useful because it is an estimation of the correlation between the converted X_{max} and the more reliable measurement of the fluorescence detector. It is also a way to evalutate any systematic offset due to the reliance on shower simulations. A scatter plot of the surface detector X_{max} versus the fluorescence detector X_{max} is plotted and fit with a straight line allowing the intercept to float.

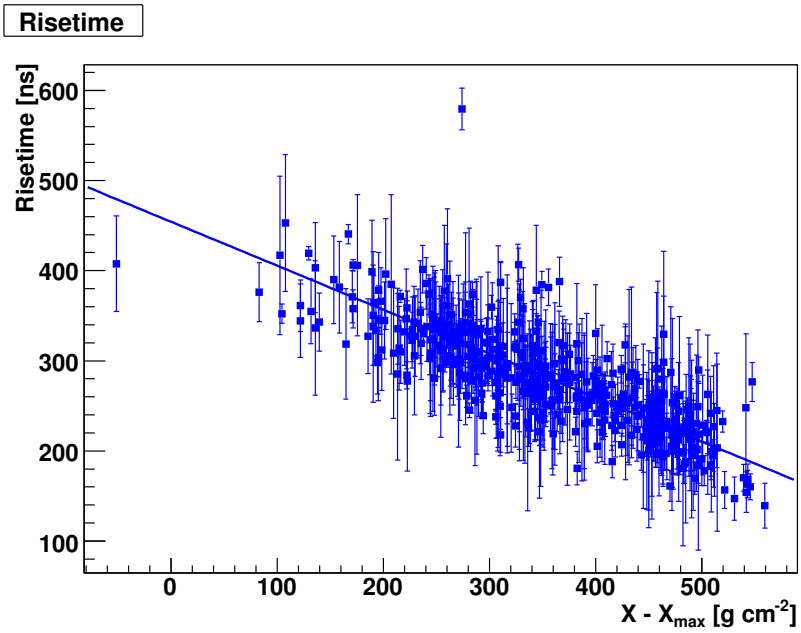

Figure 7.18: The parameterization of the risetime based on proton+qgsjet model. This parameterization is used to derive X-X_{max} from showers detected with the surface array.

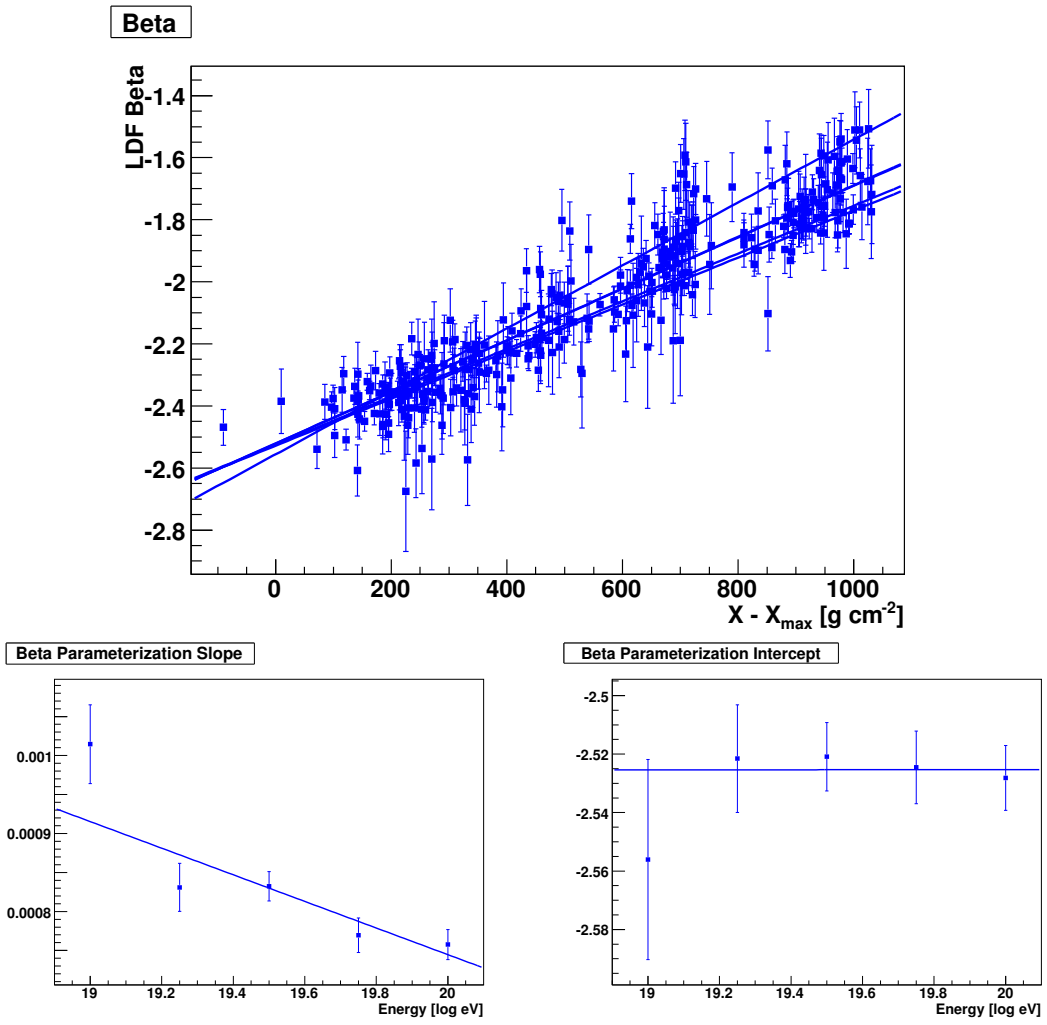

Figure 7.19: The parameterization of beta based on proton+qgsjet model. This parameterization is used to derive X-X_{max} from showers detected with the surface array.

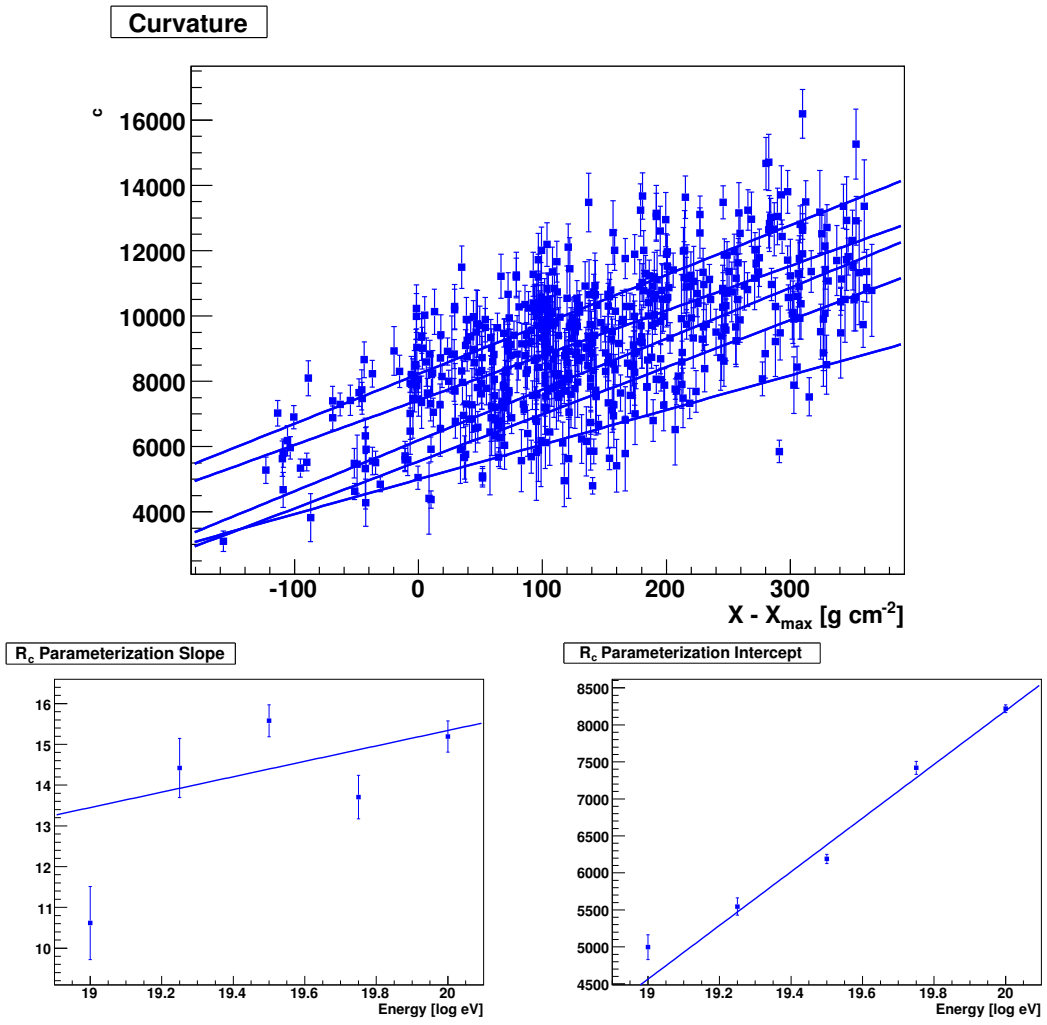

Figure 7.20: The parameterization of the radius of curvature based on proton+qgsjet model. This parameterization is used to derive X-X_{max} from showers detected with the surface array.

Using the fit it is clear that X_{max} from the surface detector is only weakly correlated (see table 7.2) with the target value from the fluorescence detector as seen in fig. 7.21. This is expected because the variance in the surface detector X_{max} should be larger than the fluorescence detector measurement. The overall agreement is good and it is clear that the two X_{max} are related regardless of which surface detector observable is used to estimate it.

It is possible to derive a systematic correction if it is assumed that the linear fit is an accurate representation of the relationship between the two measurements of X_{max}. The intercept of the fit is a constant offset in estimated X_{max}, while the slope of the line is an offset of constant proportion. Naturally, if each surface detector X_{max} is modified by the fit (see equation 7.5), it brings the fluorescence detector X_{max} into perfect agreement for the golden hybrid data as shown in fig. 7.22 for the risetime.

$$X_{max-corrected} = \frac{X_{max-SD} - \text{intercept}}{\text{slope}} \tag{7.5}$$

The possibility of applying the same correction to every event, golden hybrid or not, was investigated and found mixed results. When using beta to derive the elongation rate from the surface detector, the agreement with the fluorescence detector elongation rate was improved, however, the situation was reversed when using the radius of curvature. In the case of the risetime, the elongation rate was largely unaffected with a maximum change of less than 10% in the average X_{max} at any energy.

Despite the potential for calibrating the X_{max} found from the surface detector using simulations, the correction above was not made in the final analysis. The reasons for not doing it are, given the limited statistics, it may be premature to assume the linear relationship between the X_{max}s and it still remains to be seen if the fluorescence detector systematic uncertainty is truly zero.

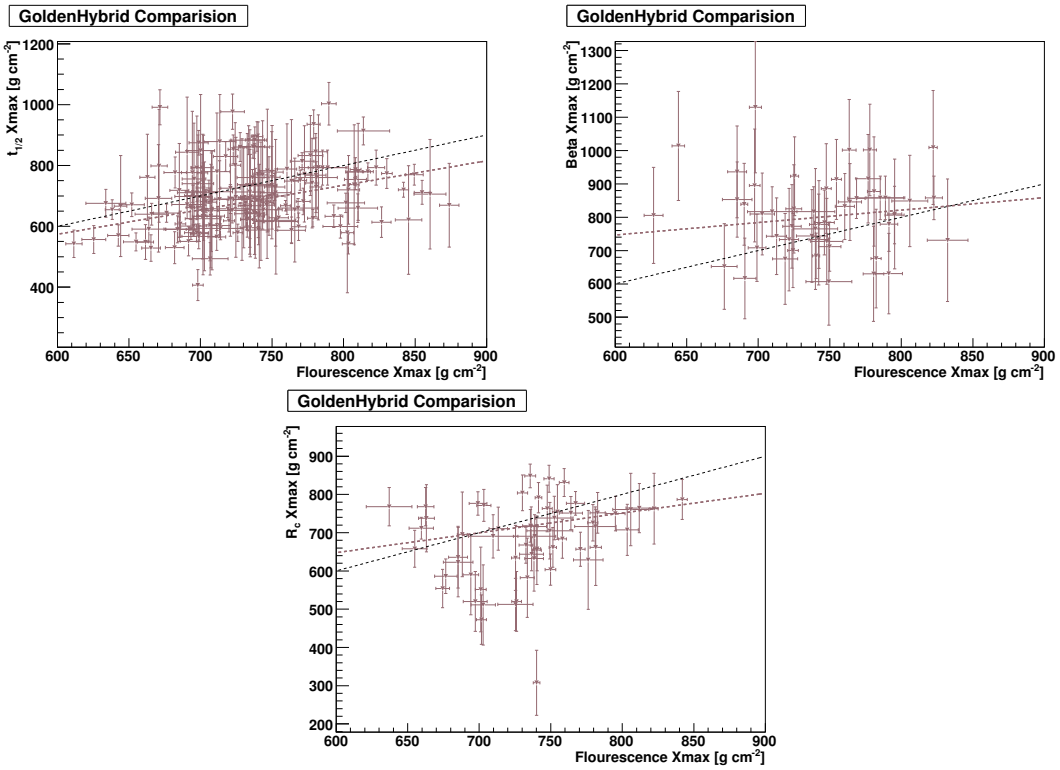

Figure 7.21: Using the set of golden hybrid showers X_{max} derived from the surface detector using the risetime (**Top-Left**), beta (**Top-Right**), and radius of curvature (**Bottom-Center**) can be compared to that measured by the fluorescence detector. The dashed black line is a line of slope one, while the dashed brown line is a fit to the data. The slope of the brown line is determined by how well the data are correlated.

	Table of Correlation Strength		
	Risetime	Beta	R_c
Slope of Best Fit	1.02	0.374	0.517
Intcpt. of Best Fit	-57.7	522.	337.

Table 7.2: Each parameterization allows an estimate of X_{max} on an event-by-event basis. Comparing these estimates to the measured values for golden hybrid showers is useful for obtaining the strength of the correlation.

With an estimate of X_{max} in hand and the confidence supplied by the golden hybrid data the elongation rate can be derived. In this final step a weighted average of X_{max} is created for bins in the logarithm of the shower energy. The weighting is done according to the error bar of each X_{max} such that those with the smallest error bars count more. Since there are three separate estimates of X_{max} it is possible to create three separate elongation rates seen in fig. 7.23, 7.24, and 7.25. In the elongation rate plots the blue lines are always proton and the red lines are always iron. The solid lines are from the qgsjet model while the dashed are the sibyll model.

Up to this point everything has been based on proton+qgsjet simulations and we know those simulations contain inconsistencies when compared to measured data. It is interesting to see how the results change if a different parameterization is used, in particular the newest EPOS [57] model that contains the most advanced hadronic simulations available in the ultra-relativistic regime. The resultant elongation rates are shown in fig. 7.26, 7.27, and 7.28. These alternate

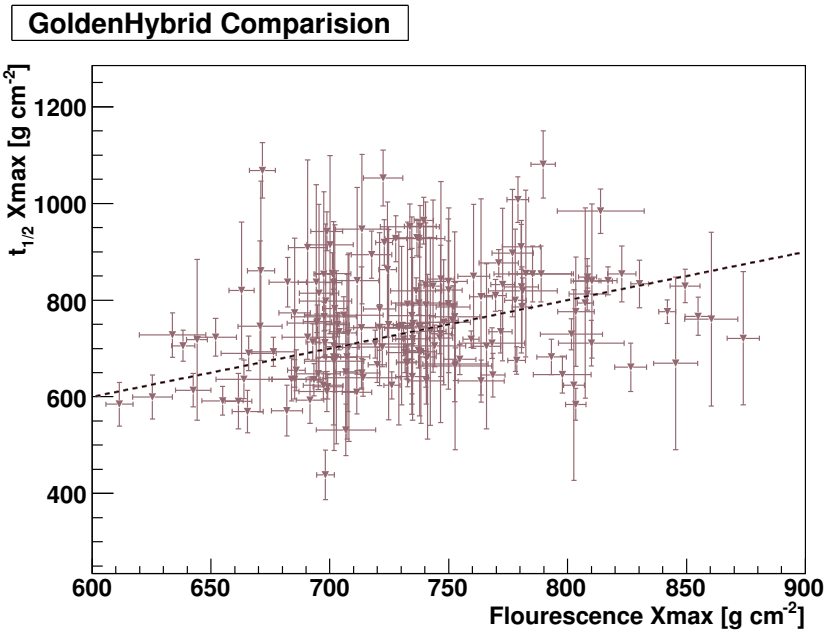

Figure 7.22: X_{max} from the risetime after correcting for the offset using equation. 7.5. A new fit, the dashed brown line, is now right on top of the dashed black line.

elongation rates also allow an estimate of the systematic uncertainties stemming from the use of a particular simulation to derive the elongation rate from the surface detector.

7.6 Discussion

An estimate of X_{max} from the surface detector is an important step on the road to understanding ultra-high energy cosmic rays. The key to its development has rested on two pillars.

- Cosmic ray air showers can be described accurately in terms of three fundamental parameters N_{max}, X_{max}, and the $\mu_{richness}$

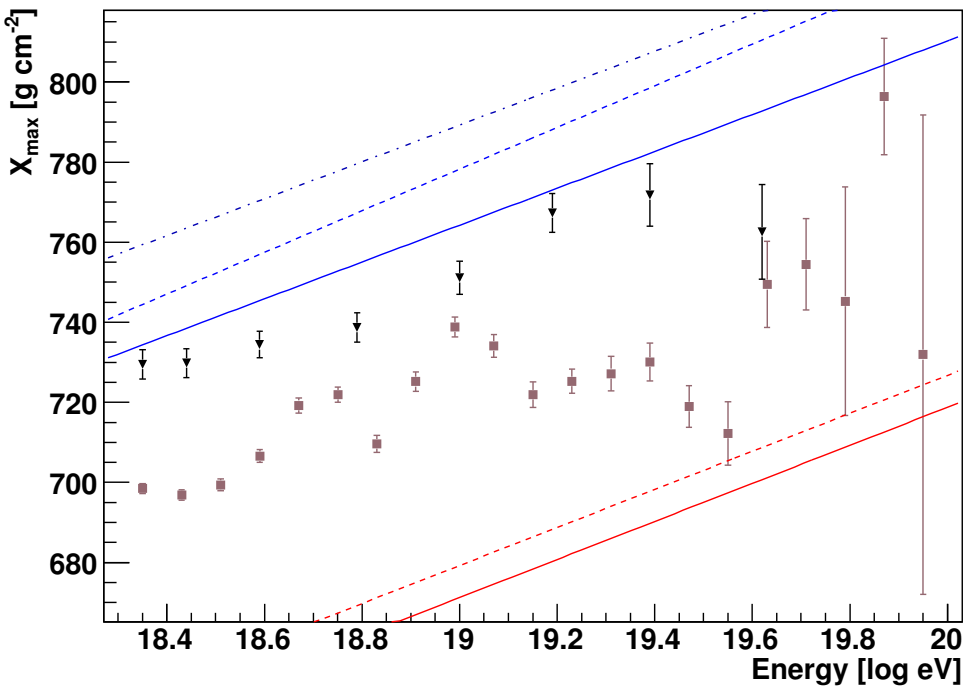

Figure 7.23: Risetime elongation rate using the proton+qgsjet model. The lines represent model predictions. The higher ones are protons in blue, the lower are iron in red. The solid lines use the qgsjet model, while the dashed are sibyll, and the dot-dashed are epos.

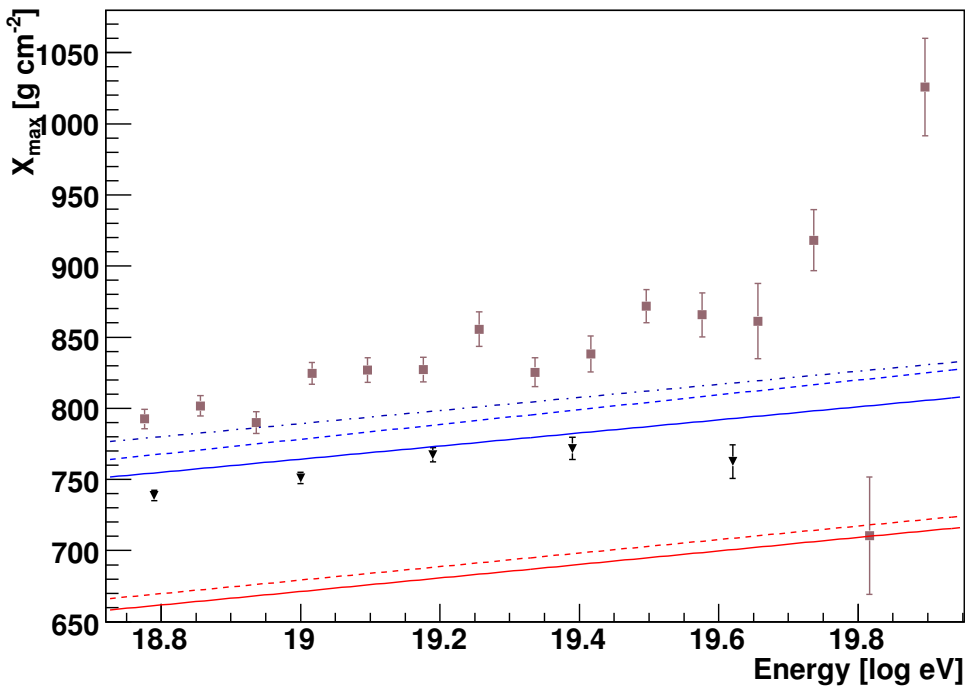

Figure 7.24: Beta elongation rate using the proton+qgsjet model. The lines represent model predictions. The higher ones are protons in blue, the lower are iron in red. The solid lines use the qgsjet model, while the dashed are sibyll, and the dot-dashed are epos.

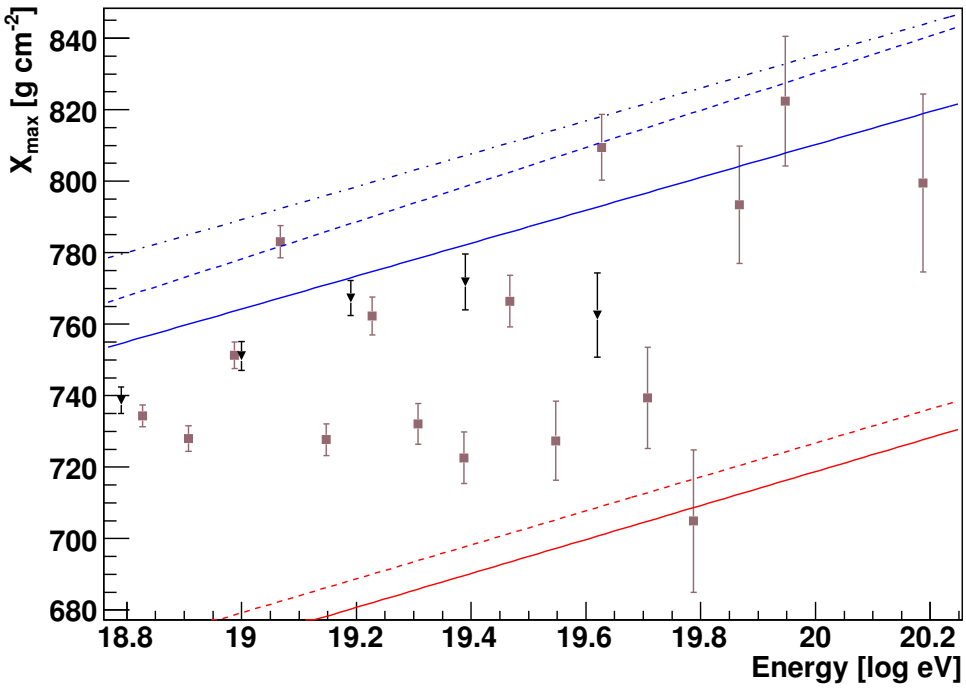

Figure 7.25: Radius of curvature elongation rate using the proton+qgsjet model. The lines represent model predictions. The higher ones are protons in blue, the lower are iron in red. The solid lines use the qgsjet model, while the dashed are sibyll, and the dot-dashed are epos.

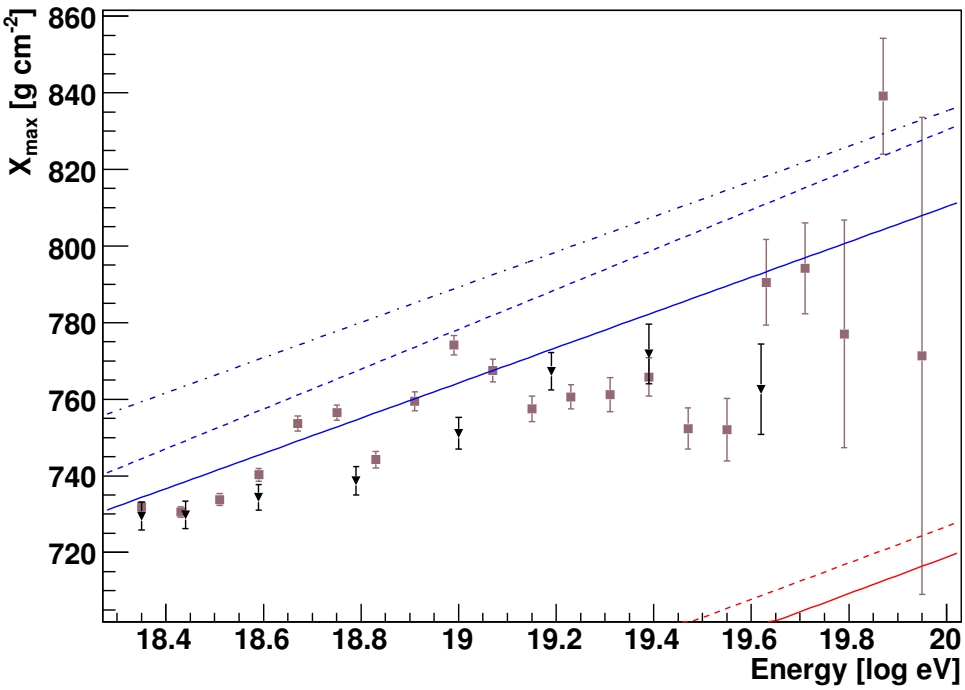

Figure 7.26: Risetime elongation rate using the epos hadronic interaction model. The lines represent model predictions. The higher ones are protons in blue, the lower are iron in red. The solid lines use the qgsjet model, while the dashed are sibyll, and the dot-dashed are epos.

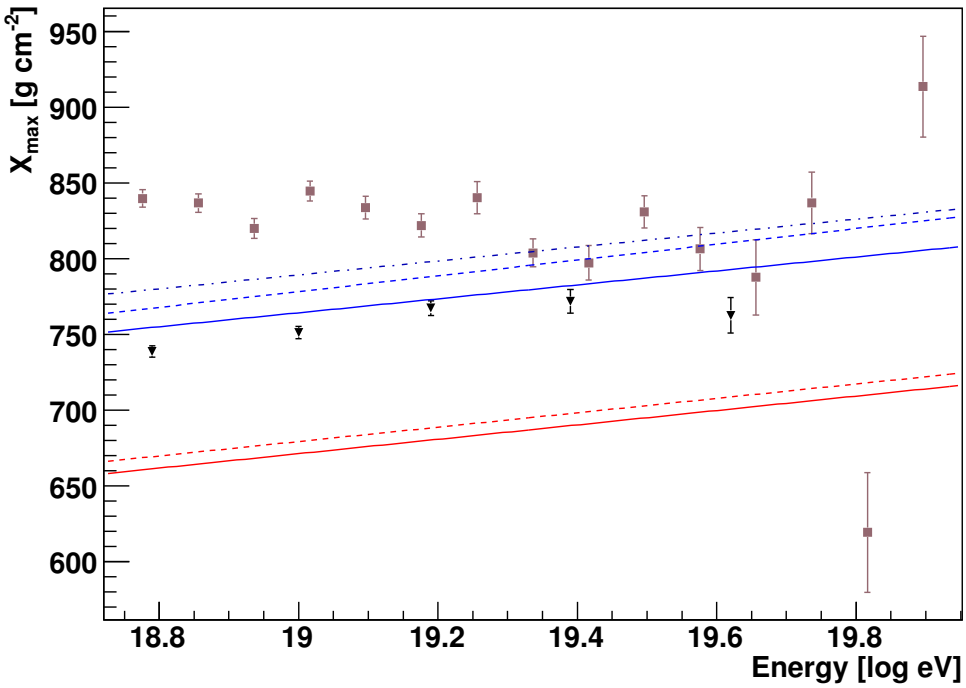

Figure 7.27: Beta elongation rate using the epos hadronic interaction model. The lines represent model predictions. The higher ones are protons in blue, the lower are iron in red. The solid lines use the qgsjet model, while the dashed are sibyll, and the dot-dashed are epos.

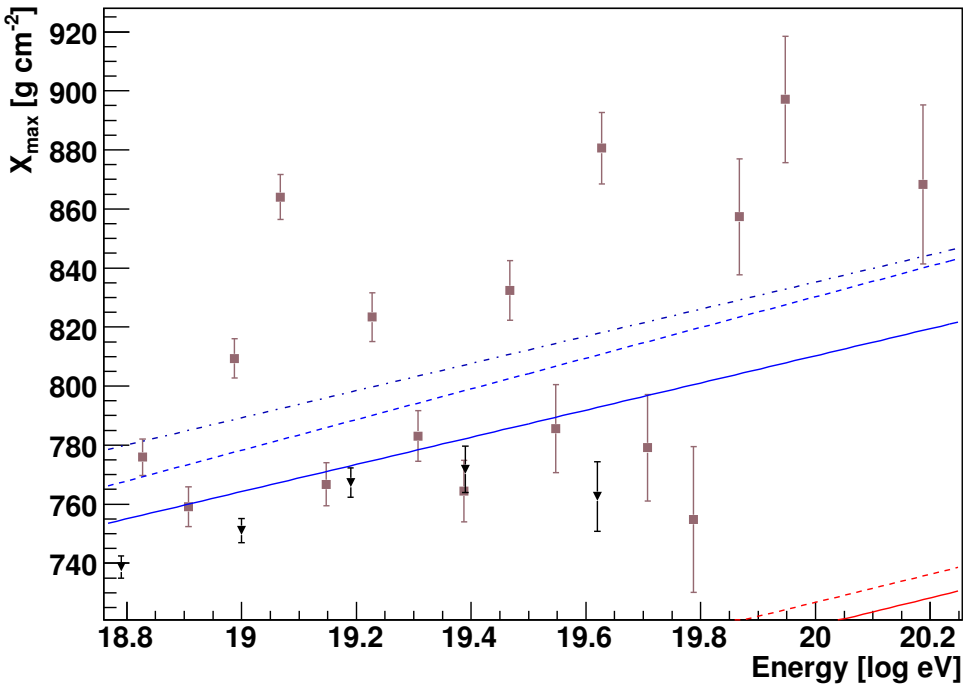

Figure 7.28: Radius of curvature elongation rate using the epos hadronic interaction model. The lines represent model predictions. The higher ones are protons in blue, the lower are iron in red. The solid lines use the qgsjet model, while the dashed are sibyll, and the dot-dashed are epos.

- Shower development is universal once the three fundamental parameters are specified allowing a parameterization from simulation that minimizes the absolute differences

The second point can not be stressed enough. It is a mistake to think universality has to do with commonalities between simulations, it doesn't. I like to think of universality as a property of statistical mechanics. An air shower contains so many particles that once a few critical initial conditions are set the ultimate outcome is a forgone conclusion.

Universality is useful because every combination of shower simulation, hadronic interaction model, and primary assumption predicts an unique average X_{max} and the corresponding surface detector observables. Without universality it would be impossible to know which simulation best represented a real cosmic ray shower[8] and the surface detector could not obtain a prediction of the composition with any reliability. That was the short-fall of the results from section 5.3.3; simulations could not reproduce the observed data in a consistent manner. Universality does not require a simulation be correct in every respect, just that the fundamental parameters (those critical initial conditions) inevitably specify the ground observables.

Demonstrating that all simulations share the same relationship between fundamental parameters and ground observables is a good test of assumed universality and was the first step in this analysis. Having accomplished that, the second step was an identification of which events are well constrained enough that variances in X_{max} are visible. The parameterizations are built assuming universality and then applied to real data. It is essential that the measurement uncertainty of

[8]In fact it has been stated by critics that **none** of the simulations may accurately represent a real cosmic ray shower

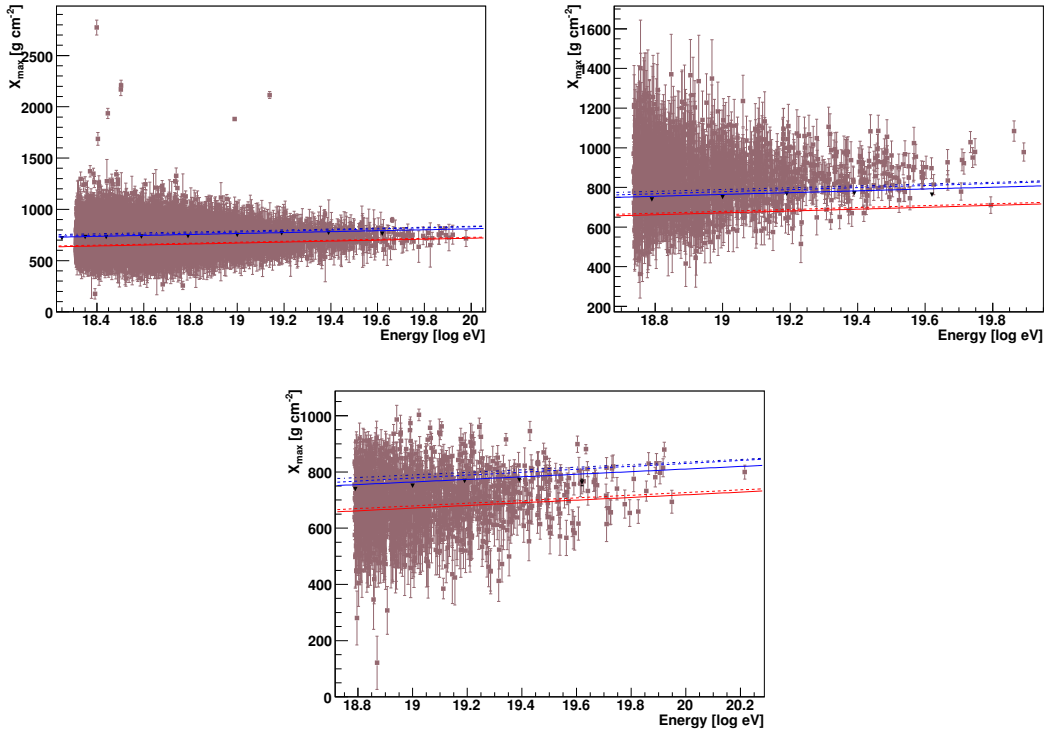

Figure 7.29: The event-by-event X_{max} as estimated from the surface detector observables. The conversion was done using the proton+qgsjet model. **Top-Left:** The estimated X_{max} from the risetime. **Top-Right:** The estimated X_{max} from beta. **Bottom-Center:** The estimated X_{max} from the radius of curvature.

the surface detector observables be propagated through the conversion process so the variance introduced by the detector can be properly weighted when forming the average value of X_{max}. Fig. 7.29 is the scatter plot of the event-by-event estimates of X_{max} prior to the weighting procedure.

Risetime is the most universal of the three ground parameters investigated and therefore I believe it provides the best measurement of the elongation rate. The risetime selection criteria are the loosest of the three and the sensitivity to X_{max} is the greatest. Both beta and the radius of curvature are more difficult to

work with. The energy dependence (really N_{max}) is strong and I believe the muon component plays a larger role for those two observables, something I have largely neglected. The elongation rate from the EPOS model demonstrates how beta and the radius of curvature are still sensitive to the model assumptions, especially at low energy (see fig. 7.27 and fig. 7.28) while the risetime universality is nearly unbroken as seen in fig. 7.26 and fig. 7.13.

The presence of a mixed composition at the highest energies is established by the non-linearity of the elongation rate. All models of constant composition are straight lines while the data is exhibiting structure. The consequence of structure is an energy dependent composition that moves to include some heavier elements above $10^{19.2}$ eV; elements that are nearly absent around 10^{19} eV. A mixed composition at the highest energies was not widely "expected" in the community.

CHAPTER 8

Conclusion

Determining the origin of ultra-high energy cosmic rays is a difficult task and a comprehensive theory will need to explain all observed results. An elongation rate that predicts cosmic rays are a mixture of nuclei at the highest energy is an important constraint on the development of acceleration models. Theories involving cosmic envirnoments of high energy density, that initially seem favorable because we are talking about ultra-high energy cosmic rays after all, will have difficulty explaining how a nucleus can survive.

Additionally correlation signals, some of which the Pierre Auger Observatory is currently testing, need to be evaluated carefully in the context of a mixed composition. Heavier nuclei contain more protons so they are effected by magnetic bending to a greater degree. Does this mean any correlation should only come from protons? Not necessarily but it must be a concern. Additionally the GZK sphere is a bit different for heavier nuclei and the mechanism for suppression at the highest energies is dominated by photo-disintegration, not delta production. The effects on the spectrum shape can be seen in fig. 8.1 where the Pierre Auger spectrum has been fit with two theories one where all cosmic rays are initially protons, and one that assumes all cosmic rays are initially iron nuclei. These models constitute the limiting cases.

The Pierre Auger group at the University of California, Los Angeles and myself specifically were the first ones to push the idea that our data indicated

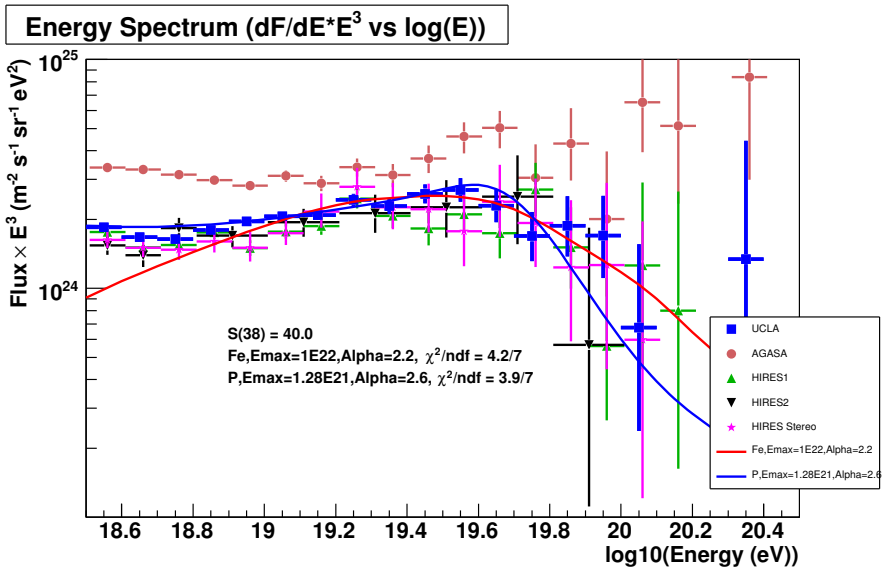

Figure 8.1: The Pierre Auger Spectrum with two theoretical predictions of the flux observed at Earth. One assumes sources that produce only proton cosmic rays, the other only iron cosmic rays. There are differeences in the shape of the spectrum as well as the suppression above the GZK energy.

a mixed composition at the higher energies. Our confidence was based on the risetime analysis of section 5.3.3. The risetime was always the better surface observable in my mind and while the absolute value indicated iron that was not the most convincing evidence because we knew there were problems with the computer simulations. In particular the results from the study I did in chapter 6 were already known and our favorite explanation for the discrepancy between the attenuation curve from simulations compared to that from real data was a systematic lack of muons in the simulations. A change in the muon content could bring the attenuation curves into agreement and it would likely speed up the simulated risetime to allow a proton like composition around 10 EeV. What it could never do was explain the evolution of risetime with energy. A linear fit to the risetime data was too flat for a constant composition regardless of the absolute value. Results based purely on simulations though were never going to convince the community at large so it became necessary to convert to a variable that was directly measured so the simulated results could be verified. That need led to the analysis in the previous chapter.

I am positive that cosmic rays are a mixed composition at the highest energies. Our initial bet that the simulations were missing muons has proven to be correct as seen in fig. 8.2. From the same study of atmospheric attenuation curves we also concluded our data was at best only marginally in agreement with the energy scale from the fluorescence detector. Fig. 8.2 confirmed that conclusion as well. Our findings that indicated a mixed composition of hadrons at the highest energies is also proven correct.

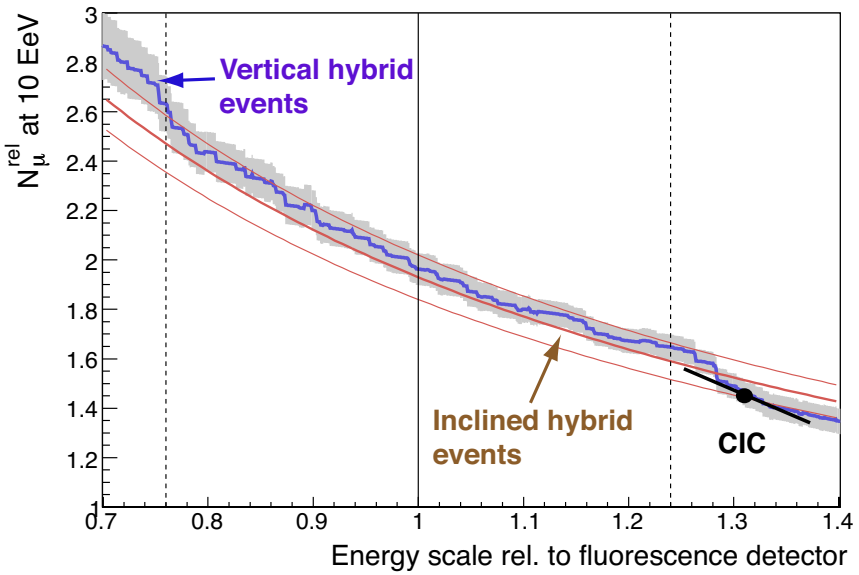

Figure 8.2: Combining several analysis techniques the Pierre Auger data can be used to set a muon content relative to proton+qgsjetII showers. The data also lead to a new calibration of the surface detector energy scale. The convergence of the three method are a boost to the simulated muon content by a factor of 1.4 and a surface detector energy 1.3 times the value used by the collaboration thus far.

APPENDIX A

FADCPulseParametersUCLA

This appendix covers the FADCPulseParametersUCLA that serves as a major building block for composition analysis. The module was developed mainly by M.D.Healy and calculates the risetime of a surface detector event. Typically the risetime is the time, in nanoseconds, that it takes for the integral signal to increase from 10 to 50% of its total value often called $t_{1/2}$ in this context, although this is a configurable option.

A.1 Module Design

FADCPulseParametersUCLA is a reconstruction module and relies on a core position, zenith angle, S(1000) value, and the individual station signals to function. A number of Pierre Auger Collaboration members contributed to the theoretical development through supporting analyzes and the development of a consistently stable method for obtaining results [41, 65].

A.2 Full Source Code

The module FADCPulseParametersUCLA was first submitted to the offline svn[1] [66] on February 20, 2007. The source code that follows is a record of the module as it was for the analysis in this work. The same version can be obtained from the offline svn as revision number 5636. Access to the code repository is obtained at https://www.auger.unam.mx/AugerWiki/OfflineSoftware/ and is password protected.

Reflecting the release of the software to the collaboration the name was changed in April 2007 to Risetime1000LLL so as to better describe the task performed by the module as well as credit the groups involved in the theoretical development. This was revision 5921.

FADCPulseParametersUCLA.h

```
// File "FADCPulseParametersUCLA.h"
//
// This module calculates the risetime for an event.  Typically this
// is a value interpolated from a fit to the individual risetimes of
// each candidate station in the shower plane.  An option to
// recalculate the risetime of each station is provided.
//
// Author:    M. Healy, D.Barnhill
// Created:   Sep 27, 2004
// Modified:  Jan 17, 2007
//*****************************************************************

#ifndef _FADCPulseParametersUCLA_h
#define _FADCPulseParametersUCLA_h

// Offline headers
#include <fwk/VModule.h>
```

[1] *svn* stands for sub-version; it is a code versioning system similar to *cvs* and is principally designed to allow the development of software by multiple programmers while providing a record of changes as well as resolving conflicting code

```
#include <evt/Event.h>
#include <sevt/Station.h>

// ROOT headers
#include <TGraphErrors.h>
#include <TF1.h>

// Standard c++ headers
#include <vector>

namespace FADCPulseParameters{

/**
   \class FADCPulseParameters

   \brief This module calculates the risetime for an event.

   Typically this is a value interpolated from a fit to the individual risetimes of
   each candidate station in the shower plane.  An option to
   recalculate the risetime of each station is provided.

   \author  M. Healy
   \author  D. Barnhill
   \date    27 September 2004
   \version   $Id:$
   \ingroup SDRecModules
*/


  struct StationRisetimeDataUCLA
  {
    unsigned int fStationId;
    double fRisetime;
    double fRisetimeError;
    double fDistance;
    double fDistanceError;
    unsigned short fRejectCode;
  };

  struct RisetimeResultsUCLA
  {
    RisetimeResultsUCLA();
    ~RisetimeResultsUCLA();
```

```
  std::vector<StationRisetimeDataUCLA*> fStationData;
  double fFitPar0;
  double fFitPar1;
  double fRisetime;
  double fRisetimeError;
  double fRisetimeChi2;
  double fRisetimeNDF;
  double fXmax;
  double fXmaxErrorUp;
  double fXmaxErrorDown;
};

class FADCPulseParametersUCLA : public fwk::VModule
  {
  public:

    FADCPulseParametersUCLA();
    virtual ~FADCPulseParametersUCLA();

    // Init, Run, and Finish functions
    fwk::VModule::ResultFlag Init(void);
    fwk::VModule::ResultFlag Run(evt::Event &theEvent);
    fwk::VModule::ResultFlag Finish(void);

    // Static public members for access outside this module
    static double Risetime;
    static double RisetimeError;
    static double RisetimeReducedChi2;
    static RisetimeResultsUCLA* RisetimeResults;

  protected:

    // Variables read from the xml file to configure the
    // risetime recalculation (if used)
    float RiseTime_StartPercent;
    float RiseTime_StopPercent;

  private:

    // Calculate the Risetime and return that value
    double FitEventRiseTime();
    double RecalculateRiseTime(sevt::Station &theStation);

    // Variables used for the riestime fit
```

```
    TGraphErrors *RiseTimeGraph;
    TFormula *RTWeights;
    unsigned int fRejectedStations;

    // Variables read from the xml file to configure the risetime routines
    float MinimumSignalForRiseTimeFit;    //Signal size in VEM
    float MinimumDistanceForRiseTimeFit;  //Distance in meters
    float MaximumDistanceForRiseTimeFit;  //Distance in meters
    float DistanceToInterpolateFitResult; //Distance in meters to evaluate the fit at
    bool IncludeSaturatedForRiseTimeFit;  //True or False
    bool DoRiseTimeFit;
    bool ForceRiseTimeRecalculation;      //Don't trust others to calculate it
    char *RTWeightingFunction;            //Function describing the
                                          //weight as a function of
                                          //distance/signal size

    REGISTER_MODULE("FADCPulseParametersUCLA",
FADCPulseParametersUCLA);

  };
}

#endif
```

FADCPulseParametersUCLA.cc

```
// File "FADCPulseParametersUCLA.cc"
//
// This module calculates the risetime for an event.  Typically this
// is a value interpolated from a fit to the individual risetimes of
// each candidate station in the shower plane.  An option to
// recalculate the risetime of each station is provided.
//
// D.Barnhill (August 10, 2005)
// Taking M. Healy's original code and modifying a few things to make
// it more simple and reliable
//
// M.Healy (Sep 18, 2006): Further modifing the code to allow the
// error parameterization from leeds.  Also commenting out the linear
// fit for risetime to eliminate events that are on the cusp in terms
// of quality.
//
// M.Healy (Oct 9, 2006): Export the chi2 of the risetime fit for
```

```
// collection by subsiquent modules.
//
// M.Healy (Nov 21, 2006): Fixed a bug related to the inclusion of
// non-canidate stations from the event selection.
//
// M.Healy (Nov 29, 2006): Major upgrade to eliminate vestigial code
// and bring the module up to distribution quality standards. Version
// to be submitted to the offline SVN shortly.
//
// M.Healy (Dec 1, 2006): Used the major upgrade to add functionality
// that will interface with the ADST produced by Karlsruhe. This will
// allow browsing the fit results in the ADST viewer.
//
// M.Healy (Dec 14, 2006): Bug fixes, and changes to compile with
// version v2r2p3 of the offline.
//
// M.Healy (Jan 8, 2007): Strip out code to call RecShower->GetZenith()
// because it is not implimented. Reverted to old method for getting
// the shower zenith angle.
//
// M.Healy (Jan 17, 2007): Eliminated the streaming of the TF1 object
// in the fit results. This was not working with the ADST writer so
// resorted to the use of two doubles.
//
// Author:    M.D.Healy, D.Barnhill
// Created:   Sep 24, 2004
// Modified:  Jan 17, 2007
//**********************************************************

// Headers for this module
#include "FADCPulseParametersUCLA.h"
using namespace FADCPulseParameters;

// Offline headers
#include <fwk/CentralConfig.h>
#include <fwk/RunController.h>
using namespace fwk;

#include <evt/Event.h>
#include <evt/ShowerRecData.h>
#include <evt/ShowerSRecData.h>

#include <sevt/SEvent.h>
#include <sevt/Header.h>
```

```
#include <sevt/Station.h>
#include <sevt/StationRecData.h>
#include <sevt/PMT.h>
#include <sevt/PMTRecData.h>

#include <det/Detector.h>

#include <utl/Reader.h>
#include <utl/AugerUnits.h>
#include <utl/ErrorLogger.h>
#include <utl/Trace.h>
#include <utl/TraceAlgorithm.h>
using namespace utl;

// ROOT headers
#include <TFormula.h>

// Standard c++ headers
#include <iostream>
#include <cmath>
#include <map>
using std::cout;
using std::endl;

// These are static variables and will be refered to in this manner throughout
double FADCPulseParametersUCLA::Risetime = -1.0;
double FADCPulseParametersUCLA::RisetimeError = -1.0;
double FADCPulseParametersUCLA::RisetimeReducedChi2 = -1.0;
RisetimeResultsUCLA* FADCPulseParametersUCLA::RisetimeResults = NULL;
// End static variables

//#define DEBUG_FADCPulseParametersUCLA

RisetimeResultsUCLA::RisetimeResultsUCLA()
{
  fFitPar0 = 0.0;
  fFitPar1 = 0.0;
  fRisetime = -1.0;
  fRisetimeError = -1.0;
  fRisetimeChi2 = -1.0;
  fRisetimeNDF = -1.0;
  fXmax = -1.0;
  fXmaxErrorUp = -1.0;
  fXmaxErrorDown = -1.0;
```

```
}

RisetimeResultsUCLA::~RisetimeResultsUCLA()
{
  for(std::vector<StationRisetimeDataUCLA*>::iterator stationrisetimeiterator =
fStationData.begin();
      stationrisetimeiterator != fStationData.end(); ++stationrisetimeiterator)
    delete *stationrisetimeiterator;
  fStationData.clear();
}

FADCPulseParametersUCLA::FADCPulseParametersUCLA()
{
  // Define the Risetime
  RiseTime_StartPercent          = 0.1;    //10%
  RiseTime_StopPercent           = 0.5;    //50%
  ForceRiseTimeRecalculation     = false;  //False

  // Fit the Risetime
  DoRiseTimeFit                  = true;   //True
  MinimumSignalForRiseTimeFit    = 10.0;   //10.0 VEM
  MinimumDistanceForRiseTimeFit  = 0.0;    //0.0 meters
  MaximumDistanceForRiseTimeFit  = 1600.0; //1600.0 meters
  IncludeSaturatedForRiseTimeFit = false;  //False
  DistanceToInterpolateFitResult = 1000.0; //1000.0 meters
  RTWeightingFunction = NULL;
  RTWeights = NULL;
  RiseTimeGraph = NULL;
  fRejectedStations = 0;
}

FADCPulseParametersUCLA::~FADCPulseParametersUCLA()
{
  if(RTWeightingFunction != NULL)
    delete[] RTWeightingFunction;
  if(RTWeights != NULL)
    delete RTWeights;
  if(RiseTimeGraph != NULL)
    delete RiseTimeGraph;
  if(FADCPulseParametersUCLA::RisetimeResults != NULL)
    delete FADCPulseParametersUCLA::RisetimeResults;
}

VModule::ResultFlag FADCPulseParametersUCLA::Init(void)
```

```
{
  CentralConfig *theConfig = CentralConfig::GetInstance();
  std::ostringstream info;
  std::string WeightingFunction;
  std::map<std::string, std::string> Attributes;

  INFO("FADCPulseParametersUCLA::Init()");

  info << "Configuring the FADC Parameters module." << endl;
  info << "**********************************" << endl;

  Branch topBranch = theConfig->GetTopBranch("FADCPulseParameters");

  //Risetime Stuff
  //Branch RiseTimeBranch = topBranch.GetChild("RecalculateRisetime");
  Branch RiseTimeBranch = topBranch.GetFirstChild();
  RiseTimeBranch.GetChild("RiseTimeStart").GetData(RiseTime_StartPercent);
  RiseTimeBranch.GetChild("RiseTimeStop").GetData(RiseTime_StopPercent);
  Attributes = RiseTimeBranch.GetAttributes();
  if(Attributes["ReCalc"] == "YES" || Attributes["ReCalc"] == "Yes" ||
Attributes["ReCalc"] == "yes")
    {
      info << "Going to recalculate risetimes for stations.\n";
      info << "Pulse RiseTime defined as:" << endl;
      info << RiseTime_StartPercent*100 << "% to " << RiseTime_StopPercent*100
     << "% of total signal." << endl;
      ForceRiseTimeRecalculation = true;
    }
  else
    {
      info << "Using existing station risetimes (from SdCalibrator)." << endl;
      ForceRiseTimeRecalculation = false;
    }
  //End Risetime Stuff

  //Risetime Fit Stuff
  info << endl << "Configuring the risetime fit routines." << endl;
  Branch RisetimeFitBranch;
  //if(RisetimeFitBranch = topBranch.GetChild("DoRisetimeFit"))
  if(RisetimeFitBranch = RiseTimeBranch.GetNextSibling())
    {
      Attributes = RisetimeFitBranch.GetAttributes();
    }
```

```
 if(Attributes["Fit"] == "YES" || Attributes["Fit"] == "Yes" || Attributes["Fit"]
== "yes")
   {
     info << "Fitting the risetime for the event is enabled.\n";

     DoRiseTimeFit = true;
     RisetimeFit-
Branch.GetChild("MinimumSignal").GetData(MinimumSignalForRiseTimeFit);
     RisetimeFit-
Branch.GetChild("MinimumDistance").GetData(MinimumDistanceForRiseTimeFit);
     RisetimeFit-
Branch.GetChild("MaximumDistance").GetData(MaximumDistanceForRiseTimeFit);
     RisetimeFit-
Branch.GetChild("RisetimeEvaluatedAt").GetData(DistanceToInterpolateFitResult);
     info << "\tMinimum Signal " << MinimumSignalForRiseTimeFit << "
VEM\n"
    << "\tMinimum Distance " << MinimumDistanceForRiseTimeFit/m << "
meters\n"
    << "\tMaximum Distance " << MaximumDistanceForRiseTimeFit/m << "
meters\n"
    << "\tRisetime Distance " << DistanceToInterpolateFitResult/m << "
meters\n";

     unsigned int includeSaturation = 0;
     RisetimeFitBranch.GetChild("IncludeSaturated").GetData(includeSaturation);
     if(includeSaturation)
 {
  IncludeSaturatedForRiseTimeFit = true;
  info << "\tIncluding saturated stations.\n";
 }
     else
 {
  IncludeSaturatedForRiseTimeFit = false;
  info << "\tNot including saturated stations.\n";
 }

     RisetimeFit-
Branch.GetChild("WeightAsFunctionDistance").GetData(WeightingFunction);
     RTWeightingFunction = new char[WeightingFunction.size() + 1];
     std::strcpy(RTWeightingFunction, WeightingFunction.c_str());
     info << "\tWeighting Function: " << RTWeightingFunction << endl;
   }
 else
   {
```

```
      info << "Fitting the risetime for the event is disabled.\n";
    }

  RTWeights = new TFormula("RiseTimeWeights", RTWeightingFunction);
  if(RTWeights->IsZombie())
    {
      std::ostringstream error;
      ERROR("Weight formula defined in FADCPulseParametersUCLA.xml contains
an error!");
      error << "Current formula is: weight=" << RTWeightingFunction << endl
      << "This formula does not conform to the ROOT formula class guidelines." <<
endl;
      ERROR(error);
      RTWeights->Delete();
      RTWeights = NULL;
      return eFailure;
    }
  //End Risetime Fit Stuff

  info << endl << "************************************" << endl;
  info << "FADC Parameters module initialized." << endl;
  INFO(info);

  return eSuccess;
}

VModule::ResultFlag FADCPulseParametersUCLA::Run(evt::Event &theEvent)
{
  std::ostringstream info;
  INFO("FADCPulseParametersUCLA::Run()");

  FADCPulseParametersUCLA::Risetime = -1.0;
  FADCPulseParametersUCLA::RisetimeError = -1.0;
  FADCPulseParametersUCLA::RisetimeReducedChi2 = -1.0;
  if(RisetimeResults != NULL)
    delete RisetimeResults;
  FADCPulseParametersUCLA::RisetimeResults = NULL;
  fRejectedStations = 0;

  if(!(theEvent.HasSEvent()))
    {
      info << "There is no SEvent" << endl;
      INFO(info);
      return eSuccess;
```

```
    }

  if(theEvent.HasRecShower())
    {
      if(theEvent.GetRecShower().HasSRecShower())
  {
    sevt::SEvent& theSEvent = theEvent.GetSEvent();
    FADCPulseParametersUCLA::RisetimeResults = new RisetimeResultsUCLA;
    cout << "FADC Parameters - Event " << theSEvent.GetHeader().GetId() <<
endl;

    for(sevt::SEvent::StationIterator sIt = theSEvent.StationsBegin();
sIt!=theSEvent.StationsEnd(); ++sIt)
      {
        sevt::Station& currentStation = *sIt;
        if(theSEvent.HasStation(currentStation.GetId()) &&
currentStation.HasVEMTrace() && currentStation.HasRecData())
    {
      double stationrisetime;
      double stationrisetimeerror;
      double stationdistance;
      double stationdistanceerror;
      unsigned short rejectcode = 0x00;

      // Setting the above variables
      sevt::StationRecData& theStationRecData = currentStation.GetRecData();
      stationrisetime = theStationRecData.GetRiseTime();

      if(ForceRiseTimeRecalculation)
        stationrisetime = RecalculateRiseTime(currentStation);

      if(stationrisetime <= 0.0)
        {
          cout << "Station " <<currentStation.GetId() <<
      " has no rise time information, calculating..." << endl;
          stationrisetime = RecalculateRiseTime(currentStation);
          if(stationrisetime <= 0.0)
      continue;
        }

      // Prefer the first method, but currently not implimented in v2r2 of the offline
      //const double secZenith = 1.0/std::cos(theEvent.GetRecShower().GetZenith());
// is this in radians?
```

```
    // Eliminate once RecShower-> GetAzimuth() and GetZenith() and GetCore()
work
    // This line is using the current agreed method for Sd reconstuction where
    // GetX(SiteCoordinateSystem) returns the shower u and
GetY(SiteCoordinateSystem)
    // returns the shower v.
    const CoordinateSystemPtr CS =
det::Detector::GetInstance().GetSiteCoordinateSystem();
    const double this_u =
theEvent.GetRecShower().GetSRecShower().GetAxis().GetX(CS);
    const double this_v =
theEvent.GetRecShower().GetSRecShower().GetAxis().GetY(CS);
    const double EventThetaRec = std::asin(sqrt(this_u*this_u + this_v*this_v)); //
in radians
    const double secZenith = 1.0/std::cos(EventThetaRec);
    // End hack for zenith angle

    stationdistance = theStationRecData.GetSPDistance();
    stationdistanceerror = theStationRecData.GetSPDistanceError();
    // Added a correction to the MeanRiseTime for shower asymmetry as
    // suggested by the Leeds group in a private communication.
    // t1/2(correct) = t1/2 - g cos(zeta)
    // g = alpha + gamma r^2
    // alpha = -66.61 + 95.13 sec(theta) - 30.73 sec^2(theta)
    // gamma = -0.0009721 + 0.001993 sec(theta) - 0.001259 sec^2(theta) +
0.0002546 sec^3(theta)
    //
    // r is the distance to the shower plane (meters), theta is the zenith angle,
    // and zeta is the angle to a station with the zero direction defined
    // to be under the shower axis.
    // M.Healy August 8, 2006
    const double alpha = -66.61+95.13*secZenith-30.73*secZenith*secZenith;
    const double gamma = -0.0009721+0.001993*secZenith
      -0.001259*secZenith*secZenith
      +0.0002546*secZenith*secZenith*secZenith;
    const double g = alpha + gamma*stationdistance*stationdistance;
    // This gets the asymmetry angle as set by the reconstruction module.
    // Beware of custom reconstructions that do not set this information.
    const double zeta = theStationRecData.GetAzimuthShowerPlane();
    stationrisetime = stationrisetime - g*std::cos(zeta);
    // M.Healy August 8, 2006
    // End additions by M.Healy
    stationrisetimeerror = RTWeights->Eval(stationdistance/m,  // slight mistake in
error propogation here
```

```
            secZenith,
            theStationRecData.GetTotalSignal());

      if(theStationRecData.GetTotalSignal() < MinimumSignalForRiseTimeFit)
        rejectcode = rejectcode — 0x01;
      if(!currentStation.IsCandidate())
        rejectcode = rejectcode — 0x02;
      if(currentStation.IsLowGainSaturation() & !IncludeSaturatedForRiseTimeFit)
        rejectcode = rejectcode — 0x04;
      if(stationdistance < MinimumDistanceForRiseTimeFit || stationdistance >
MaximumDistanceForRiseTimeFit)
        rejectcode = rejectcode — 0x08;
      // Done setting variables

      if(rejectcode != 0)
        fRejectedStations++;

      // Assign to the station risetime data
      StationRisetimeDataUCLA* currentStationRisetimeData = new
StationRisetimeDataUCLA;
      currentStationRisetimeData->fStationId     = currentStation.GetId();
      currentStationRisetimeData->fRisetime      = stationrisetime;
      currentStationRisetimeData->fRisetimeError = stationrisetimeerror;
      currentStationRisetimeData->fDistance      = stationdistance;
      currentStationRisetimeData->fDistanceError = stationdistanceerror;
      currentStationRisetimeData->fRejectCode    = rejectcode;
      // End assign data

#ifdef DEBUG_FADCPulseParametersUCLA

      cout << "Station Id: " << currentStationRisetimeData->fStationId << '\n'
           << "Risetime: " << currentStationRisetimeData->fRisetime << '\n'
           << "Risetime Error: " << currentStationRisetimeData->fRisetimeError <<
'\n'
           << "Distance: " << currentStationRisetimeData->fDistance << '\n'
           << "DistanceError: " << currentStationRisetimeData->fDistanceError <<
'\n'
           << "RejectCode: " << currentStationRisetimeData->fRejectCode << '\n';

#endif

      FADCPulseParametersUCLA::RisetimeResults-
>fStationData.push_back(currentStationRisetimeData);
    }
```

```
    }
  }
    else
  {
   info << "There is no surface reconstruction!"
        << "Need a core position and zenith angle before this module." << endl;
   INFO(info);
   return eSuccess;
  }
   }

  if(DoRiseTimeFit)
   {
    FitEventRiseTime();

    cout << "The RiseTime at " << DistanceToInterpolateFitResult/km
    << "km is " << FADCPulseParametersUCLA::Risetime
    << " +- " << FADCPulseParametersUCLA::RisetimeError
    << " ns" << endl;
   }

  return eSuccess;
}

VModule::ResultFlag FADCPulseParametersUCLA::Finish(void)
{
  INFO("FADCPulseParametersUCLA::Finish()");

  return eSuccess;
}

double FADCPulseParametersUCLA::FitEventRiseTime()
{
  const unsigned int POINTS_IN_GRAPH =
    FADCPulseParametersUCLA::RisetimeResults->fStationData.size() -
fRejectedStations;

  // If only 2 stations pass the cuts then we will ignore the event
  // M.Healy (18 Sep 2006)
  if(POINTS_IN_GRAPH <= 2)
   {
    INFO("Event risetime uncalculated due to an insuffiecent number of acceptable
stations.");
    return -1.0;
```

```
    }

  double *distances = new double[POINTS_IN_GRAPH];
  double *distanceserror = new double[POINTS_IN_GRAPH];
  double *risetimes = new double[POINTS_IN_GRAPH];
  double *risetimeserror = new double[POINTS_IN_GRAPH];
  StationRisetimeDataUCLA* currentStation;
  unsigned int point = 0;

  for(std::vector<StationRisetimeDataUCLA*>::const_iterator stationrisetimeiterator
=
  FADCPulseParametersUCLA::RisetimeResults->fStationData.begin();
      stationrisetimeiterator !=
FADCPulseParametersUCLA::RisetimeResults->fStationData.end();
      ++stationrisetimeiterator)
    {
      currentStation = *stationrisetimeiterator;
      if(currentStation->fRejectCode != 0)
  continue;

      distances[point] = currentStation->fDistance/km;
      distanceserror[point] = currentStation->fDistanceError/km;
      risetimes[point] = currentStation->fRisetime/ns;
      risetimeserror[point] = currentStation->fRisetimeError/ns;

      cout << "--- ** Passed Cut ** ---"
     << "\nstation: "  << currentStation->fStationId
     << "\ndistance: " << distances[point]
     << "\nrisetime: " << risetimes[point]
     << endl;

      point++;
    }

  cout << endl << "—- " << POINTS_IN_GRAPH << " stations passed the cuts."
<< endl;

  RiseTimeGraph = new TGraphErrors(POINTS_IN_GRAPH, distances, risetimes, 0,
risetimeserror);
  RiseTimeGraph->SetMarkerStyle(20);
  RiseTimeGraph->SetMarkerColor(2);
  RiseTimeGraph->SetLineColor(2);
  RiseTimeGraph->SetLineWidth(2);
  TF1 risetimeFit("RisetimeFit", "40+[0]*x+[1]*x*x",
```

```
    MinimumDistanceForRiseTimeFit/km, MaximumDistanceForRiseTimeFit/km);
  risetimeFit.SetParLimits(0, 0.0, 10000.0);
  risetimeFit.SetParLimits(1, 0.0, 10000.0);
  RiseTimeGraph->Fit(&risetimeFit, "Q", "", MinimumDistanceForRiseTimeFit/km,
MaximumDistanceForRiseTimeFit/km);

  const double risetime     = risetimeFit.Eval(DistanceToInterpolateFitResult/km);
  const double risetimeerr  = std::sqrt(std::pow(risetimeFit.GetParError(0), 2)
          +std::pow(risetimeFit.GetParError(1), 2));
  const double risetimechi2 = risetimeFit.GetChisquare();
  const double risetimeNDF  = risetimeFit.GetNDF();

  FADCPulseParametersUCLA::Risetime = risetime*ns;
  FADCPulseParametersUCLA::RisetimeError = risetimeerr*ns;
  FADCPulseParametersUCLA::RisetimeReducedChi2 = risetimechi2/risetimeNDF;

  FADCPulseParametersUCLA::RisetimeResults->fFitPar0 =
risetimeFit.GetParameter(0)*m/km;
  FADCPulseParametersUCLA::RisetimeResults->fFitPar1 =
risetimeFit.GetParameter(1)*m/km*m/km;
  FADCPulseParametersUCLA::RisetimeResults->fRisetime = risetime*ns;
  FADCPulseParametersUCLA::RisetimeResults->fRisetimeError = risetimeerr*ns;
  FADCPulseParametersUCLA::RisetimeResults->fRisetimeChi2 = risetimechi2;
  FADCPulseParametersUCLA::RisetimeResults->fRisetimeNDF = risetimeNDF;

  // This functionality not yet included
  FADCPulseParametersUCLA::RisetimeResults->fXmax = -1.0;
  FADCPulseParametersUCLA::RisetimeResults->fXmaxErrorUp = -1.0;
  FADCPulseParametersUCLA::RisetimeResults->fXmaxErrorDown = -1.0;

  RiseTimeGraph->Delete();
  RiseTimeGraph = NULL;

  delete[] distances;
  delete[] distanceserror;
  delete[] risetimes;
  delete[] risetimeserror;

  return risetime*ns;
}

double FADCPulseParametersUCLA::RecalculateRiseTime(sevt::Station
&theStation)
{
```

```
  int start_bin, stop_bin, num_pmts = 0;
  double risetime_start, risetime_stop, total_risetime = 0;
  double MeanRiseTime, RMSRiseTime;
  std::vector<double> risetime;
  for(sevt::Station::PMTIterator pmtIt = theStation.PMTsBegin(); pmtIt !=
theStation.PMTsEnd(); ++pmtIt)
    {
      sevt::PMT &currentPMT = *pmtIt;
      if(currentPMT.HasRecData() && currentPMT.GetRecData().HasVEMTrace()){
  num_pmts++;
  sevt::PMTRecData &pmtRec = currentPMT.GetRecData();
  TraceD &aVEMTrace = pmtRec.GetVEMTrace();

  start_bin = theStation.GetRecData().GetSignalStartSlot() - 4;
  stop_bin = theStation.GetRecData().GetSignalEndSlot();

  if(start_bin >= stop_bin || start_bin < 0 || start_bin > 5000)
    start_bin = 0;

  risetime_start =
TraceAlgorithm::TimeAtRelativeSignalX(aVEMTrace,start_bin,stop_bin,100*RiseTime_StartPercent);
  risetime_stop =
TraceAlgorithm::TimeAtRelativeSignalX(aVEMTrace,start_bin,stop_bin,100*RiseTime_StopPercent);

  risetime.push_back(risetime_stop - risetime_start);
  total_risetime += (risetime_stop - risetime_start);
      }//end if pmt has rec data
    }// end loop over PMTs

  if(num_pmts == 0)
    {
      ERROR("Valid station, but no PMTRecData.  Risetime recalculation failed!");
      return -1.0;
    }
  MeanRiseTime = total_risetime / (double)num_pmts; RMSRiseTime = 0;
  for(int i=0; i<num_pmts; i++)
    {
      RMSRiseTime += pow((MeanRiseTime - risetime[i]),2);
    }
  RMSRiseTime = sqrt(RMSRiseTime / (double)num_pmts);

  return MeanRiseTime*ns;
}
```

APPENDIX B

Photon Limit Analysis

Shower observables sensitive to composition can also be used to distinguish nuclear primaries from other non-hadronic primaries. Indeed a good deal of effort has been spent on identifying primary cosmic ray photons because many theories of exotic physics would results in a significant flux of ultra-high energy photons. In this section I details the methods to set a photon limit as done in [4, 63].

The method uses a parameterization of the risetime and the radius of curvature similar to this thesis except there is not a conversion to X-X_{max}. This conversion was not required because the limit is based **solely** on simulations of photon showers which are believed to be reliable and in that case the two observables (risetime and radius of curvature) can be compared directly between real showers and simulations.

The complete analysis package can be found at `/home/autojob/PhotonAnalysis.tar.gz` on the UCLA Pierre Auger Cluster. That file contains a fully working analysis and only requires a simulated photon spectrum, and a set of real data to derive a limit. The correct executable is `NewPhotonLimit` followed by a root file containing a photon spectrum in the UCLANtuple format. This is the same format referred to in the data analysis chapter of this thesis and is created by a module called `FillNtuple` whose source can be found at `/home/autojob/DPA/UCLA_ReconDump/`.

The limit uses parameterizations of the expected risetime and radius of curvature for photon showers. The expected value is a function of the zenith angle of the shower and S(1000). The details can be found in [4] but suffice it to say they are quadratic functions. First the expected value is parameterized as a function of the log S(1000) for several zenith angles (it doesn't matter which but the more the better of course), and then each of the three free parameters from the quadratic fit are then parameterized as a function of the cos(zenith) angles used. The parameterizations are already made and can be found in the `parameter_files/` sub-directory from the tar file. They can be remade using the `Parameterize` executable. Fig. B.1 is an example of the parameterization process. The RMS also must be parameterized as a function of log S(1000) and then the cos(zenith) angle. A simple $\frac{1}{x}$ dependence on S(1000) is assumed leading to a complete parameterization of the mean and RMS for any zenith and S(1000) as shown in fig. B.2.

Using the parameterization each event can be characterized as photon like or not depending on how many standard deviations the event is from the predicted behavior. The choice as to how close an an event needs to be before it is a photon it totally arbitrary, but will effect the efficiency to identify photons (ie if for instance we only select events that lie within the gray band we lose all those beyond one sigma, 100% - 68% = 32%). That factor would then enter the calculation of the limit.

Any events that are identified as photons must use an energy converter designed for photons because of the well known energy mismatch. The rest become hadrons and a limit is now easy to set. The fraction is simply the ratio of photons to non-photons above a given energy, the flux is just the number of photons above a given energy and the aperture.

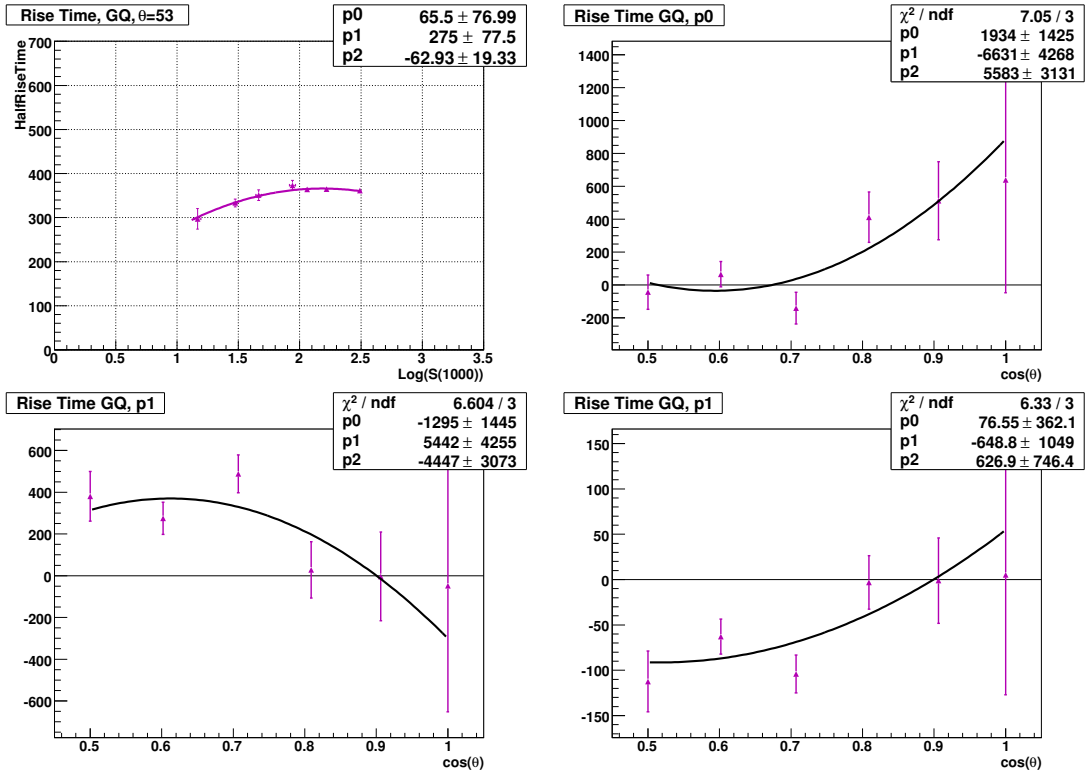

Figure B.1: Parameterizing the risetime as a function of S(1000) and then as a function of zenith angle.

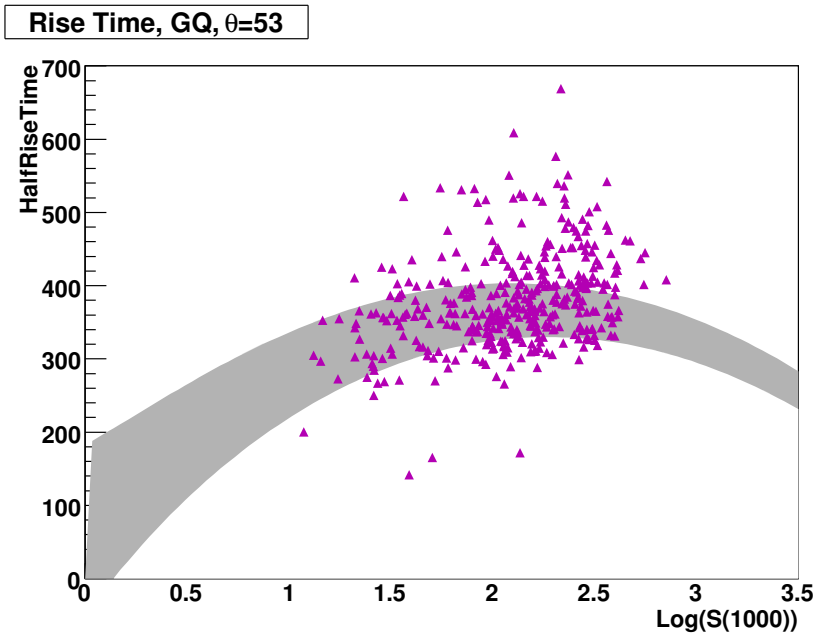

Figure B.2: The middle of the band is the expected value of the risetime for photon+qgsjet simulations while the gray area is the one sigma error region. Real showers of the same zenith and S(1000) are compared to where they lie on this figure to calculated how many standard deviations they are from the mean expected for a photon.

Do not forget to convolve the trigger efficiency[1] for photons, which varies as a function of energy, as well as the aforementioned identification efficiency. The trigger efficiency depends on how the real photon showers are distributed in energy and is estimated from a simulated photon spectrum the power-law of which is unknown. Several spectra will demonstrate the variation in trigger efficiencies.

Fig. B.3 is a plot of the monte-carlo photon shower and 5% of the real data in terms of the deviation from the photon expected value for the risetime and the radius of curvature. Clearly the data are not very similar to the photon predictions. Setting the photon identification cut at the dashed line leads to 50% efficiency and the corresponding 95% confidence limits applied to the remaining 95% of real data are shown in fig. B.4.

[1]the trigger efficiency is both the detector trigger and the ability to reconstruct the observables: risetime and radius of curvature

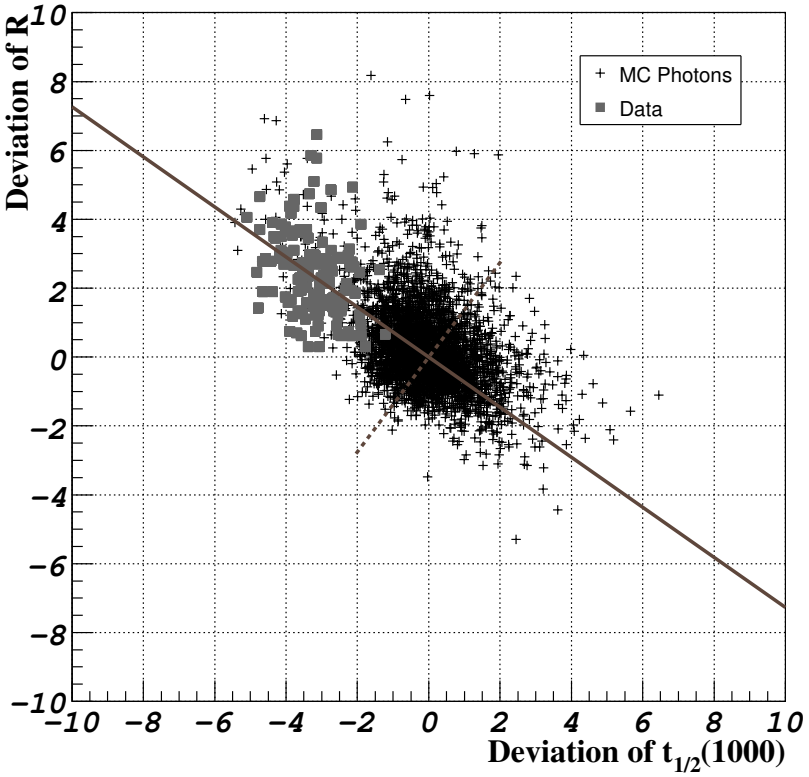

Figure B.3: The deviation of photon showers and real data from the expected value for photons showers. Of course photons are distributed around their own expected value! The dashed line is a good choice for selection photon candidates. Real data events below that line are identified as possible photon showers.

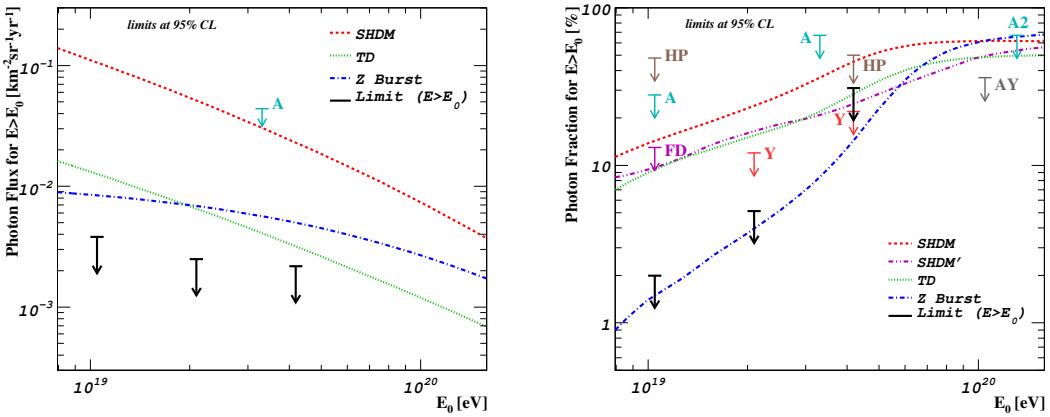

Figure B.4: **Left:** The 95% confidence limit on the flux of photons above several energies from the Pierre Auger data. Also shown are predictions from some top-down models. **Right:** The 95% confidence limit on the fraction of photons above several energies from the Pierre Auger data. Also shown are some prediction from top-down models (unfortunately the models are not identical to those in the left plot).

APPENDIX C

Other Elongation Rate Studies

A second study based on the station by station deviation of the risetime from the expected value given the energy and zenith angle of the shower was conducted on the Pierre Auger Observatory data by Ben Smith of Leeds University, England. As an analysis in preparation on the same topic as this thesis it is worth mentioning some of the preliminary results he obtained. Using the measurement uncertainty $\sigma_{t_{1/2}}$ as function of signal S in the tank, the core distance r and zenith angle θ has been determined from a small number of twin tanks and from pairs of detectors at similar core distances (within 100 m). A parameterisation of $\sigma_{t_{1/2}}$ is used to define the error bars shown in fig. C.1 (top). Measurements of $t_{1/2}$ for signals < 20 VEM are severely influenced by Poisson fluctuations due to low numbers of particles and are not used. A correction of the risetime for the azimuthal asymmetry in the shower, particularly important between 35 and 50°, is applied. For each station the deviation Δ of the measured risetime, in units of the accuracy of measurement, from the average values found for r and θ at a fixed reference energy $E \approx 10^{19}$ eV is formed, thus: $\Delta = \frac{t_{1/2}(r,\theta) - \langle t_{1/2}(r,\theta,E_{\rm ref})\rangle}{\sigma_{t_{1/2}}(S,r,\theta)}$. All stations in one event are then combined in an average event deviation $\langle\Delta\rangle$ as seen in fig. C.1 (left), which should be larger for showers developing deeper than the reference and smaller for those developing higher.

Using hybrid events [67] it can be tested whether the so-constructed variable $\langle\Delta\rangle$ indeed correlates with $X_{\rm max}$. The data have been binned in $\rm X_{max}$ (according

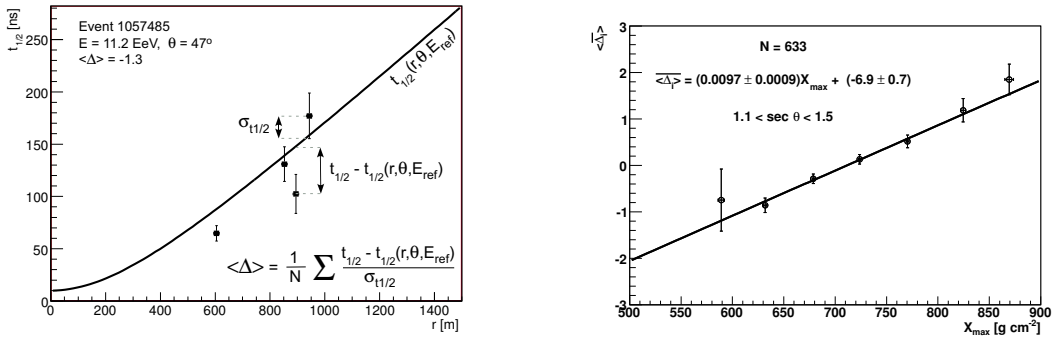

Figure C.1: **Left:** $\langle\Delta\rangle$ derived from a single event. The black line is the predicted risetime while the data points represent measurements with the error bars from twin station studies. Combining each stations' Δ from the expectation an average for the event can be defined. **Right:** $\overline{\langle\Delta\rangle}$ as a function of $X_{\rm max}$, for nearly-vertical hybrid events.

to its uncertainty of 40 g cm^{-2}, and for all events in one $X_{\rm max}$ bin the average of $\langle\Delta\rangle$ (i.e. $\overline{\langle\Delta\rangle}$) has been formed. This is shown in fig. C.1 (right). A linear dependence is observed which allows estimation of $X_{\rm max}$ from events observed with the SD alone.

Finally $\langle\Delta\rangle$ is converted into an $X_{\rm max}(\langle\Delta\rangle)$ estimate for each event, which is shown as function of energy in the right panel of Fig. C.2, where the $X_{\rm max}$ deduced are compared with direct $X_{\rm max}$ measurements and with model predictions.

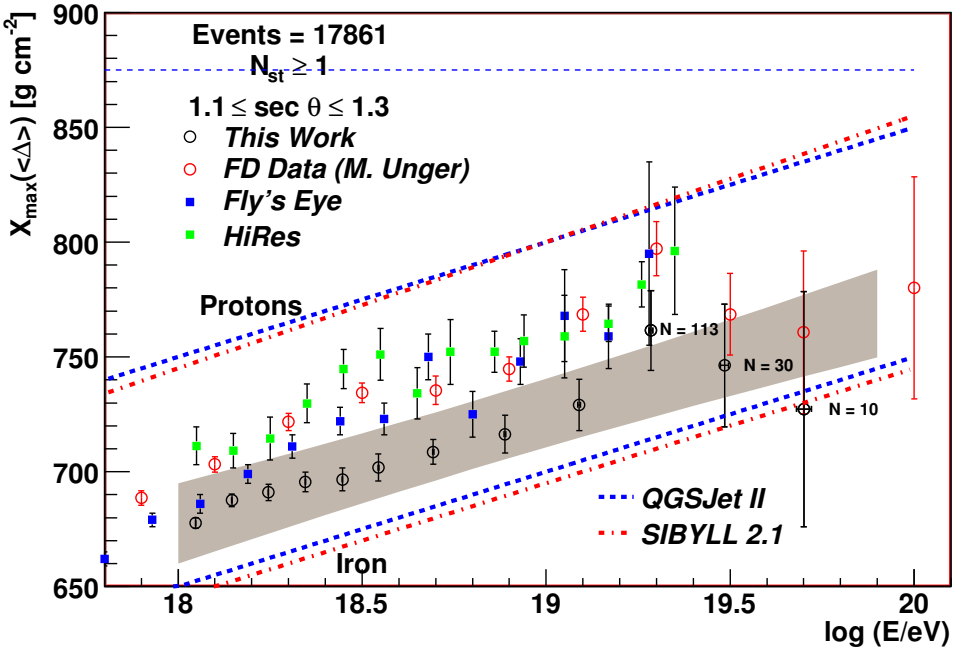

Figure C.2: X_{max} found from the $\langle\Delta\rangle$ on an event by event. The data has been binned in energy to produce an elongation rate and the corresponding uncertanty (the shaded region). This data is compared to other measurements.

References

[1] G. Archbold and P. Sokolsky [HiRes Collaboration], Chemical Composition Studies with HiRes Stereo Data, in *Proc. 28th ICRC (Tsukuba)*, 2003.

[2] R. Clay and B. Dawson, *Cosmic Bullets*, Perseus Books, 1995.

[3] G. Farmelo, The Discovery of X-Rays, Scientific American **November**, 86–91 (1995).

[4] D. Barnhill, *Composition Analysis of Ultrahigh Energy Cosmic Rays Using the Pierre Auger Observatory Surface Detector*, PhD thesis, University of California, Los Angeles, 2005, Internal Gap Note 2005-082.

[5] Energy, 1996, http://library.thinkquest.org/3659/energy/energy.html.

[6] M. A. Pomerantz, The properties of cosmic radiation at very high altitudes, Phys. Rev. (Series II) **75**, 69 (1949).

[7] V. F. Hess, The significance of variations in cosmic-ray intensity and their relation to solar, earthmagnetic and atmospheric phenomena, Rev. Mod. Phys. **11**, 153 (1939).

[8] S. H. Neddermeyer and C. D. Anderson, Note on the Nature of Cosmic-Ray Particles, Phys. Rev. (Series II) **51**, 884 (1937).

[9] P. Sokolsky, *Introduction to Ultra High Energy Cosmic Rays*, Addison-Wesley Publishing Company, Inc., 1989.

[10] K. Kamata and J. Nishimura, Prog. Theoretical Phys. **6**, 93–100 (1958).

[11] K. Greisen, op. cit. , 73.

[12] M. Takeda *et. al.* [AGASA Collaboration], Extension of the cosmic-ray energy spectrum beyond the predicted Greisen-Zatsepin-Kuzmin cutoff, Phys. Rev. Lett. **81**(1163) (1998), An update titled "Updated AGASA event list above 4×10^{19} eV," arXiv:astro-ph/0008102, is available; also see http ://www-akeno.icrr.u-tokyo.ac.jp/AGASA/.

[13] R. U. Abbasi *et. al.* [HiRes Collaboration], Measurement of the flux of ultra-high energy cosmic rays from monocular observations by the High Resolution Fly's Eye experiment, Phys. Rev. Lett. **92**(151101) (2004), arXiv:astro-ph/0208243; also see http://hires.physics.utah.edu/.

[14] Jörg R. Hörandel, Cosmic-ray composition and its relation to shock acceleration by supernova remnants, in *Proc. 36th COSPAR Scientific Assembly (Bejing)*, Jul 2006, Available as arXiv:astro-ph/0702370v1.

[15] R. Meyhandad, B. Dawson, R. Clay, L. Horton, J. Ulrichs, and M. Winn, Comparisons of some Apparent EHE Point Sources, in *Proc. 22nd ICRC (Dublin)*, volume 1, page 384, 1991.

[16] M. Takeda *et al.*, Small-scale anisotropy of cosmic rays above 10**19-eV observed with the Akeno Giant Air Shower Array, Astrophys. Journal **522**, 225 (1999), Available as arXiv:astro-ph/9902239.

[17] C. Bonifazi and A. Letessier-Selvon [Pierre Auger Collaboration], Anisotropy studies around the galactic center, (2006), Available as arXiv:astro-ph/0610160.

[18] M.S. Longair, *High-Energy Astrophysics*, Cambridge University Press, 1981.

[19] K. Greisen, End To The Cosmic Ray Spectrum?, Phys. Rev. Lett. **16**, 748 (1966).

[20] G. T. Zatsepin and V. A. Kuzmin, Upper Limit Of The Spectrum Of Cosmic Rays, Pisma Zh. Eksp. Teor. Fiz. **4**, 114 (1966).

[21] E. Parizot *et al.* for the Pierre Auger Collaboration, Aperture calculation of the Pierre Auger Observatory surface detector, in *Proc. 29th ICRC (Pune)*, volume 1, 2005.

[22] P. A. Collaboration, *Pierre Auger Observatory: Technical Design Report*, The Pierre Auger Collaboration, March 2004.

[23] S. Dagoret-Campagne, The Central Trigger, User Guide and Reference Manual, Internal Gap Note 2004-020, 2004.

[24] D. F. Barbosa, I. M. Pepe, G. P. Guedes, L. C. S. oes soares, A. L. Aguera, I. Rodriguez, M. de Fátima, and C. Rosolem, Batteries Performance Characterization - I, Internal Gap Note 2007-022, 2007.

[25] A. Lopez-Aguera, E. Lorenzo, E. Marques, G. Parente, I. Rodriguez-Cabo, and E. Zas, Solar Panels for Auger Southern Observatory: A quality check, Internal Gap Note 2005-106, 2005.

[26] C. L. Pryke, Long Baseline Testing of a GPS Based, Autonomous Event Time-tagging System, Internal Gap Note 1997-017, 1997.

[27] R. Brun and F. Rademakers, ROOT - An Object Oriented Data Analysis Framework, in *Proceedings AIHENP'96 Workshop, (Lausanne)*, September 1996, Additinal information in *Nucl. Inst. and Meth. in Phys. Res. A* **389** (1997) 81-86; see also http://root.cern.ch/.

[28] J. Abraham *et. al.* [Pierre Auger Colaboration], Properties and Performance of the Prototype Instrument for the Pierre Auger Observatory, Nuclear Instruments and Methods in Physics Reseach (NIM) **A523**(Issues 1-2), 50 (2004).

[29] A. Tripathi *et. al.*, A Systematic Calibration of Surface Detectors using Muon Data from the Engineering Array, Internal Gap Note 2002-046, 2002.

[30] X. Bertou, P.S. Allison, C. Bonifazi, P. Bauleo, C.M. Grunfeld, M. Aglietta, F. Arneodo, D. Barnhill, J.J. Beatty, N.G. Busca, A. Creusot, D. Dornic, A. Etchegoyen, A. Filevich, P.L. Ghia, I. Lhenry-Yvon, M.C. Medina, E. Moreno, D. Nitz, T. Ohnuki, S. Ranchon, H. Salazar, T. Suomijarvi, D. Supanitsky, A. Tripathi, M. Urban, L. Villasenor, for the Pierre Auger Collaboration, Calibration of the Surface Detector of the Pierre Auger Observatory, Nuclear Instruments and Methods in Physics Research **A568**, 839 (2006).

[31] J. Lee *et. al.*, Long Term Performance and Stability of the Surface Detector from September 2003 through June 2004, Internal Gap Note 2004-044, 2004.

[32] K. Shinozaki *et. al.* [AGASA Collaboration], Chemical Composition of Ultra-high Energy Cosmic Rays observed by AGASA, in *Proc. 28th ICRC (Tsukuba)*, 2003.

[33] P. A. Collaboration, An Upper Limit to the Photon Fraction in Cosmic Rays Above 10^{19}eV from the Pierre Auger Observatory, Astroparticle Physics **27**, 155 (2007).

[34] O. Blanch-Bigas *et. al.* for the Pierre Auger Collaboration, Limits to the diffuse flux of UHE tau neutrinos at EeV energies from the Pierre Auger Observatory, in *Proc. 30th ICRC (Mérida)*, 2007.

[35] D. Gora, M. Roth, and A. Tamburro, A MC approach to simulate up- and down-going neutrino showers including local topographic conditions, Internal Gap Note 2006-077, 2006.

[36] P. Sommers *et. al.* for the Pierre Auger Collaboration, First estimate of the primary cosmic ray energy spectrum above 3 EeV from the Pierre Auger Observatory, (2005), available as arXiv:astro-ph/0507150.

[37] A. Tripathi, K. Arisaka, J. Lee, D. Barnhill, T. Ohnuki, M. Healy, and W. Slater, A preliminary estimate of the cosmic ray energy spectrum from the Pierre Auger Observatory Data, Internal Gap Note 2005-061, August 2005.

[38] Darko Veberič and Markus Roth for the Offline team, The Offline Reconstruction Manual, Internal Gap Note 2005-035.

[39] P. Billoir, FADC trace cleaning in Surface Detector through a segmentation procedure, Internal Gap Note 2005-074, 2005.

[40] B. D. Hieu and A. Watson, Analysis of the risetime and its uncertainty for events recorded by the surface detector in the Pierre Auger Observatory, Internal Gap Note April 2005.

[41] C. Wileman, Parameterization of Risetime Asymetries from Twin Tank Studies, Private Communication, 2006.

[42] N. Kalmykov, S. Ostapchenko, and A. Pavlov, Nuclear Physics B (Proc. Suppl.) .

[43] R. Fletcher, T. Gaisser, P. Lipari, and T. Stanev, **D50**(5710) (1994), See also J. Engel, T.K. Gaisser, P. Lipari, and T. Stanev *Phys. Rev.* **D46** (1992) 5013.

[44] S.J. Sciutto, Departamento de Fisica Universidad Nacional de la Plata, AIRES–A package for the simulation of extensive air showers, Available from http://www.fisica.unlp.edu.ar/auger/aires/.

[45] D. Barnhill, K. Arisaka, M. Healy, J. Lee, and P. Boghrat, A Study of Composition Trends Using Rise Time Data, Internal Gap Note 2006-017, 2006.

[46] B. Dawson *et al.* for the Pierre Auger Collaboration, Hybrid Performance of the Pierre Auger Observatory, in *Proc. 30th ICRC (Mérida)*, 2007.

[47] M. Unger *et al.* for the Pierre Auger Collaboration, Study of the Cosmic Ray Composition above 0.4 EeV using the Longitudinal Profiles of Showers observed at the Pierre Auger Observatory, in *Proc. 30th ICRC (Mérida)*, 2007.

[48] T.K. Gaisser and A.M. Hillas, Reliability of the Method of Constant Intensity Cuts for Reconstruction of the Average Development of Vertical Showers, in *Proc. 15th ICRC (Plovdiv)*, volume **8**, page 353, 1977.

[49] B. Revenu *et. al.* for the Pierre Auger Collaboration, Search for localized excess fluxes in Auger sky maps and prescription results, in *Proc. 29th ICRC (Pune)*, 2007.

[50] C. Hojvat, The Acceptance for the Auger Observatory Surface Detector, Internal Gap Note 1997-003, 1997.

[51] M. Roth *et. al.* for the Pierre Auger Collaboration, Measurement of the UHECR spectrum using data from the Surface Detector of the Pierre Auger Observatory, in *Proc. 30th ICRC (Mérida)*, 2007.

[52] R. Engel *et al.* for the Pierre Auger Collaboration, Test of hadronic interaction models with data from the Pierre Auger Observatory, in *Proc. 30th ICRC (Mérida)*, 2007.

[53] C. Bonifazi *et al.* for the Pierre Auger Collaboration, Angular Resolution of the Pierre Auger Observatory, in *Proc. 29th ICRC (Pune)*, volume 1, 2005.

[54] D. Newton, J. Knapp, and A. A. Watson, The Optimum Distance at which to Determine the Size of a Giant Air Shower, Astroparticle Physics **26**, 414 (2007).

[55] S. Ostapchenko, Nucl. Phys. B (Proc. Suppl.) **151**, 143 and 147 (2006), See also *Phys. Rev.* D **74** (2006) 014026.

[56] R. Engel, T. Gaisser, P. Lipari, and T. Stanev, in *Proc. 26th Int. Cosmic Ray Conf., (Salt Lake City)*, volume 1, page 415, 1999.

[57] K. Werner, F. M. Liu, and T. Pierog, Phys. Rev. C **74**(044902) (2006).

[58] D. Heck and J. Knapp and J.N. Capdevielle and G. Schatz and T. Thouw, *Corsika: A Monte Carlo Code to Simulate Extensive Air Showers*, Report **FZKA 6019**, Forschungszentrum Karlsruhe, 1998, Available from http://www-ik.fzk.de/corsika/physics_description/corsika_phys.html.

[59] D. Heck and J. Knapp, (1998), Available from http://www-ik.fzk.de/~heck/publications/.

[60] A. Fassò, A. Ferrari, S. Roesler, P. Sala, G. Battistoni, F. Cerutti, E. Gadioli, M. Garzelli, F. Ballarini, O. Ottolenghi, A. Empl, and J. Ranft, The physics models of FLUKA: status and recent developments, in *Computing in High Energy and Nuclear Physics Conference (CHEP2003), (La Jolla)*, March 2003, Available as arXiv:hep-ph/0306267; see also http://www.fluka.org/references.html.

[61] S. Argiró, S. Barroso, J. Gonzalez, L. Nellen, T. Paul, T. Porter, L. P. Jr., M. Roth, R. Ulrich, and D. Veberič, The Offline Software Framework of the Pierre Auger Observatory, Nuclear Instruments and Methods in Physics Research (NIM A) (2007), Article Currently Under Review.

[62] S. Agostinelli *et al.*, G4–a simulation toolkit, Nucl. Instrum. Meth. A **506**, 250 (2003), See also *IEEE Transactions on Nuclear Science,***53***:270 (2006)* by J. Allison *et al.* and http://geant4.cern.ch/.

[63] M. Healy *et al.* for the Pierre Auger Collaboration, Search for Ultra-High Energy Photons with the Pierre Auger Observatory, in *Proc. 30th ICRC (Mérida)*, 2007.

[64] M. Roth for the Offline team, The Pierre Auger Observer, A web site devoted to the distribution of standardized reconstruction results http://augerobserver.fzk.de/.

[65] P. Billoir, Indirect Measurement of Xmax with the Surface Detector, Internal Gap Note 2004-010, 2004.

[66] B. Collins-Sussman, B. W. Fitzpatrick, and C. M. Pilato, *Version Control with Subversion*, O'Reilly Media, 2007, Available at http://svnbook.red-bean.com/; see also http://subversion.tigris.org/.

[67] M. Mostafa *et al.* for the Pierre Auger Collaboration, Hybrid Activities of the Pierre Auger Observatory, in *Proc. Cosmic Ray International Seminar (Catania)*, 2006, Available as arXiv:astro-ph/0608670.